The Atmospheric Transport in the Western Pacific Region by Measurements and Model Simulations

Dissertation

Zur Erlangung des akademischen Grades
Doktor der Naturwissenschaften (Dr. rer. nat.)
im
Fachbereich Physik und Elektrotechnik
der
Universität Bremen vorgelegt von

Xiaoyu Sun

eingereicht am: 14. December 2023
Datum des Kolloquiums: 15. February 2024

1. Gutachter: Prof. Dr. Justus Notholt
2. Gutachter: Prof. Dr. Mihalis Vrekousis

Abstract

The major pathway for air entering the stratosphere is over the Tropical Western Pacific (TWP) region, and this key region influences the atmospheric composition in the stratosphere. Motivated by this, we used trace gases measurements by using the Fourier Transform Infrared (FTIR) Spectrometer and cirrus cloud measurements by using a ground-based COMpact Cloud Aerosol Lidar, COMCAL from the atmospheric observatory at Koror, Palau (7.34°N, 134.47°E, in the heart of the Pacific warm pool) and combined model simulations to study the transport pathways, with a special focus on the stratosphere-troposphere exchange (STE) processes over this key region.

The atmospheric transport dynamics in the TWP region are closely linked to the movements of the circulation system, particularly the Inter-Tropical Convergence Zone (ITCZ) associated with the up-welling branch of the Hadley cell. Given the limitations of traditional ITCZ indicators, such as the maximum tropical rain belt to determine the air mass origins, I have developed a tool termed the Chemical Equator (CE), modified from Hamilton et al. (2008) to study the Inter-hemispheric Transport (IHT). The CE is calculated by the model simulation of an artificial passive tracer by GEOS-Chem to discern the migration patterns of circulation systems and air mass origins. Subsequently, the CE was used to characterize tropospheric carbon monoxide (CO) and ozone (O_3) column measurements using the FTIR Spectrometer and the ozone sondes, respectively. The observed low CO and O_3 during summer and early autumn, contrasting with maxima in winter and early spring, were outlined by the seasonal meridian movement of the CE. Additionally, comparisons were made between CE and commonly used IHT indicators, such as satellite measurements of methane (CH_4) and CO, and model simulations of sulfur hexafluoride (SF_6). Particularly, the position of CE demonstrated agreement with the meridional gradient boundary of those trace gases. Consequently, the impact of IHT on the seasonal variation of the trace gases in the tropospheric TWP region suggests that CE holds the potential to differentiate diverse air mass origins influenced by large-scale atmospheric circulation.

Upper-air observations targeting the Upper Troposphere and Lower Stratosphere (UTLS) were performed to detect cirrus cloud layers using Lidar, COMCAL. The annual cycle shows that cloud layer height peaks with the highest Cold Point Tropopause (CPT) in winter and reaches its minimum with the lowest CPT in summer. In comparison with similar cirrus cloud measurements obtained in other tropical sites, our measurements reveal that cirrus clouds detected over TWP are the coldest and highest. The prevalence of the coldest cirrus cloud layer detected over Palau corresponds to the cold trap, a region of exceptionally cold air, in UTLS over the TWP region. In order to build the relationship between STE in the UTLS region and measurements, we conducted trajectory analysis by Hybrid Single-Particle Lagrangian Integrated Trajectory (HYSPLIT) model simulations based on cirrus cloud layer measurements. Our observation results reveal that only in winter with high supersaturation at the measured cirrus clouds, the air masses are further dehydrated and slowly ascend into the stratosphere.

Conclusively, we present an atmospheric transport scheme over the TWP region based on horizontal IHT and vertical STE processes and provide observational and model simulation support for it. In the lower heights, from the surface to the free troposphere, the transport and air mass origins are characterized by the meridian movement of the CE. In the UTLS region, measurements of cloud layers and trajectories validate the pathways of STE. During summer, pristine air from the Pacific Ocean reaches Palau, with oceanic short-lived species injected into the stratosphere through rare and the highest overshooting tops. Conversely, Southeast Asia dominates air mass origins over the TWP region in winter, transporting a high level of anthropogenic species, such as O_3 and CO, into the stratosphere via the pathway within the cold trap. This winter-specific cold trap pathway, seasonally persisting over Palau, plays a crucial role in altering the stratospheric atmosphere through the transport of troposphere-originate air masses.

Acknowledgements

I would like to thank Prof. Dr. Justus Notholt, who gave me the opportunity to conduct my PhD work in his working group at the University of Bremen. I am grateful for his support during my whole research and for the time he spent reviewing this thesis.

I would like to particularly thank Dr. Mathias Palm for supervising my PhD studies. I learnt the basic theories of FTIR spectrometry and trace gas retrieval with his guidance. He provided the initial idea for this project and spent plenty of work on the proposal ROMIC-II. I also appreciate his advice on reviewing my work and this thesis.

I would like to express my gratitude to Dr. Christoph Ritter. He has explained the basic theories of the ground-based polarization Lidar and particle property retrieval. He spent a lot of time helping me retrieve the data from the ComCAL lidar. He also provided me guidance on my PhD work.

I would like to express my deep gratitude to Dr. Katrin Müller for co-supervising my PhD. She helped me start with the project and provided a basic understanding of the scientific background of the Western Pacific region. She has always provided me with scientific insights and useful comments on my work.

Discussions with many other colleagues at IUP ensured the progress of my thesis and, I could not have undertaken this journey without (in no particular order): Matthias Buschmann, Thorsten Warneke, Lukas Heizmann, Alexandra Klemme, Jamal Makkor, Christof Petri, Winfried Markert and Jonas Hachmeister (special thanks for the methane satellite data and his guidance for its usage).

Without technical and logistical support, the experimental base and the measurement data for this thesis would not exist. I would like to thank all the collaborators for their precious contributions to the Palau Weather Observation Station. I want to thank Impres GmbH for taking care of the ComCAL lidar. I also want to thank the Palau Community College (PCC), with President Patrick Tellei, for providing a space in the college for our lab containers. I would like to thank the Coral Reef Research Foundation for holding our liquid nitrogen generator in their station. I am thanking Sharon Patris, the main local operator, who has launched most of the ozone sondes and she took care of the FTIR spectrometry and remains an excellent and careful contact on-site.

In the end, I would like to acknowledge my family and friends. They also played an irreplaceable role in my PhD process. They gave me the gentlest encouragement and strongest support when I felt stressed and motivational lows. They tolerated my anxiety before the deadline and my frustration when I encountered problems. Thanks to their support and encouragement, the joy of being together with them is the greatest support for me to complete this life journey. I would also like to thank my parents from the bottom of my heart, for educating, supporting, and helping me develop a thirst for knowledge and a curious personality.

Last but not least, I would like to give my deepest gratitude to my husband, my partner, and the closest person in my life, Denghui Ji, who has been with me and supported me throughout my PhD studies. I would never have been able to complete my studies without your selfless investment of time, energy, and love.

Contents

List of Figures

List of Tables

List of Abbreviations

ACCLIP	Asian Summer Monsoon Chemical & CLimate Impact Project
ARL	Air Resources Laboratory
APD	Avalanche Photo Diode
AVK	Averaging Kernel
AWI	Alfred-Wegener-Institut
BSR	Backscatter Ratio
CALIOP	Space-borne Cloud-Aerosol lidar with Orthogonal Polarization
CALIPSO	Cloud-Aerosol Lidar and Infrared Pathfinder Satellite Observations
CE	Chemical Equator
CESM2	Community Earth System Model Version 2
COD	Cloud Optical Depth
COMCAL	COMpact Cloud Aerosol Lidar
CPT	Cold Point Tropopause
CR	Color Ratio
DJF	December–January-February
DOF	Degrees of Freedom
EDGAR	Emission Database for Global Atmospheric Research
EL	Equilibrium Level
ENSO	El Niño-Southern Oscillation
ETTCi	Extremely Thin Tropical Cirrus
FTIR	Fourier Transform InfraRed
FTS	Fourier Transform spectrometer
GCC	GEOS-Chem Classic
GCHP	GEOS-Chem High Performance
GDAS	Global Data Assimilation System
GEOS	Goddard Earth Observing System
GEOS ESM	(NASA) GEOS Earth System Model
GEOS-FP	GEOS-Forward Processing
GMAO	Global Modeling and Assimilation Office
GT	Geometrical Thickness
HEMCO	Harvard–NASA EMission COmponent
HYSPLIT	Hybrid Single-Particle Lagrangian Integrated Trajectory
IHT	inter-Hemispheric Transport
ITCZ	Inter-Tropical Convergence Zone
JJA	June-July-August
LHCO	Level of Highest Convective Overshooting
LMCO	Level of Main Convective Outflow
LMS	Level of Minimum of the Stability
LNB	Level of Neutral Buoyancy
LPDR	Linear DePolarization Ratio
LR	Lidar Ratio
LRM	Lapse Rate Minimum

LRT	Lapse Rate Tropopause
LZRT	Level of Zero net Radiative Heating
MAM	March-April-May
MERRA	Modern-Era Retrospective analysis for Research and Applications
MCT	Mercury Cadmium Telluride
MIR	Mid-InfraRed
MPL	Maximum Parcel Level
NASA	National Aeronautics and Space Administration
NCEP	National Centers for Environmental Prediction
NDACC-IRWG	Network for the Detection of Atmospheric Composition Change-InfraRed Working Group
NH	Northern Hemisphere
NIR	Near-InfraRed
OEM	Optimal Estimation Method
OPD	Optical Path Difference
RHi	Relative Humidity with respect to ice
RMS	Root Mean Square
SH	Southern Hemisphere
SON	September-October-November
SST	Sea Surface Temperatures
STE	Stratosphere-Troposphere Exchange
SVC	Sub-Visible Cirrus
SZA	Solar Zenith Angle
TCCON	Total Carbon Column Observing Network
Trans-Com	atmospheric tracer Transport model interComparison project
TRMM	Tropical Rainfall Measuring Mission
TROPOMI	TROPOspheric Monitoring Instrument
TTL	Tropical Tropopause Layer
TWP	Tropical Western Pacific
UTLS	Upper Troposphere and Lower Stratosphere
WPM	Western Pacific Monsoon

Chapter 1

Motivation and Introduction

1.1 Motivation

Over the last two decades, significant attention in the science community has been paid to studying the tropical upper troposphere and lower stratosphere as various processes in this region are known to strongly modulate global climate change. During the Northern Hemispheric (NH) winter troposphere air ascends into the stratosphere via the Tropical Tropopause Layer (TTL) mainly in this region, Tropical West Pacific (TWP) is considered the major transport pathway from the troposphere into the stratosphere during NH winter (Newell and Gould-Stewart, 1981; Fueglistaler, Wernli, and Peter, 2004; Krüger, Tegtmeier, and Rex, 2008; Rex et al., 2014). The TWP is an area extending from the Maritime Continent (Ramage, 1968) to the International Date Line, with some of the world's highest sea surface temperatures. The TWP warm pool provides the environment in which deep convective cloud systems develop (Fueglistaler, Wernli, and Peter, 2004; Fueglistaler et al., 2009; Takahashi, Luo, and Stephens, 2017). Deep convection and large-scale ascent over this region enable boundary layer air heated by the warm ocean surface to ascend to the TTL and stratosphere, changing the composition of the TTL atmosphere across the tropics. The air mass origin in the TWP region needs to be studied to properly describe the chemical species entering the stratosphere via the Stratosphere-Troposphere exchange (STE) (Holton et al., 1995) transport pathway above the TWP.

In the boundary layer, the Inter-Tropical Convergence Zone (ITCZ) is conventionally defined as a lower-tropospheric convergence region circling the globe where the tropical trade winds from the Northern and Southern hemispheres meet, typically lying between approximately 15°S and 15°N, associated with the up-welling branch of Hadley cell (Waliser and Gautier, 1993). In the TWP, the ITCZ migrates seasonally towards the warmer hemisphere relative to the other (Schneider, Bischoff, and Haug, 2014), indicating the migration of the circulation patterns in this region. The seasonal movement of ITCZ affects the upwind region to the TWP and thus determines the air mass origins in the TWP boundary layer. Moreover, the seasonal variability of the tropospheric composition in the TWP boundary plays an important role in the TTL atmosphere across the tropics via the interhemispheric transport (IHT) and the STE transport pathways. However, the mechanisms controlling its position and its relationship with the rainfall intensity are not fully understood (Schneider, Bischoff, and

Haug, 2014). Besides, the ITCZ is difficult to define over the TWP region, because the Western Pacific Monsoon (WPM) (Smith, Moise, and Colman, 2012) adds complexity to the tropical rain belt. In recent years, the advent of global atmospheric transport models such as p-TOMCAT and the atmospheric tracer transport model intercomparison project (TransCom) investigated this by non-reactive tropospheric species such as carbon dioxide (CO_2), methane (CH_4) and Sulfur hexafluoride (SF_6). The global atmospheric chemical and transport model has the potential to provided a comprehensive understanding of the differences in tracer distribution between the northern and southern hemispheres and studies IHT (Krol et al., 2018), specifically in the TWP boundary layer.

On the other hand, in the upper layer of the troposphere, the TTL is a transition region a few kilometers thick that separates the troposphere and the stratosphere and is characterized by a radiatively driven slow ascent and thus considered to be a processing region for tropospheric air to enter the stratosphere (Fueglistaler et al., 2009). The cold temperatures of the TTL dehydrate air as it ascends from the troposphere into the lower stratosphere, resulting in extreme dryness throughout the middle atmosphere. Consequently, dehydration and transport are intrinsically coupled, and associated information about dehydration is the cirrus cloud (Sassen, Wang, and Liu, 2008; Fueglistaler et al., 2009). Thus, in TTL, the presence of cirrus clouds is of particular interest not only because of its important role as the STE indicator but also the ability to modify the energy budget of the region through their radiative properties (Fu, Smith, and Yang, 2018) and the release or uptake of latent heat upon their formation or dissipation (Holton and Gettelman, 2001; Immler et al., 2008a; Spichtinger, 2014). Recent research shows that the stratospheric water vapour which mainly comes from the TTL has been increasing (Solomon et al., 2010) and this increase is closely associated with the changes in the tropopause temperature because of the global warming (Randel and Jensen, 2013; Bourguet and Linz, 2023). Moreover, cirrus cloud can interplay with the air in TTL both chemically and microphysically, altering the water vapour budget of the layer(Flury, Wu, and Read, 2012) and eventually of the stratosphere as a whole. The pathway of STE may also transport short-lived species into the Upper Troposphere and Lower Stratosphere (UTLS), which shows an ongoing net ozone depletion in the tropical lower stratosphere (LS) and has a large impact on the future presence of the ozone layer in low latitudes (Villamayor et al., 2023). Space-borne Cloud-Aerosol lidar with Orthogonal Polarization (CALIOP) aboard Cloud-Aerosol Lidar and Infrared Pathfinder Satellite Observations (CALIPSO) have partially filled the observational gap of the cirrus cloud in the last 17 years by providing observations globally (Sassen, Wang, and Liu, 2008; Martins, Noel, and Chepfer, 2011; Flury, Wu, and Read, 2012; Pandit et al., 2015). This satellite data of cirrus clouds and aerosols measured in UTLS has been reported to deepen the understanding of STE (Christian et al., 2019; Pan and Munchak, 2011). However, because of the narrow swath of the CALIOP, the repeat cycle of it is only the order of 16 days in the tropical regions (Pandit et al., 2015). Thus, the dense and continuous cirrus cloud observations from ground-based lidar over the TWP are essential.

The characterization and probe of the trace gases and cirrus clouds in the TWP region is therefore of great importance to improve the understanding of the STE transport path in this hot spot place. The column information of different trace gases, such as O_3 and CO have been probed using solar absorption FTIR spectrometry in Koror, Palau (7.34°N, 134.47°E). The FTIR instrument at the measurement station Koror, Palau is the only FTIR instrument in the center of the TWP (see Figure

3.4 for the global map of FTIR stations). The trace gas measurement from FTIR is of great importance in tracing possible sources and differentiating between types of origins of air mass. Ground-based Lidar systems have been set up there to obtain the geometrical and optical properties of the cirrus cloud over the TWP region, which fills the gap concerning the coverage of existing ground-based lidar studies in this region. Besides, the long-term observations from ground-based stations can provide intensive measurements over one specific region compared to satellite data with coarse temporal resolution. Thus, the measurements from the ground-based station in Palau can provide observational support to the long-standing assumption in this field about the STE mechanisms that the primary source region of the stratosphere air is in the TWP, which is the subject of an ongoing debate (e.g. Pommereau, 2010; Bergman et al., 2012a; Randel and Jensen, 2013; Randel et al., 2016; Boothe and Homeyer, 2017).

1.2 Aim and Outline

The aim of this study is to investigate atmospheric transport in the TWP region by a variety of means, including measurements and model simulations, and to deepen the understanding of the STE pathways characterized by seasonal variations. To reach the goal, we aim to consider the following objectives:

1. Utilize model simulations to discern the origins and transport routes of air masses within both the boundary layer and upper atmospheric layers of the Tropical Western Pacific (TWP).

2. Categorize trace gases and cirrus clouds measurements based on seasonal characteristics and air mass origins, and validate the atmospheric transport results from model simulations.

3. Explore the specificity of the TWP region to the STE mechanism and develop a scheme for the pathways of atmospheric transport over the TWP region, substantiated by measurements and model simulations.

After the finish the above work, we can be more confident of the pathways over TWP is the major source for the stratosphere air and shed light on the specificity of the TWP region to the global stratospheric climate.

This work is presented in the PhD thesis in the following outline:

Chapter 1: the motivation and aim of the thesis is presented.

Chapter 2: the scientific background which is essential to understand the thesis is given. First, the atmospheric composition and the general circulations are presented. After that, the main focus is on the tropical region. The major circulation system and the special features of the vertical structure of the tropical troposphere are reviewed. Moreover, the tropical clouds highly associated with the vertical transport are also reviewed.

Chapter 3: The measurements and the model simulations used in the thesis are introduced. First, a basic description of the ground-based observatory is given and a brief outline of the observational means and instrumentation used in this thesis is given. Then the theories of FTIR measurements and the trace gases retrieval methods are described. After that, the technique of ground-based lidar and the detection

methods for obtaining the cirrus cloud is introduced. The overview of the models including global 3-D chemical transport model, GEOS-Chem and Lagrangian integrated trajectory model, HYSPLIT is given. The basic set-ups used of the models used in this thesis are also presented.

Chapter 4: The results of the thesis. First, a tool from model simulations to determine the atmospheric chemical equator (CE), which is a boundary for air mass transport between the two hemispheres in the tropics is introduced. By this tool, the FTIR measurements are categorized by the seasonal variations and the associated air mass origins are also determined. Then, the measurement results of the cirrus cloud properties by the ground-based lidar system are presented. The back- and forward trajetory simulation of the air mass from the cloud layer are descibed later, to further complete the picture of the vertical transport over the TWP region. Finally, the horizontal transport results from CE and trace gas measurements and the vertical transport results from cirrus measurements and trajectory modeling are combined to give the final atmospheric transport schematic in the TWP region.

Chapter 5: This chapter summaries the results of this work. The futures plan are discussed in the outlook.

Chapter 2

Scientific background

2.1 Atmosphere

The atmosphere is a layer of gases surrounding celestial bodies, like Earth, due to gravity. On Earth, it consists of a mixture of gases and particles enveloping the planet. This gaseous layer provides vital protection against direct solar radiation, including harmful ultraviolet rays, and moderates temperature fluctuations. The atmosphere extends to heights of 2000-16000 kilometers above the Earth's surface.

Figure 2.1 shows the proportions of the gases that compose the atmosphere. The Earth's atmosphere is primarily composed of nitrogen dioxide (N_2, 78.1%) and oxygen (O_2, 20.9%), with a higher concentration of argon (Ar, 0.9%) compared to other noble gases (helium (He), neon (Ne), krypton (Kr), xenon (Xe) and radon (Rn)). Additionally, the remainder about 0.1% of the atmosphere contains trace gases, e.g. ozone (O_3), carbon dioxide (CO_2) and nitrous oxide (N_2O), aerosols, and cloud droplets.

Despite constituting a small fraction of the total atmosphere, these trace gases, aerosols, and cloud droplets play a significant role in atmospheric chemical and physical processes. Water vapor accounts for about 0.25% of the atmosphere's mass, but its concentration varies widely from approximately 10 parts per million by volume (ppmv) in cold regions to around 5% in hot and humid air masses, spanning over three orders of magnitude. Major greenhouse gases include water vapor, carbon dioxide (CO_2), and ozone (O_3). Other trace gases such as methane (CH_4), nitrous oxide (N_2O), carbon monoxide (CO), and chlorofluorocarbons (CFCs) also contribute to the greenhouse effect. Besides, CFCs contribute to the destruction of the ozone layer which protects human beings from the harmful wavelengths of ultraviolet light passing through the atmosphere. The atmosphere also contains molecules with carbon, nitrogen, and sulfur atoms originating from the decomposition of organisms, plant emissions, and combustion processes. These chemicals are removed from the atmosphere through oxidation processes, with the hydroxyl (OH) radical playing a crucial role. Some nitrogen and sulfur compounds are transformed into particles that are eventually removed by raindrops, leading to acid deposition on the Earth's surface. Despite constituting a tiny fraction of the atmospheric mass, aerosols and cloud droplets play essential roles in atmospheric water cycles, chemical reactions,

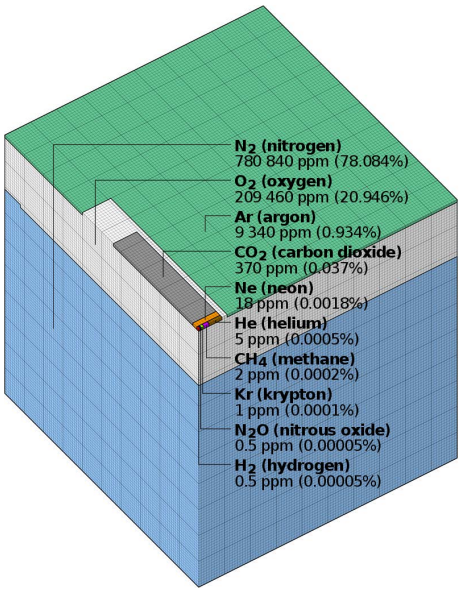

FIGURE 2.1: Visualization of composition by volume of Earth's atmosphere. Water vapour is not included, as this is highly variable. Each tiny cube (such as the one representing krypton) has one millionth of the volume of the entire block.
Data and plot are from https://en.wikipedia.org/wiki/File:Atmospheric_composition_Langley.svg , From Wikipedia, data from NASA Langley, last access: 30 November 2023.

and atmospheric optical effects such as reducing the visibility of the atmosphere and air pollution.

2.1.1 Vertical Structure of the Atmosphere

The density of air at sea level is $1.25\,\mathrm{kg\,m^{-3}}$ within a few percent (Wallace and Hobbs, 2006). Pressure and air density decrease with height, and these vertical variations in pressure and air density are much larger than the horizontal and time variations. The vertical structure of the temperature profiles for typical conditions in the Earth's atmosphere is shown in Figure 2.2. According to the vertical gradient of the temperature, the atmosphere can be divided into four layers: troposphere, stratosphere, mesosphere and thermosphere.

Troposphere

The troposphere is characterized by decreasing temperatures with height, with an average lapse rate of about 6.5°C per kilometer. This is the lowest layer of the atmosphere, extending from the surface to about 8 kilometers at the poles and 17 kilometers at the equator (see figure 2.2, right side). Its upper boundary is known as the tropopause. Almost all weather phenomena occur in this lowermost layer of the atmosphere. Tropospheric air, constituting approximately 80% of the atmosphere's mass, is continuously purified or scavenged of aerosols by cloud droplets and ice particles, some of which eventually fall to the ground as rain or snow.

The transition between the troposphere and the stratosphere is not continuous; the average height of the tropopause in the tropics is about 16 - 17 km, while in the subtropics, it is around 10 km, as shown in Figure 2.1.1 (right). However, actual observations of temperature, winds, and atmospheric trace gases indicate that there is a transition layer from the troposphere to the stratosphere, rather than at a sharp boundary "tropopause". In tropical regions, this layer is often referred to as the "tropical tropopause layer" (TTL). This will be discussed in detail later (section 2.2.2).

Stratosphere

In the stratosphere, the air is extremely dry and rich in ozone. The temperature increases with altitude due to the absorption of solar ultraviolet radiation by the ozone layer, reaching a maximum temperature of around 50 km, known as the stratopause, with a temperature of about 270 K, nearly the same as the ground level temperature. The ozone layer in the stratosphere absorbs solar radiation in the ultraviolet spectrum, which is crucial for Earth's habitability. Vertical mixing of gases in the stratosphere is strongly inhibited due to the temperature increase with height. Cloud processes have a limited impact in removing particles injected by volcanic eruptions and human activities in the stratosphere, leading to longer residence times for particles in this layer.

Mesosphere

The mesosphere is the layer above the ozone layer, extending from about 50 km above the Earth's surface to 80 km. In this layer, temperature decreases with height until it reaches the mesopause, the top of the mesosphere. This region is where most meteoroids burn up upon entering the Earth's atmosphere, creating visible trails or meteors. The mesosphere is also known for its dynamic and intricate phenomena, including the presence of noctilucent clouds, and luminescent clouds observed in high-latitude regions during summer. Additionally, the mesosphere is where the Earth's atmosphere is thin enough to support satellite orbits.

Thermosphere

The temperature increase with height in the thermosphere is due to the dissociation of molecules and the absorption of solar radiation associated with the stripping of electrons from atoms. These processes are known as photodissociation and photoionization. The photolysis of carbon dioxide in the thermosphere lead to a CO concentration greater than 50 ppm, which is almost 1000 times that of the troposphere (Grossmann, Gusev, and Knieling, 2006). Temperatures in the Earth's outer thermosphere vary significantly due to changes in ultraviolet and X-ray radiation from the sun's outer atmosphere. This layer is where Earth's auroras occur and is also the region where the International Space Station (ISS) and other satellites orbit the Earth.

2.1.2 General circulation of atmosphere

To understand the reasons behind regional climate trends, such as the focus area of this thesis, the Tropical Western Pacific (TWP) region, it is necessary to consider the

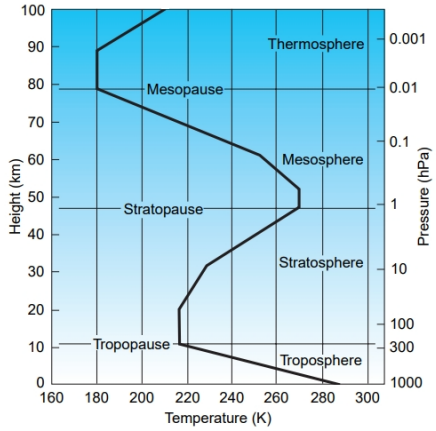

FIGURE 2.2: A typical midlatitude vertical temperature profile, as represented by the U.S. Standard Atmosphere, The figure source: Wallace and Hobbs (2006), Fig. 1.9, Section 1.3.4, Chapter 1.

changes in large-scale atmospheric circulation and assess the impact of internal climate variability. Changes in large-scale latitudinal circulation affect regional climate trends. Atmospheric circulation and ocean circulation are how thermal energy is redistributed on the Earth's surface. The Earth's atmospheric circulation varies from year to year, but its large-scale structure remains relatively constant.

In the idealized condition, there are three main circulation cells between the equator and the poles, influenced by solar radiation and the rotation of the Earth, i.e., the Hadley cell, the Ferrell cell and the polar cell, see Figure 2.3.

George Hadley proposed an axisymmetric single cell in each hemisphere in 1735 to transport heat from the tropics to the poles, giving the Hadley cell its name (Hadley, 1735). The Hadley cell is an important circulation system in the Earth's atmosphere, referring to the movement of heated, ascending air currents within a few degrees of the equator that reach the tropopause, and then gradually cool down in the upper tropical atmosphere pole-ward, moving downward at about 30 ° latitude (subtropical region). The idealized tropical circulation depicted in Figure 2.3 (top), where northeasterly (NE) and southeasterly (SE) trade winds converge near the equator, occurs in a region known as the Intertropical Convergence Zone (ITCZ). This is an important circulation system in tropical regions, which will be discussed in detail later in section 2.2. In the real Earth, ITCZ does not stay in the equator as shown in Figure 2.3 (bottom) but shifts in the tropics and tends to be seasonally towards the hemisphere that warms relative to the other (Schneider, Bischoff, and Haug, 2014). The convergence of the NE and SE trade winds causes large-scale rising of the warm and moist air and thus the ITCZ is typically characterized by heavy rain in the tropics.

The Ferrel Cell is a weak and variable atmospheric circulation cell located between the Hadley cell and the polar cell, named by William Ferrel in the 19th century (Ferrel, 1856). In this cell the air flows poleward and eastward near the surface and equatorward and westward at higher levels in the mid-latitude. The Polar Cell, on the other hand, is a circulation cell that exists near the poles, where cold and dense air descends, creating easterly surface winds known as polar easterlies. This cell is

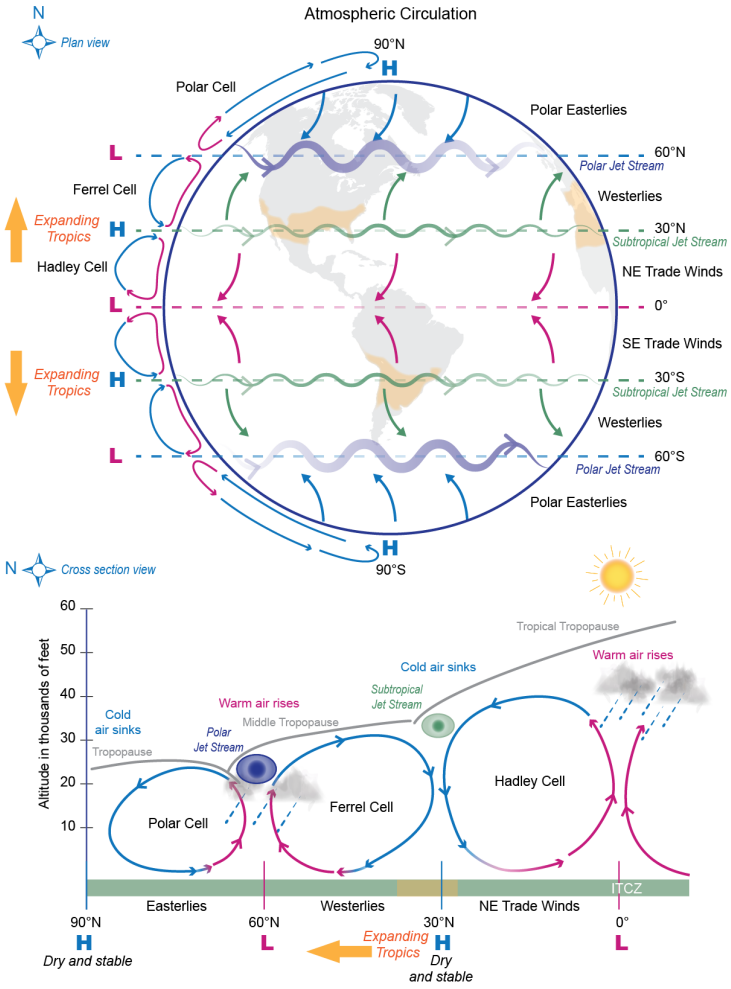

FIGURE 2.3: A schematic view of the idealized atmospheric circulation in the horizontal (top) and in the vertical cross-section (bottom). See Section 2.1.2 for further explanation. The figure source: https://science2017.globalchange.gov/chapter/5/, Climate Science Special Report (CSSR): Chapter 5: Large-Scale Circulation and Climate Variability (Perlwitz, Knutson, and Kossin, 2017).

a vital component of the overall global atmospheric circulation system, facilitating the movement of cold air from the polar regions towards the mid-latitudes.

2.2 Tropical Meteorology

The tropical regions play a crucial role in Earth's atmospheric circulation system, influencing global climate and weather patterns. These areas receive the most direct sunlight and are the warmest regions on Earth. Intense solar heating causes warm, moist air to rise, creating low-pressure areas near the equator. This further leads to the formation of NE and SE trade winds at the surface, historically influencing the choice of global trade routes. Overall, the tropical regions act as the engine driving the heat source for global circulation, propelling atmospheric movements. The

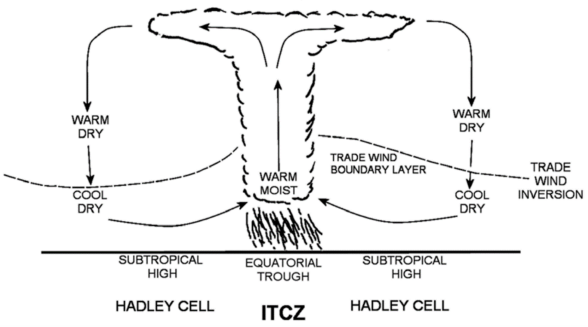

FIGURE 2.4: Idealized schematic of the ITCZ, as historically described. The figure source: Nicholson (2018), Figure 1.

Hadley cell, through the transport of heat and momentum, is crucial for maintaining global heat balance and angular momentum balance. Moreover, the tropical regions have a significant impact on global climate patterns. Phenomena like El Niño and La Niña (Bjerknes, 1969), originating in the tropical Pacific region, can cause widespread climate anomalies, affecting global weather patterns and precipitation distribution.

2.2.1 General Circulation Pattern in Tropics

The Inter-Tropical Convergence Zone (ITCZ)

The Inter-Tropical Convergence Zone (ITCZ) is conventionally defined as a lower-tropospheric convergence region circling the globe where the tropical trade winds from the Northern and Southern hemispheres meet, typically lying between approximately 15°S and 15°N (Waliser and Gautier, 1993), as shown in Figure 2.4. Generally, it is characterized by fast vertical motion and heavy rainfall and essentially acts as a meteorological barrier to cross-equatorial flow. As shown in Figure 2.5, the zonal averaged rain belt is maximum in the Northern Hemisphere (NH) in about 5 °N in July-August-September (JAS) and in about 5 °S in January-Febuary-March (JFM). The ITCZ migrates seasonally towards the hemisphere that warms relative to the other (Schneider, Bischoff, and Haug, 2014), indicating the migration of the circulation patterns in this region. Previous studies recognize the ITCZ as the boundary to Inter-Hemispheric Transport (IHT) and/or interhemispheric mixing in the tropical region (Williams et al., 2002; Stehr et al., 2002). The location of the ITCZ affects weather conditions and air mass origin throughout the tropics. The time mean or the climatology of ITCZ locations can be characterized by zonal regions of heavy rainfall in the tropics. The day-to-day features of the ITCZ, however, can be quite changeable over the landmasses and due to interactions with monsoon systems (Wang and Magnusdottir, 2006). The mechanisms controlling its position and rainfall intensity are not fully understood (Schneider, Bischoff, and Haug, 2014).

Trade Winds and Monsoon

A monsoon is a seasonal wind pattern that brings a noticeable change in weather to a region. Monsoons are characterized by a distinct shift in wind direction and speed,

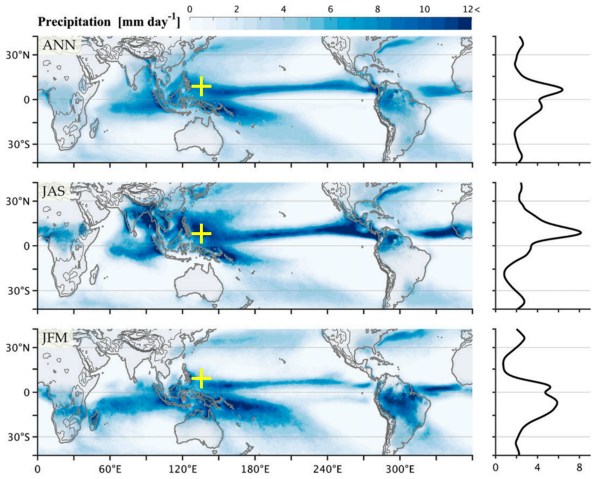

FIGURE 2.5: (left) Tropical precipitation from TRMM for 1998–2014, Annual, boreal summer (JAS), and boreal winter (JFM). (right) Zonal-mean precipitation. The location of Palau is marked by the yellow "+". The figure adapted from: Adam, Bischoff, and Schneider (2016), Figure 1.

leading to significant changes in precipitation and temperature patterns. The term monsoon also often refers to a region where there is a clear contrast between the dry NH winter and wet NH summer (for simplicity, all the following terms of seasons refers to the general NH seasons). The global monsoon region is generally defined by the difference between summer and winter precipitation in the region, and the widely used definition (Lee and Wang, 2014) is shown in Figure 2.6.

In the case of the Asian monsoon, the summer monsoon is a phenomenon resulting from the warming of the Asian continent and the cooling of the Indian Ocean, which introduces moist air and brings widespread rainfall to India, Southeast Asia, and neighbouring regions, for example, the Tropical Western Pacific region. The winter monsoon, on the other hand, is a phenomenon caused by a sharp cooling of the Asian continent and a warming of the Indian Ocean, resulting in dry and cool weather over much of Asia. For the tropics, there is a clear seasonal shift in the source of air masses in the tropics due to the north-south shift of the Asian monsoon, which feeds the tropics with air masses from the extra-tropics SH in summer and from extra-tropics NH in winter, respectively.

In addition, the rotation of the Earth and the temperature difference between the equatorial region and the subtropical high-pressure region cause the easterly winds, or trade winds, to prevail continuously near the equator. In the tropics, the prevalence of NE winds in winter and SE winds in summer similarly affects the seasonal variations in the source of air masses. The trade winds, historically important for maritime trade routes, are part of the global atmospheric circulation system and play an important role in the climate of the regions they affect.

In addition, according to models and observations, as a result of climate change, the temperature difference between the NH and SH has increased (Wang et al., 2012) and the extent of the monsoon zone is expanding, especially in Southeast Asia, by 10.6% to the west(Lee and Wang, 2014), which implies that the extent of the monsoon zone is further expanding in the Western Pacific region. The Western Northern Pacific

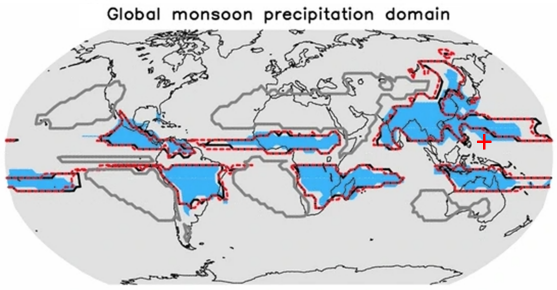

FIGURE 2.6: The global monsoon domain defined by regions where the summer-minus-winter precipitation exceeds 2.5 mm day^{-1} and the summer precipitation exceeds 55% of the annual total. The location of Palau is marked by the red "+", and it is located in the edge of the Asian monsoon domain. The figure is adapted from Lee and Wang (2014), Figure 4.

monsoon region specifies that there is the highest frequency of cyclones on Earth (Basconcillo, Cha, and Moon, 2021; Gao et al., 2020). The details about the Western Pacific Monsoon will be introduced in section 2.3.

2.2.2 Tropical Tropopause Layer (TTL)

As mentioned in Section 2.1.1, the boundary between the troposphere and stratosphere is the tropopause which is captured by the very sharp difference in the temperature lapse rate. However, in the tropics, this is not the real situation. It has been accepted for almost two decades (Highwood and Hoskins, 1998; Holton and Gettelman, 2001; Fueglistaler et al., 2009) that there is a transition layer between the upper troposphere and the lower stratosphere (UTLS). It has been known as the Tropical Tropopause Layer (TTL). Since TTL is characterized by the features of both the upper troposphere and lower stratosphere, it is best defined as a layer extending over several kilometers rather than as a sharp boundary.

Many studies, e.g. Gettelman et al. (2009), Fueglistaler et al. (2009), Gettelman et al. (2004), and Folkins et al. (1999) have been made and focused on the physical and chemical processes of the TTL, and different upper and lower boundaries are taken into consideration because of the different central points of these studies. Figure 2.7 shows the different definitions of the TTL by previous studies.

The first definition used in this study is shown by layer A (see Figure 2.7). The level of Minimum of the Stability (LMS) identifies the lower limit of the TTL (Sunilkumar et al., 2017) or the Lapse Rate Minimum (LRM) typically around 10 - 12 km (Gettelman and Forster, 2002), which is the level of the minimum potential temperature gradient. This level is also characterized by the minimum ozone (O_3 min). The level of the Cold Point Tropopause (CPT) which is the level of temperature minimum (Highwood and Hoskins, 1998; Gettelman and Forster, 2002) or the Lapse Rate Tropopause (LRT; World Meteorological Organization, 1957) is used to identify the upper limit of TTL which is about 17 km. The layer between the LMS / LRM and CPT / LRT is a commonly used definition of the TTL (Folkins et al., 1999; Gettelman and Forster, 2002; Gettelman et al., 2004; Sunilkumar et al., 2017; Pan et al., 2018;

Cairo et al., 2021). The example upper and lower limit definitions of TTL and its features over Palau are discussed in detail in Section 2.3.

Some studies, for example, Immler et al. (2008a), Sherwood (2000), and Folkins, Oltmans, and Thompson (2000), focused on the radiative effect of the clear sky in TTL, and the TTL is the region where a transition of the background clear sky radiative heating from net cooling to net heating (see the blue and red arrows in Figure 2.7) takes place. In this definition, the Level of Zero net Radiative Heating (LZRH) is used to determine the lower limit of TTL.

Fueglistaler et al. (2009) argued for the definition of the upper limit of the top of the thermal troposphere (CPT/LRT) and proposed a Level of Highest Convective Overshooting (LHCO) tops that can reach about 18.5 km (70 hPa). Previous studies have demonstrated, using radio soundings (Gettelman and Wang, 2015; Birner, Sankey, and Shepherd, 2006) and cirrus cloud observations (Immler et al., 2007; Immler et al., 2008a), that there is a maximum static stability layer (Pilch Kedzierski, Matthes, and Bumke, 2016) within 2 km of thickness above the conventional top of the thermal troposphere (CPT/LRT). In this layer, the trace gases such as O_3 and CO also show a large vertical gradient (Schmidt et al., 2010; Park et al., 2007), which implies the need for a higher upper limit of the TTL as the air eventually transits into the lower stratosphere.

From LZRH (around 15 km) to a level (around 18 km) above the CPT and below LHCO is the second definition of TTL, denotes by "B" (Figure 2.7), commonly used for the study of the radiative effect in TTL (Fu, Hu, and Yang, 2007; Immler et al., 2008a; Dessler, 2002; Sherwood and Dessler, 2001; Sherwood, 2000). The definition "C" of TTL placed the lower limit to the Level of Main Convective Outflow (LMCO) which is also the Level of Neutral Buoyancy (LNB) in around 14-15 km. The top boundary of TTL is LHCO, where there are rare cases of overshooting tops that can penetrate TTL into the stratosphere(Fueglistaler et al., 2009; Jensen et al., 2010). Even though this is the most synthesis definition incorporating most previous research on this topic (Henz, 2010), the exact level of LHCO is difficult to quantify compared with the thermal tropopause CPT / LRT and varies in different places and seasons. So this study will use the first definition (definition "A", shown in Figure 2.7) to quantify the TTL region but also include the discussion about the layer of 1 - 2 km above CPT as TTL region where several cases of cirrus cloud are observed above Palau, see details in Section 4.3 and 4.4.

2.2.3 Tropical Clouds and dehydration process

Clouds form when air is lifted to a saturation point by fronts, topography, convergence or convection. Warm clouds have temperatures above 0°C, while cold clouds have temperatures below 0°C. Mixed-phase clouds have ice crystals and super-cooled droplets. In higher altitudes above 10 km, clouds contain mainly ice crystals (Cairo et al., 2021). In the lower and middle troposphere, tropical clouds are dominated by cumulonimbus. In higher altitudes, cirrus clouds dominate in the range of the TTL.

The process of atmospheric dehydration is closely related to cloud formation. Dehydration refers to the process of water molecules in the atmosphere transitioning from a gaseous state to a liquid or solid state (Henz, 2010). When air rises, it cools down in the atmosphere, causing water vapour to condense into small water droplets or ice

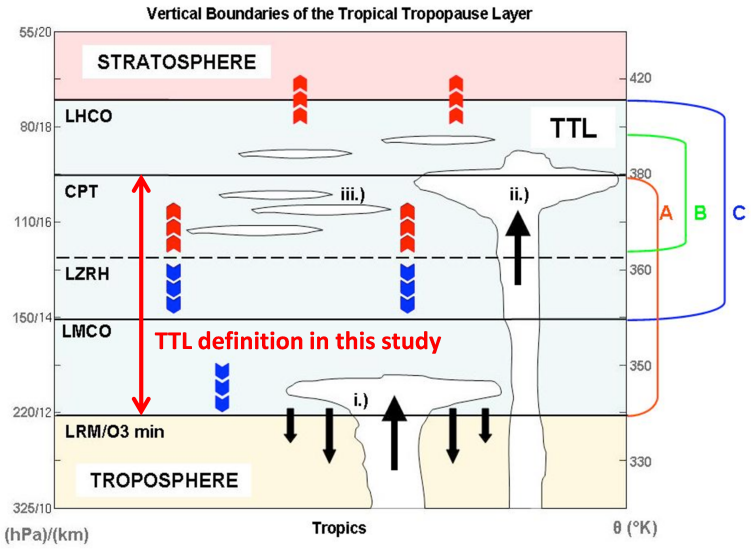

FIGURE 2.7: Vertical boundaries of the Tropical Tropopause Layer, see section 2.2.2 for the explanation. The definition of TTL used in this study is marked by the red bidirectional arrow, namely the definition "A". The figure is adapted from Henz (2010), Figure 1.

crystals, which is the dehydration process forming clouds. This process is known as condensation. Clouds are composed of water droplets or ice crystals depending on the temperature as mentioned before, suspended in the atmosphere, forming cloud layers.

The process of dehydration in the atmosphere is a prerequisite for the formation of clouds and precipitation. When water vapour in the atmosphere condenses into clouds, the moisture content in the atmosphere decreases, indicating dehydration. The water droplets or ice crystals in the cloud layer may eventually return to the Earth's surface in the form of precipitation, replenishing surface water sources.

The convection process is highly related to the cumuli-form cloud. Air parcels are lifted through the convection process to their saturation point and form a cumulus cloud. The air parcels continue to ascend until there is a level where the air parcels become as cool as the surrounding air. This level is the Equilibrium Level (EL) or the LNB as mentioned before. The parcels do not stop immediately but oscillate and spread out to form an anvil-shaped cloud top (Pfister et al., 2001; Comstock and Jakob, 2004). Therefore, EL/LNB is also the main outflow of the convection, which is also called LMCO (Henz, 2010), as mentioned in section 2.2.2. This anvil-shaped cloud can detach from the main body of the cumulus cloud flow in the TTL region and form a thin layer of cloud that only contains ice-crystal, which is called a layer of cirrus cloud.

Another rare but also important process after the convection cloud penetrates the EL is overshooting. During intense convective activity, such as severe thunderstorms, updrafts of warm, moist air parcels can be so strong that they push the top of the cloud system above the EL and into a higher altitude, forming a dome-shaped overshooting top. It occurs when the convective updrafts are exceptionally powerful, allowing the cloud tops to penetrate the stable layer of TTL and intrude into the stratosphere (Danielsen, 1982; Fueglistaler et al., 2009; Pommereau, 2010; Wu, Fu,

and Kodama, 2023). So the detection of the overshooting top is recognized as an indication of the troposphere air penetrating the stratosphere. However, as mentioned before, the detection of overshooting is challenging because of its small spatial and temporal scale. This process is rare and the condition for the forming of such intensive overshooting tops that can penetrate the TTL is limited (Fueglistaler et al., 2009; Pope and Fry, 1997). Other processes can also play a role in the transport from the troposphere into the stratosphere associated with anvil-shaped and cirrus clouds in TTL (Fueglistaler et al., 2009; Henz, 2010; Cairo et al., 2021).

Cirrus is one genus of clouds forming at high altitudes made of ice crystals, which is also a dominant type of cloud with high frequency in the TTL. The global occurrence of cirrus cloud coverage based on satellite measurement is 16.7% (Sassen, Wang, and Liu, 2008). In tropical regions, the occurrence of cirrus is higher (Sassen, Wang, and Liu, 2008; Sassen, Wang, and Liu, 2009), and the frequency can be up to 70% (Wang et al., 1996). The formation mechanism of the cirrus can be summarized by five types (Sassen, Wang, and Liu, 2008): synoptic, mountain-wave updraft, contrail-cirrus, injection cirrus, and "cold trap" (Holton and Gettelman, 2001). The synoptic types are relative to the jet stream and low-pressure system which is a common process of cloud forming in the mid-latitudes (Sassen, Wang, and Liu, 2008; DeMott, 2002). In addition to mountain-wave updraft and contrail-cirrus controlled by terrain and human factors, the latter two are cloud formation mechanisms that mainly happen in tropical regions considering the strength and speed of the uplifts (Krämer et al., 2016).

The injection cirrus is usually called convective forming cirrus. Large amounts of water vapour and cloud nuclei are uplifted by fast and intensive vertical rising air masses in the convective activities. This deep convective mix-phased cloud generates widespread anvils in high altitudes where the temperature is very low and the freezing of the liquid droplets forms long-lived cirrus (Pfister et al., 2001; Comstock and Jakob, 2004). The convective forming cirrus is always linked to the interhemispheric transport between the two hemispheres and is usually indicated by ITCZ (Waliser and Gautier, 1993). Moreover, there is a tool called Chemical Equator (CE) that provides a more accurate picture of the interhemispheric exchange (Sun et al., 2023), which can also related to the hotspot region for the tropical convective forming cirrus.

The last forming mechanism of cirrus cloud in the TTL, the cold trap, is generated by cooling and freezing from the slow and large-scale uplifting (Jensen et al., 1996; Holton and Gettelman, 2001) and atmospheric temperature anomaly by Kelvin or gravity wave activity in the TTL region (Immler et al., 2007; Fujiwara et al., 2009). The air rising from the troposphere to the stratosphere is readily dried to saturation pressure over ice so the cirrus cloud with very low Cloud Optical Depth (COD) is formed by this process in the TTL region (Spichtinger et al., 2003; Jensen et al., 2005). This cloud-forming mechanism which is described by the dehydration process, suggests that the horizontal advection rather than vertical motion in the TTL flows into the cold trap (Holton and Gettelman, 2001) where the temperature is extremely cold and can favor the dehydration process of the air in this region then releasing latent heat through the adiabatic ascent in the cold trap (Schoeberl et al., 2019). Bergman et al. (2012a) from the trajectory modeling, they concluded that in summer, the air over the Indian subcontinent is the main source of fresh air eventually being transported into the stratosphere. In contrast, in winter, air moves slowly upward into the stratosphere mainly from the Western Pacific region (Fueglistaler, Wernli, and

Peter, 2004). Besides, More air enters the stratosphere from the troposphere in winter as opposed to summer (Bergman et al., 2012a; Bergman et al., 2012b; Randel and Jensen, 2013).

Cirrus is usually categorized by the COD as Sassen and Cho (1992) suggested. For COD higher than 0.3, it is thick and opaque cirrus; for COD between 0.03 and 0.3, it is optically thin cirrus; and for COD less than 0.03, it is the sub-visible cirrus (SVC). The SVC is often formed in situ by slow and synoptic-scale uplift compared to cirrus with higher COD which is often related to deep convection (Haladay and Stephens, 2009; McFarquhar et al., 2000). The existence of the SVC was first established from airborne in-situ measurements (e.g. Heymsfield, 1986) and ground-based lidar observations by Sassen and Cho (1992). The dehydration of tropospheric air before it enters the stratosphere is related the occurrence of SVC (Reverdy et al., 2012).

2.3 the Tropical Western Pacific Warm Pool

The Tropical West Pacific (TWP) region is an area extending from the Maritime Continent (Ramage, 1968) to the International Date Line with the world's highest sea surface temperatures (SST, above about 28°C year round) and is noted to be a tropical warm pool, shown in Figure 2.8. The warm pool provides the environment in which deep convective cloud systems develop. As mentioned before, the warm waters in this region act as a reservoir of thermal energy. This heat drives atmospheric circulation, including the Hadley Cell, which is a major component of the Earth's general circulation system. It plays a vital role in redistributing heat from the tropics toward the poles, influencing global weather patterns. The TWP warm pool is closely linked to El Niño and La Niña events (Bjerknes, 1969), and changes in the TWP warm pool can influence the onset, intensity, and duration of these events, leading to widespread climate impacts. Besides, the tropospheric air ascends into the stratosphere via the TTL mainly in this region, The TWP region is therefore considered as the major transport pathway from the troposphere into the stratosphere during winter (Fueglistaler, Wernli, and Peter, 2004; Krüger, Tegtmeier, and Rex, 2008; Newell and Gould-Stewart, 1981). Recent studies have revealed the very low ozone content inside the tropical warm pool region, leading to a low oxidative capacity in this region (Rex et al., 2014). The specific low oxidative capacity in this region favours the relatively longer lifetime of short-lived species such as NOx and halogen species compared with other tropical regions and exacerbates the ozone depletion in the tropical lower stratosphere (Villamayor et al., 2023). Thus, the tropospheric chemical composition above the TWP influences the stratospheric composition on a global scale (Rex et al., 2014; Müller et al., 2023c).

2.3.1 Cold Trap and Stratosphere-troposphere Exchange (STE)

The TTL over the TWP warm pool is the so-called "cold trap" (Holton and Gettelman, 2001) which refers to a layer of the atmosphere that is substantially colder than both the lower and higher layers. This specific temperature structure plays an important role in the Stratosphere-troposphere Exchange (STE). It is recognized as the major source of the stratosphere air in winter when the TTL is extremely cold (Fueglistaler, Wernli, and Peter, 2004; Fueglistaler et al., 2005; Immler et al., 2008a).

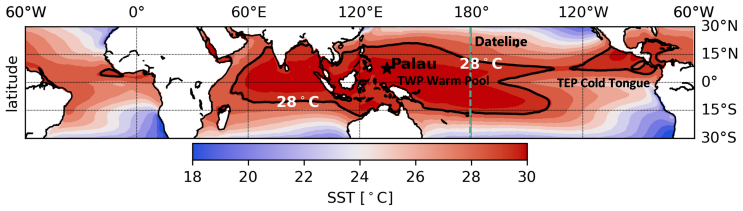

FIGURE 2.8: SST (in °C) in the tropical region averaged from 2015 to 2022. The black line shows the isothermal line of 28 °C. The green dashed line shows the Dateline in 180 °. The location of Koror, Palau is marked in the plot. TWP Warm plot: Tropical Western Pacific warm pool. TEP cold Tongue: Tropical Eastern Pacific Cold Touge. The SST data is obtained from the Ocean Surface Diagnostics of MERRA-2 (The second Modern-Era Retrospective analysis for Research and Applications) reanalysis, Global Modeling and Assimilation Office GMAO (2015).

Figure 2.9 shows the annual mean cross-section of tropical ($\pm$ 30°N) zonal temperature as a function of longitude and pressure/altitude. Over the TWP warm pool region (100°E - 180°), the zonal temperature shows a structure of the lower temperature from 120 hPa (15.5 km) to 90 hPa (17.5 km) and the minimum center at about 100 hPa. This cold trap structure exists as a climatology phenomenon over the TWP region, but the value of the minimum temperature of the cold certer (about 194 K) is reduced by the annual averaging. Figure 2.10 shows maps of monthly mean temperature at 100 hPa for January and July from 2012 to 2022 within the tropics ($\pm$ 30°N). The temperatures show a specific spatial structure in January with a gradient of the temperature up to 5 K within the inner tropical region ($\pm$ 10°N) from 194 K decreasing to 189 K. The coldest center is located over the TWP region in January as shown by the white dashed line of the isothermal of 189 K in Figure 2.10. In July, the gradient of the temperature is less intensive and the cold center extends toward the north and east, over the TWP and Indian/Southeast Asian monsoon region.

The temperature structure of the TTL region is a key determinant of air transport (Immler et al., 2008b; Fueglistaler et al., 2009). As described in section 2.2.3, when the temperature of an air mass is higher than that of the surrounding air, a dehydration process occurs in which the latent heat of the air mass is released and causes an upward movement of the air mass. This process also applies to the air parcels in the TTL, except that this upward motion is a slow, large-scale uplift, unlike the rapid vertical process in the lower troposphere (Holton and Gettelman, 2001). When the TTL air mass drifts horizontally through the large-scale circulation into a cold trap, the low-temperature conditions here enable the air mass to further release latent heat and rise finally into the stratosphere.

Figure 2.11 gives a schematic of the classical four transport paths for STE in the tropics. The free troposphere below the TTL is characterized by weak large-scale downwelling interrupted by strong upward motion relative to the convective updrafts (Bergman et al., 2012a). In the tropics, air masses converge and lift in the troposphere to form cumulonimbus clouds, in which they rise and mix with the surrounding air before finally breaking away from the cumulonimbus. Cumulus clouds vary in intensity depending on the magnitude and speed of vertical motion. Air

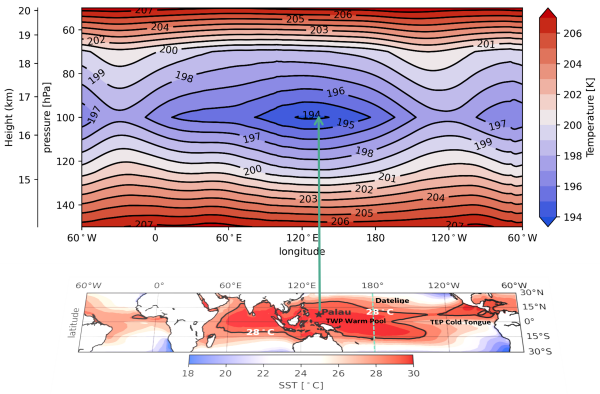

FIGURE 2.9: Upper part: Maps of zonal cross sections of meridionally averaged temperature (in K, annually averaged 2012-2022) from 150 to 50 hPa in latitude range of $\pm$ 30°N. Lower part: Sea surface temperature (SST, in °C) in the tropical region averaged from 2015 to 2022 (2.8). The upper cold center is well above the lower warm center where the site Palau is located, as shown by the green arrows in the plot. The temperature data in pressure level are from the ERA5 reanalysis data (Hersbach et al., 2020). The sea surface temperature is from the Ocean Surface Diagnostics of MERRA-2 (The second Modern-Era Retrospective analysis for Research and Applications) reanalysis, Global Modeling and Assimilation Office GMAO (2015).

masses converge and lift into the free troposphere and reach the LNB/EL as mentioned in Section 2.2.3. After the air flows into the TTL, there are four main paths relative to different atmospheric conditions in TTL and the strength of convective activities.

- Path 1. After the air parcel reaches LNB/EL, and the latent heat of the parcels is fully released, it will not stop abruptly. The air parcel travels upward before it exhausts all of its momentum. The upward acceleration ceases as it becomes colder than the environmental temperature, but its momentum propels the air parcel to a higher level and reaches the maximum parcel level (MPL) or LHCO (Fueglistaler et al., 2009). Through this extremely deep convection cell, the air parcel can penetrate the stable layer of TTL and form an overshooting top intruding into the stratosphere (Danielsen, 1982; Fueglistaler et al., 2009; Pommereau, 2010; Wu, Fu, and Kodama, 2023). This pathway plays an important role in the STE, particularly in favour of the injection of short-lived chemically active species, i.e., NOx, Br_y, I_y, and CO, into the stratosphere before they can be removed by atmospheric oxidation reactions (Pommereau, 2010).

- Path 2. After the air parcel is detrained away from the deep convective cell, it flows through the TTL region and eventually descends to low altitudes unless it encounters a region where the ambient temperature is lower than that of the air parcel, i.e., the cold trap over the TWP in winter and the Indian subcontinent in summer (Bergman et al., 2012b). This process is related to the mix-phased deep convection cell that reaches the TTL and generates widespread anvils in a high layer of TTL where the temperature is very low and the freezing of the liquid droplets forms long-lived cirrus (Pfister et al., 2001; Comstock and Jakob, 2004).

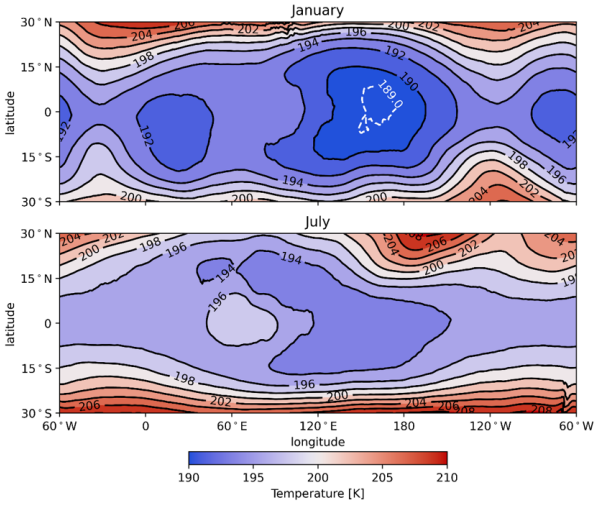

FIGURE 2.10: Maps on 100 hPa of January and July averaged temperature (in K, monthly averaged 2012-2022) fields. The temperature data are from the ERA5 reanalysis data (Hersbach et al., 2020)

- Path 3. The air parcel is detrained in the lower boundary of the TTL, i.e., LNB/EL. Then it descends into the free troposphere.

- Path 4. The same as the beginning transport path of Path 2, after the air parcel is detached from the deep convective cell, it flows through the TTL region. However, because of the circulation in the TTL, the air parcel flows into the cold trap where the temperature is extremely cold and can favour the dehydration process of the air then finally enters the stratosphere. The dehydration of tropospheric air before it enters the stratosphere is typically related to the occurrence of SVC in the previous studies, e.g. Reverdy et al. (2012), Immler et al. (2007), and Martins, Noel, and Chepfer (2011), which is often formed in situ by slow and synoptic-scale uplift in the cold trap and stays a very long time (Martins, Noel, and Chepfer, 2011).

Air parcel transport through Path 1 and Path 4 can finally reach the stratosphere. The commonality of the two paths is the air parcel is initially uplifted to TTL from the convection process in the tropics. The location of the active convection is related to the ITCZ/CE (Cairo et al., 2021; Sun et al., 2023), which shifts seasonally northsouthwards to the hemisphere that warms relative to the other (Schneider, Bischoff, and Haug, 2014). The locations with significant strong convective activities in the tropics are the TWP region (Fueglistaler, Wernli, and Peter, 2004; Fueglistaler et al., 2005; Bergman et al., 2012a) and the Asian monsoon region (Fueglistaler et al., 2005; Randel and Jensen, 2013).

The scheme of Path 1 is associated with the fast overshooting of adiabatically cooled air uplifted with deep convective systems (Danielsen, 1982; Pommereau, 2010). Overshooting processes are rare on a global scale and the conditions under which they form are very demanding (Fueglistaler et al., 2009). However, the rapid overshoot process prevents short-lived species from being removed during the vertical transport through oxidative reactions in the troposphere. It plays a vital role in the vertical transport of boundary layer pollutants, especially short-lived species, to the upper troposphere and lower stratosphere, with important implications for stratospheric ozone and climate (Wu, Fu, and Kodama, 2023).

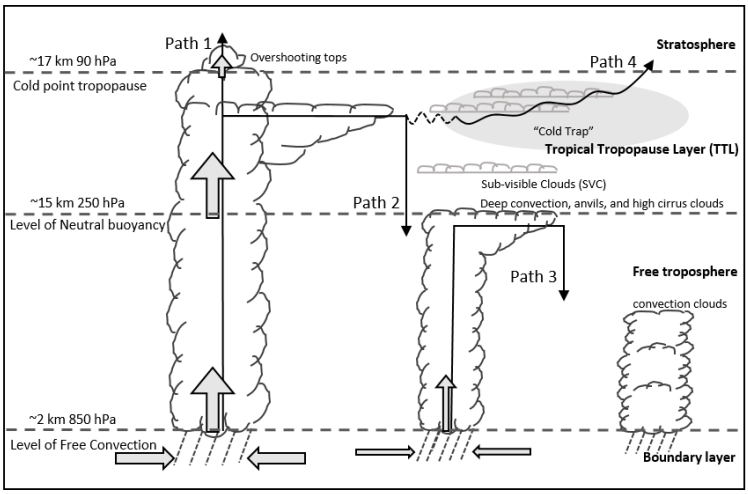

FIGURE 2.11: A schematic of transport paths of Stratosphere-troposphere Exchange (STE) in the tropics.

Path 4, on the other hand, is a large-scale uplift process in which the air mass is in the stratosphere vertically for a much longer period than in path 1 (> 60 days, Gettelman and Forster, 2002; Dessler, 2002). Only the air parcel that flows into the cold trap can continuously release the latent heat and slowly ascend because of the lower ice saturation point in the cold trap. However, it has been argued that given the long time it takes for Path 4, short-lived species will be deactivated through the slow vertical transport process. The air masses that make it into the stratosphere in Path 4 do not contain short-lived species, so there will be little effect on the atmospheric composition of the stratosphere, especially ozone (Pommereau, 2010).

In the TWP region, both Path 1 and Path 4 happen. It has been recognized that the deep overshooting conventions appear frequently in the western Pacific warm pool (e.g. Fueglistaler, Wernli, and Peter, 2004; Fueglistaler et al., 2009; Wu, Fu, and Kodama, 2023). The cold trap over the TWP region in winter is also with exceptionally low temperatures, which favors the STE by Path 4. The TWP region is therefore considered as the major transport pathway of STE (e.g. Newell and Gould-Stewart, 1981; Holton and Gettelman, 2001; Fueglistaler et al., 2005; Krüger, Tegtmeier, and Rex, 2008; Rex et al., 2014; Müller et al., 2023c).

2.3.2 Low-ozone high water structure

The composition of the stratosphere is mainly determined by species that ascend from the troposphere into the stratosphere. The reactions with OH in the troposphere break down most short-lived species. The major source of OH in the clean troposphere is formation through:

$$O_3 + hv \longrightarrow O(D) + O_2 \,, O(D) + H_2O \longrightarrow OH + OH$$

The reaction shows that the oxidizing capacity of tropospheric is air closely related to the ozone concentration (Levy, 1971; Jaeglé et al., 2001).

High SST favors strong convective activity, which can lead to low O_3 concentration in the TWP region, where the air temperature is the highest globally and O_3 lowest

(e.g. Kley et al., 1996). In the warm and humid tropical marine boundary layer, this particular loss mechanism is very efficient (Kley et al., 1997). Besides, the TWP area is far away from industrial human activity areas, which is influenced by the monsoon and the ITCZ, and only receives long-distance transported air masses from East Asia in winter. It is largely free of air pollution from local sources, especially NOx, for the chemical production of O_3 in the troposphere. Both factors result in the tropospheric O_3 column being at the lowest level in the TWP region throughout the year (Rex et al., 2014; Müller et al., 2023a).

The corresponding O_3 and OH concentrations simulated by the GEOS-Chem model are shown in Figure 2.12, with low concentrations of O_3 and OH in the TWP region. The cross-sections of the meridionally averaged O_3 and OH simulated from GEOS-Chem in the tropical region from surface to 18 km in the latitude range of $\pm$ 30°N are shown in Figure 2.13. The OH is lower than elsewhere in the tropics in the vertical extent from the surface to about 17 km. These low values of OH and O_3 in the TWP region have a large impact on prolonging the lifetimes of short-lived species, i.e., NOx, Br_y, I_y, and CO. As mentioned before, the air mass can transit into the stratosphere via Path 4 (see Figure 2.11), which takes more than 60 days Gettelman and Forster, 2002; Dessler, 2002 and is longer than the typical lifetime of those short-lived species. Considering the low oxidizing capacity of the TWP region, especially in cold traps, short-lived species can survive and enter the stratosphere before being removed by oxidative reactions with OH (Rex et al., 2014; Müller et al., 2023b).

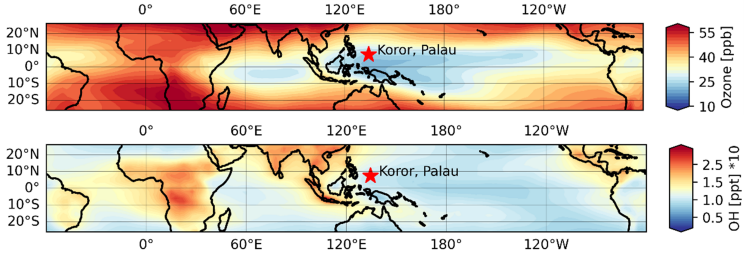

FIGURE 2.12: Tropospheric columns of O_3 (upper plot) and OH (lower plot) simulated from GEOS-Chem (average in 2016-2020) in the tropical region (in latitude range of $\pm$ 30°N). The red mark is site Koror, Palau.

2.3.3 Walker circulation, El Niño and La Niña

The Walker Circulation is a large-scale atmospheric circulation pattern spanning the tropical Pacific Ocean. It is named after the British scientist Sir Gilbert Walker, who studied and identified this phenomenon in the early 20th century (Bjerknes, 1969). As shown in Figure 2.8, there is a temperature contrast between the warm pool in the western tropical Pacific and a cold tongue of water in the eastern tropical Pacific. The Walker Circulation is driven by this temperature contrast, which is a rising branch over the warm pool surplus heating region and a sinking branch over the east Pacific cooling region (see Figure 2.14a).

The main variability of the Walker Circulation is the El Niño-Southern Oscillation (ENSO), a coupled atmospheric-oceanic phenomenon driven by SST anomalies with

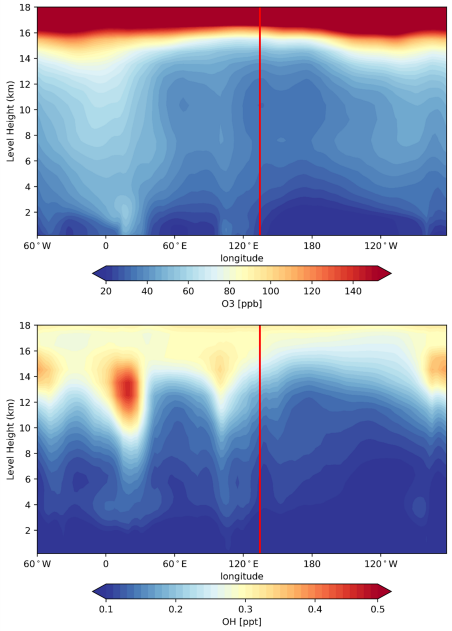

FIGURE 2.13: Maps of zonal cross-section of meridionally averaged O_3 (upper plot) and OH (lower plot) simulated from GEOS-Chem (average in 2016-2020) in the tropical region from surface to 18 km in latitude range of $\pm$ 30°N. The red mark is the location of the site Koror, Palau.

a period of 2-7 years. The normal Walker circulation is accompanied by cold up-welling in the east and warm SSTs in the west, as shown in Figure 2.14a. The strongest up-welling branch of the Walker circulation is located in the TWP region, however, SST anomalies can affect the entire tropics, influencing precipitation on several continents near the equator, from Africa to Asia to South America, as shown by the thinner blue arrows in Figure 2.14a.

During the El Niño events, the typically warm pool in the TWP region moves towards to the east Pacific, leading to a shift in the rising branch of the Walker circulation eastwards, as shown in Figure 2.14b. This alteration in the circulation pattern results in a redistribution of global precipitation. For example, in the El Niño pattern, the usual rising branches in the TWP and South America are replaced by anomalous sinking branches, leading to reduced precipitation in these regions.

On the other hand, during La Niña events (Figure 2.14c), the warm pool in the TWP is warmer than the ENSO-neutral conditions and meanwhile, the east Pacific is cooler than usual. The up-welling branches in the TWP and northern South America are stronger and cause anomalous high precipitation in this region. Meanwhile, the anomalous down-welling branches are located in North Africa, leading to a deficiency of precipitation during these events.

It is important to note that the ENSO pattern described and shown above is typically idealized. The reality of coupled atmosphere-ocean phenomena is complex and variable. Since SST anomalies in the warm pool region are the driving factor of ENSO, it has a higher correlation with changes in monsoon circulation and precipitation in the Pacific compared to other tropical regions. During El Niño events, drought conditions usually occur, especially in eastern Australia, while negative SST anomalies

occur in the TWP and eastern Indian Ocean. During La Niña, an increase in rainfall is observed over the TWP with positive SST anomalies in the western Pacific and eastern Indian Oceans.

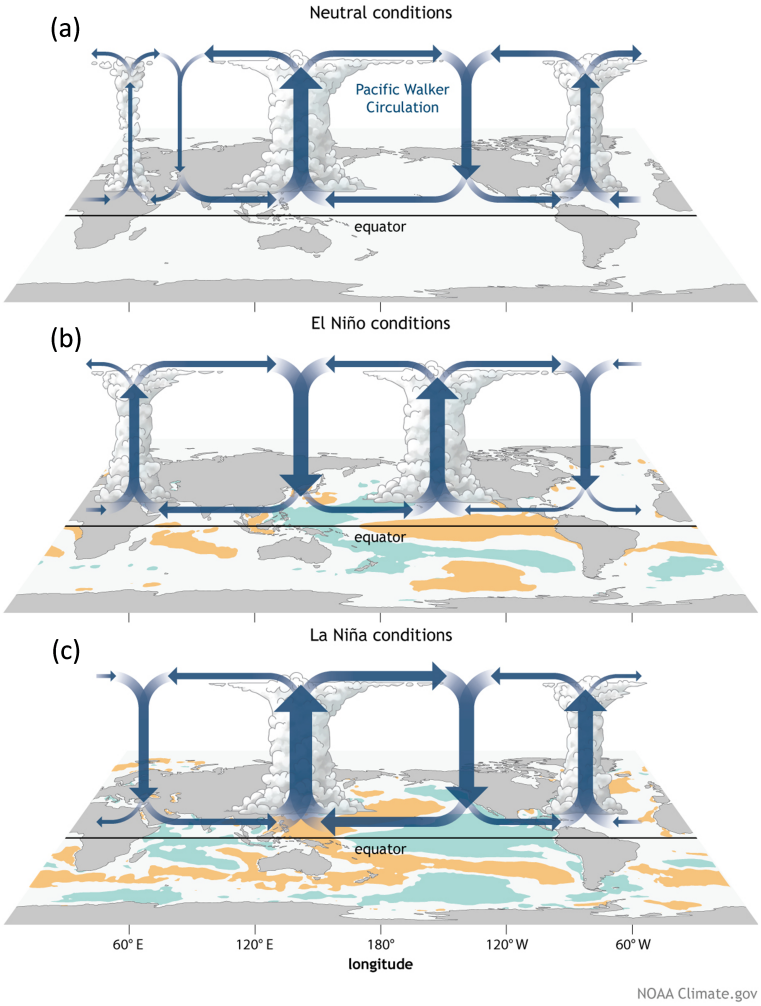

FIGURE 2.14: Generalized Walker Circulation (December-February) during (a) ENSO-neutral conditions, convection associated with rising branches of the Walker Circulation is found over the Maritime continent, northern South America, and eastern Africa.; (b) El Niño events, overlaid on a map of averaged SST anomalies. Anomalous ocean warming in the central and eastern Pacific (orange) helps to shift a rising branch of the Walker Circulation to the east of 180° while sinking branches shift to over the Maritime continent and northern South America; and (c) La Niña events, overlaid on map of average SST anomalies. Anomalous ocean cooling (blue-green) in the central and eastern Pacific Ocean and warming over the western Pacific Ocean enhance the rising branch of the Walker circulation over the Maritime Continent and the sinking branch over the eastern Pacific Ocean. Enhanced rising motion is also observed over northern South America, while anomalous sinking motion is found over eastern Africa. (Loberto, 2014) The figure source: https://www.climate.gov/media/13542, NOAA Climate.gov, by Fiona Martin, last access 30 November, 2023

Chapter 3

Measurements and Models

To make the study of characterization of the trace gases such as O_3, CO and CH_4 of the tropospheric TWP region, measurements and model simulations are used. An important aim of this study is to deepen the knowledge of the pathway of the STE over the TWP region, for this, I use cirrus cloud observations combined with model simulations. Most of the measurements are from the Palau Atmospheric Observatory (PAO), located in the TWP region, and it is equipped with comprehensive instruments for atmospheric measurement. Auxiliary data for daily meteorology conditions are from Palau Weather Station (PWS). Analysis of the observational data products is closely combined with model simulations. The 3-D chemical transport model GEOS-Chem version 13.0.0 (Bey et al., 2001) is used for the study of the characterization and origin sources of the trace gases and cirrus clouds. The trajectory model HYSPLIT (Air Resources Laboratory's (ARL) Hybrid Single-Particle Lagrangian Integrated Trajectory model) is used for the study of the STE.

In this chapter, I will first describe the station base PAO which contains most of the instruments I used for this thesis in Section 3.1. Then thorough descriptions of the Fourier Transform Infrared (FTIR) Spectrometer and how I obtain the trace data products of trace gases from FTIR spectrometer are in Section 3.2. The cirrus cloud data products are measured and retrieved from a Gound-based Lidar system. The theoretical background of the lidar system and the method for retrieving cloud products are described in Section 3.3. The descriptions and set-ups of models are given in Section 3.4.

3.1 The Palau Atmospheric Observatory

The TWP region is of great importance for the study of the STE but has been reported and recorded as a measurement gap of the atmospheric composition such as O_3 and cirrus cloud. The Palau Atmospheric Observatory (PAO) was established to conduct comprehensive atmospheric measurements above the TWP region to fill in the gap.

PAO was established in 2015 in the Palau Community College (PCC), in the middle of downtown Koror, Republic of Palau, see figure 3.1(Müller et al., 2023c; Müller, 2020). It was funded under the EU-funded StratoClim (Stratospheric and upper

tropospheric processes for better Climate predictions, 2015-2019) project at the beginning of the operation period. Since 2019, measurements have been conducted and funded by Alfred-Wegener-Institut (AWI) with further contributions from the Institute of Environmental Physics (IUP), University of Bremen.

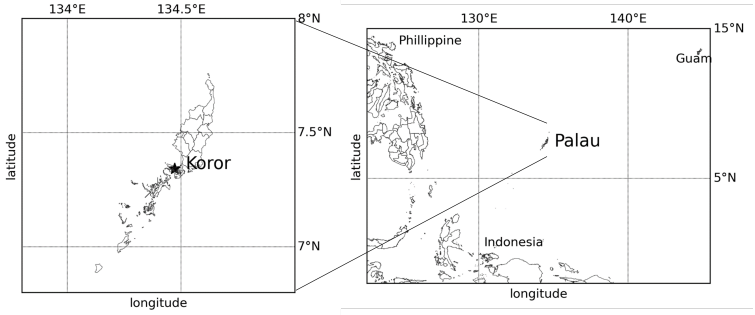

FIGURE 3.1: Maps of the location of Koror, Palau. The site is located in Koror (marked on the left side of the map), the main commercial centre of the Republic of Palau.

Two scientific laboratories are held separately in two containers. One is used for measurement of the atmospheric particles, namely cirrus clouds in TTL and stratospheric aerosol in high altitude by a micro lidar, The COMpact Cloud Aerosol Lidar (COMCAL). The other is used for measurement of the atmospheric trace gases by a Fourier-transform infrared (FTIR) spectrometer. Besides, some space of the laboratories are made for a Pandora 2S photometer and weather balloon soundings with O_3, water vapour, aerosol, and radiosondes. The following part will give a short description of the equipment that is relevant to this study.

FIGURE 3.2: Picture of the outward appearance of PAO.

Grond-based Fourier-transform infrared (FTIR) spectrometer

The ground-based FTIR spectrometer measures the solar spectrum in clear sky conditions to retrieve the abundance of trace gases, such as CO, O_3 and CH_4. It has been operated since 2016 and we obtain a large number of spectrum in different months. By retrieval algorithm, we can obtain a variety kinds of trace gas profiles in 2-4 atmospheric layers from the ground to 30 km. The model of the ground-based FTIR

spectrometer is Bruker 120 M. The solar tracker which is needed for the atmospheric measurement is mounted on the roof of the container, with a hatch that can be remotely opened or closed. The measurements of CO, O_3 and CH_4 are used in this study.

COMCAL lidar system

The COMpact Cloud-Aerosol Lidar (COMCAL) system measures the backscatter Laser Light at 355 nm, 532 nm and 1064 nm and signal from the atmosphere. The aerosol and cloud information can be obtained from the measurements. The lidar is multi-channeled and with polarized design, which can help to determine the particle size and shape. In this study, the measurements of COMCAL are used to detect the cirrus cloud in the TTL over TWP.

COMCAL has been operating since April 2018 and continued measuring till May 2019. Due to technique issues, there are no measurements between May 2019 and March 2022. After maintenance, COMCAL started to be operated in March 2022 until December 2022. The details about the operation hours of the Comcal lidar system are given in Section B.2. In this work, measurements from April 2018 to August 2022 are used for analysis. In a total of about 332 h of lidar measurements that is useful for the analysis of the cirrus in 124 different days. Note that the lidar system is only available during the night, it is assumed that there is no dominant diurnal feature of the cirrus cloud over Palau following the study by Cairo et al., 2021.

ECC ozone and radio sondes

ECC ozone sondes and radiosonde launches have been conducted to measure the profile of O_3 and meteorological elements, such as temperature, air pressure, and relative humidity of the atmospheric environment since 2016. At least two ozone sondes are launched per week. Vaisala radiosondes were used for data transmission, measuring pressure, temperature, and humidity, and providing the GPS coordinates. The RS41-SGP (Sun et al., 2019) are used for both ECC ozonesondes and radio sounds after 2017. Before that, the old model, RS92-SGP (Dirksen et al., 2014) was used. The pressure and temperature profiles from the radio sounds are used to obtain air number density via the law of ideal gas (Bucholtz, 1995) and thus to calculate BSR (see section 3.3.2) combined with lidar measurement. On certain days when both the radiosonde and lidar measurements are available, this dataset was used for the case study analysis because of their high vertical resolution, see subsection 4.4.2.

Auxiliary Data: radio sounds by Palau weather station

The twice-daily radio sondes are conducted by the US National Weather Service (under NOAA, National Oceanic and Atmospheric Administration) in Palau weather station (station reference number: PTRO 91408). The location of PAO and Palau weather station are close to each other and on the same island of Palau. The temperature and potential temperature profiles measured by the Palau weather station are used to derive the level of the TTL (see section 2.2.2) over Palau and the meteorology properties of the cirrus cloud, for example, mid-cloud temperature.

3.2 The Fourier Transform Infrared (FTIR) Spectrometer

3.2.1 The principle of the FTIR spectrometer

The Fourier transform spectrometer (FTS) originated with A. Michelson's classic attempt to measure luminiferous aether in 1881. The aether was thought to be a medium that could permeate space and allow light to travel through interplanetary space at the time. This is probably the most well-known failed experiment in history (Blum and Lototsky, 2006).

The simple form of FTS is shown in Fig. 3.3a. which is similar to the instrument used in the Michelson experiment. A beamsplitter splits the light from the source into two beams, one reflected from the fixed mirror and one from the movable mirror, which introduces a time delay - the core of the FTS is a Michelson interferometer. The beams interfere, enabling the light's temporal coherence to be measured at each different time delay setting, effectively converting the time field into spatial coordinates. This brings an optical path difference (OPD) between the beam's two paths. The beam splitter is a plate composed of a partially reflecting and partially transmitting material, for example, Calcium Fluoride (CaF_2) and potassium bromide (KBr).

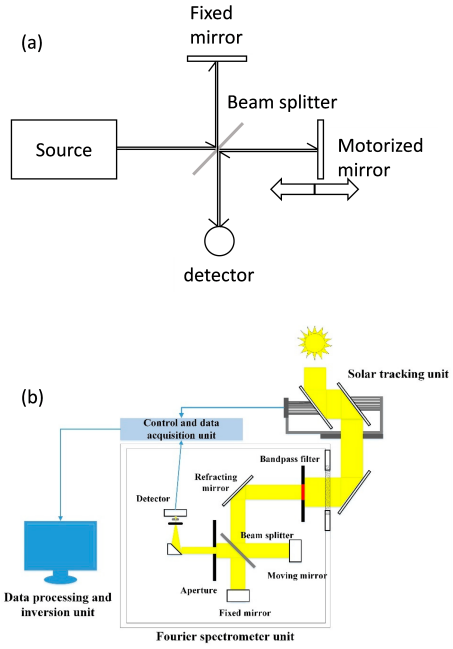

FIGURE 3.3: Schematic diagram of Fourier transform spectrometer. (a) A simple form of FTS. (b) The overall composition diagram of a high-resolution Fourier spectrometer (Shi et al., 2023, Figure 1).

The Ground-based solar absorption FTIR spectrometer uses the sun as the light source. It measures the solar spectrum in the infrared wave range. The gas molecules in the atmosphere absorb solar radiation at different frequencies of light. This can be used to derive the abundance, for instance, the total and partial column, of the trace gases in the atmosphere from the measured solar spectrum. Sunlight is directed into the instrument through a sun tracker and enters the optical chamber. It undergoes a series of reflections via mirrors, eventually entering the interferometer chamber. Inside the interferometer chamber, a beamsplitter divides the incoming

light into two perpendicular beams. One beam travels through the beamsplitter to reach the fixed mirror, while the other beam goes through the beamsplitter to reach the moving mirror.

The moving mirror chamber consists of multiple segments, and the total length of the moving arm can be up to 180 cm (for example, in the IFS 125HR model). A longer moving arm results in higher spectral resolution. Due to the movement of the moving mirror, there is a variation in optical path difference (OPD) between the two beams reflected by the moving and fixed mirrors. When these beams recombine, interference occurs, and the interfered light intensity signal is collected by a detector. The difference in the path length to fixed and moving mirrors creates OPD. The resolution of an FTIR spectrometer is related to the mirror travel or maximum OPD:

$$Resolution = 1/OPD \tag{3.1}$$

The interference signal generated at an OPD x by monochromatic radiation with wavelength $\lambda = 1/\nu$ (frequency) is defined as:

$$I(x)' = I(\nu)(1 + \cos(2\pi\nu x)) \tag{3.2}$$

When the incident radiation is a continuous spectrum, the detector receives an interference signal intensity:

$$I(x) = \int_0^\infty I(x)'dv = \int_0^\infty I(\nu)(1 + cos(2\pi\nu x))d\nu = I_{DC}(x) + I_{AC}(x) \tag{3.3}$$

Here, $I_{AC}(x) = \int_0^\infty I(\nu)(cos(2\pi\nu x))d\nu$ represents the harmonic term, varying with the OPD, while the constant term $I_{DC}(x) = \int_0^\infty I(\nu)d\nu$ is determined by the incident radiation intensity, and may be ignored because of the clear sky condition required while measuring.

The interference signal collected by ground-based Fourier spectrometers is a spatial domain function and does not represent the desired solar radiation spectrum intensity or spectral transmittance. Fourier transformation is necessary to obtain the transmittance spectrum. Equation 3.3 can be adjusted for the harmonic term as follows:

$$I_{AC}(x) = B(\nu)cos(2\pi\nu x) \tag{3.4}$$

Mathematically, Equation 3.4 corresponds to the cosine Fourier transform of the function $B(\nu)$. The spectral information is obtained by performing an inverse Fourier transform on the interference pattern, giving rise to the term "Fourier Transform Spectrometer (FTS)".

In theory, if the moving mirror could move an infinite distance, an interference spectrum can be captured spanning frequencies from 0 to infinity. However, real instruments have inherent systematic errors that require correction.

Firstly, the limited range of motion for the moving mirror necessitates convolution in the frequency domain using a truncation function, which is called the windowing or apodization. And one often used truncation function is Boxcar function:

$$D(\delta) = \begin{cases} 1, & \delta \leq |\Delta| \\ 0, & \delta > |\Delta| \end{cases} \tag{3.5}$$

Where Δ represents the maximum movement distance of the moving mirror. The corresponding spectrum is given by:

$$B(\nu) = \int_{-\infty}^{\infty} S(\delta)D(\delta)cos(2\pi\nu\delta)d\delta = B'(\nu) \otimes f(\nu) \tag{3.6}$$

Here, $B'(\nu)$ represents the spectrum obtained by Fourier-transforming the ideal interference spectrum at infinite OPD, and $f(\nu)$ is the frequency-domain representation of the function $D(\nu)$, known as the instrument line shape function.

3.2.2 Retrieval of the trace gases from the FTIR spectrometer

From the measurement of the solar spectrum from the FTIR spectrometer by the principle mentioned above in section 3.2.1, the next step is to retrieve the abundance of the trace gases in the atmosphere from the spectrum. This subsection introduces an overview of the widely used optimal estimation method (OEM) (Rodgers, 2000) for the retrieval of the column of atmospheric trace gases. The atmospheric radiation transfer equation can be abstracted as a simple mathematical equation:

$$y_i = F(X, b) \tag{3.7}$$

where y_i is the radiation signal which is the intensity or transmittance in the wavelength i, and X represents the unknown atmospheric and auxiliary parameters, i.e instrumental parameters, such as temperature profile etc., which are the quantities to be determined and that influence the radiation signal y_i. The term b represents the known atmospheric and surface state parameters. The function F encodes the radiative transfer process, also referred to as the forward process. The inversion process involves determining the unknown atmospheric and surface state parameters X, given the observed spectral data Y. Because observation instruments inevitably introduce errors ϵ, the observed spectrum can be expressed as:

$$Y = F(X, b) + \epsilon \tag{3.8}$$

The forward model is F, which describes the physics of the measurements. It represents the information of the light path through certain conditions of the atmosphere following the theory of the atmospheric radiative theory. Observational errors ϵ are

caused by various factors which can be changed with variations in observation conditions, making it impossible to obtain the exact values for each observation. Therefore, inverse problems require estimating the range of errors and searching for the optimal solution. According to Bayesian theory, when the observed spectrum Y is known, the probability density function (PDF) of X can be represented as:

$$PDF(X \mid Y) \approx \frac{P(Y \mid X)P(X)}{P(Y)} \tag{3.9}$$

In the equations provided:

- P(X) represents the probability of X under real conditions, indicating the distribution state of the target inversion quantity under actual circumstances, known as the prior (a priori) information.

- P(Y) represents the probability of Y occurring under real conditions. In real case, P(Y) is not accessible, there fore the equal sign in Equation 3.9 should be the approx equal sign.

- P(X | Y) represents the probability of X occurring when condition Y is known.

- P(Y | X) represents the probability of Y occurring when condition X is known.

The optimal estimation method suggests that when the observed spectrum Y is known, the X that maximizes the probability is the sought-after final solution for the inversion. This can be obtained by taking the derivative of P(X| Y) with respect to X to find the optimal solution X, as follow:

$$\frac{\partial P(X \mid Y)}{\partial X} = 0 \tag{3.10}$$

If we assume that the most general way to describe the distribution characteristics of a physical quantity in the natural world is the normal distribution, also called Gaussian distribution, then A can be represented as:

$$\begin{aligned} -2lnP(X \mid Y) = (Y - F(X))^T S_\epsilon^{-1}(Y - F(X)) \\ + (X - X_a)^T S_a^{-1}(X - X_a) + C \end{aligned} \tag{3.11}$$

where S_ϵ and S_a represent the observation and prior covariance, respectively, X_a represents the state variables, and C is a constant, the derivative equation 3.11 can be represented as:

$$\begin{aligned} \bigtriangledown_x [(Y - F(X))^T S_\epsilon^{-1}(Y - F(X)) \\ + (X - X_a)^T S_a^{-1}(X - X_a)] = 0 \end{aligned} \tag{3.12}$$

the term $[(Y - F(X))^T S_\epsilon^{-1}(Y - F(X)) + (X - X_a)^T S_a^{-1}(X - X_a)]$ is defined as cost function $J(X)$:

$$\begin{aligned} J(X) = [&(Y - F(X))^T S_\epsilon^{-1}(Y - F(X)) \\ &+ (X - X_a)^T S_a^{-1}(X - X_a)] \end{aligned} \tag{3.13}$$

The cost function can be understood as having two components: observational and prior information. Y represents the observational information, and S_ϵ is the covariance matrix of the observations. X_a represents prior information, and S_a is the prior covariance matrix.

Then the problem of inversion or retrieval is to find the minimum value of the cost function. If the function F varies continuously within a reasonable range, then there must exist a value, denoted as Δx, such that F is linear within the interval (x, x+Δx), which be represented as:

$$\Delta Y = \frac{\partial F(X, b)}{\partial x} \Delta x + \epsilon \tag{3.14}$$

where the partial term in Equation 3.14 $\frac{\partial F(X,b)}{\partial x}$ is the weighting function:

$$K_i^T = \frac{\partial F(X, b)}{\partial x} \Delta \tag{3.15}$$

But in real atmosphere, the fuction of the radiative transfer is nonlinear, so the Gauss-Newton method is commonly used to find the solution of the Equation 3.14 for slight non-linear cases. For more severe ones, the Levenberg-Marquardt method is commonly used. The iteration procedure which is used to find the maximum probability state $\hat{x}$ is shown as follows:

$$x_{i+1} = x_i + \hat{S}[K_i^T S_\epsilon^{-1}(y - F(x, b)) - S_a^{-1}[x - x_a]] \tag{3.16}$$

$$\hat{S} = [(1 + \gamma) S_a^{-1} + K_i^T S_\epsilon^{-1} K_i]^{-1} \tag{3.17}$$

where x_i represent the state x in the "i-th" iteration process, and K_i shows the sensitivity of the results to the state parameters. $\hat{S}$ is the covariance matrix of the solution, γ is the factor of the Levenberg-Marquardt method. The state vector or the maximum probability state after the final iteration converges is $\hat{x}$:

$$\hat{x} = x_a^{-1} + A(x_t - x_a) + \epsilon \tag{3.18}$$

$$\begin{aligned} A &= GK \\ &= [(1 + \gamma) S_a^{-1} + K^T S_\epsilon^{-1} K]^{-1} K^T S_\epsilon^{-1} K \end{aligned} \tag{3.19}$$

In equation 3.19:

- $\hat{x}$ is the retrieved state vector, and x_t represents the state of the atmosphere or environment.

- The contribution function matrix, denoted as G, represents how observed values contribute to the inversion results.

- The weighting function matrix, denoted as K, as mentioned above, describes how simulated values are sensitive to input parameters, such as instrument line shape functions, spectral parameters and atmospheric state.

- The Averaging Kernel Matrix (AVK), denoted as A, characterizes the sensitivity of inversion parameters to the true atmospheric state. It shows how changes in the inversion parameters impact the actual atmospheric condition.

In an ideal condition of the inversion problem, the matrix AVK would be an identity matrix I_n, indicating that the inversion results perfectly match the true values at all altitudes. However, in reality, the values of AVK may not equal to one, and their deviations indicate the extent to which the inversion relies on information from specific altitudes.

The trace of matrix AVK, often denoted as Degrees of Freedom (DOF) for signal, indicates the number of independent pieces of information used in the inversion process. In an ideal case, the trace of an $n \times n$ identity matrix (where n is the number of layers or altitudes) would equal to n, signifying that inversion is independent in each layer, and the retrieval results match the true atmospheric state. However, in practice, the retrieval results are influenced by both the true state and the initial values. In an ideal condition, the initial values do not impact the results. But in reality, the closer initial values lead to the closer inversion results to the true values.

There are several software packages, for example, GFIT (Wunch et al., 2010) and SFIT-4 algorithm, of this fitting method can be used for the ground based FTIR. GFIT is a well-established retrieval software, which has been widely used for TCCON networking. It scales the a priori profiles of the trace gases by a constant parameter which minimises the root mean square (RMS) value between the observational and the forward calculated spectrum. By this method, we can obtain the total column of the trace gases. Another way is used in SFIT-4. It modifies the profile of the mixing ratio of the trace gases in different layers by the OEM method described before. After the iterative process, the software can get the profiles of the trace gases in different layers. The SFIT-4 software package is commonly used in NDACC, which can be found in the website: Infrared Working Group Retrieval Code, SFIT.

Currently, there are two main high-resolution FTIR monitoring networks worldwide, namely the Total Carbon Column Observing Network (TCCON) and the Network for the Detection of Atmospheric Composition Change InfraRed Working Group (NDACC-IRWG), both shown in Figure 3.4. As shown in the figure, there are sufficient spatial coverage of both TCCON and NDACC sites in North America and Europe. But there is still a clear gap in oceanic regions, for example, the Western Pacific region. The equipment of FTIR in PAO can partly fill in this gap and shed light on the trace gas content in the TWP region.

Both TCCON and NDACC observation networks have their own advantages and disadvantages. TCCON stations typically use CaF_2 beamsplitter and InGaAs detectors, while NDACC stations typically use KBr beamsplitter along with MCT and

TABLE 3.1: Wave bands of spectroscope and detector adopted by TCCON and NDACC.

Beamsplitter	**Waveband**
CaF_2	14000-1850 cm^{-1}
KBr	4800-450 cm^{-1}
Detector	**Waveband**
InGaAs (Indium Gallium Arsenide)	12800-4000 cm^{-1}
InSb (Indium Antimonide)	9600-1850 cm^{-1}
	5000-780 cm^{-1}
MCT (Mercury Cadmium Telluride)	12000-600 cm^{-1}
	12000-420 cm^{-1}

InSb detectors. The wavelength information for these instruments is provided in Table 3.2. As shown in this Table, TCCON mainly concentrates on greenhouse gases, such as CO_2 and CH_4 in the near-infrared (NIR) and aims at a very high precision providing long-term monitoring data and is an ideal data source for verifying the results of relevant satellite remote sensing detection. And NDACC focuses on the measurements in the mid-infrared (MIR). Since the MIR includes more gas absorption peaks, it can measure more kinds of trace gases than NIR. For PAO, the measurements of trace gases are made and retrieved under the framework of NDACC observation networks.

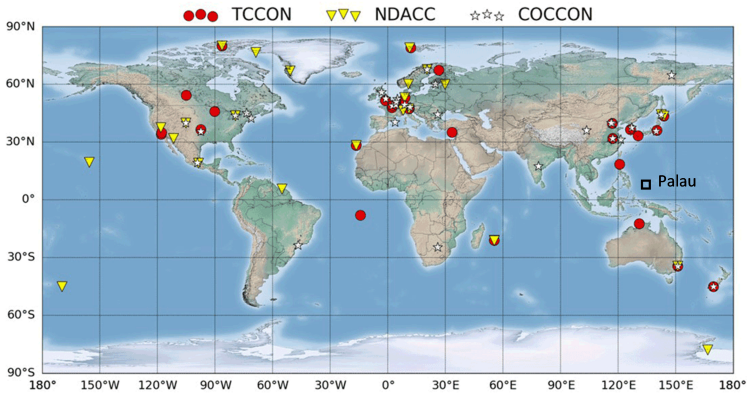

FIGURE 3.4: Global FTIR observation networks, including TCCON, NDACC-IRWG, and COCCON networks. This figure is adapted from (Sun et al. (2022), Figure 3). Palau is marked as the black square in the plot.

3.2.3 Measurements by FTIR spectrometer in Palau

The FTIR spectrometer in PAO (see Section 3.1) is installed in the container in Palau, equipped with a Sterling-cooled InSb detector, covering the spectral region between 1900 cm^{-1} and 6000 cm^{-1} since the beginning of the installation of the instrument.

However, the vibrations of the Sterling-cooled system lead to spikes in the spectra up to 2500 cm^{-1}. Thus, high-quality measurements are available above 2500 cm^{-1}.

In August 2022, the second detector, MCT, was installed to cover the spectra range between 700 cm^{-1} and 3000 cm^{-1}. Different from the InSb detector, the MCT detector needs to be cooled with liquid nitrogen which is available on the Palau island. The lower wavenumber region allows the study of the concentration profiles with higher precision, which gives especially importance to the O_3 since the isolated suitable O_3 absorption lines can be found around 1100 cm^{-1}, shown in Figure 3.5.

The retrieval of the profiles requires an optimum alignment of the instrument. The Instrumental Line Shape (ILS) must be close to the theoretical optimum line shape and well known. We aligned the whole instrument in 2022, using gas cells, filled with a gas of known pressure. Using the software LINEFIT allows us to retrieve the ILS to a sufficient degree Hase, Blumenstock, and Paton-Walsh, 1999. In an iterative procedure of aligning the instrument, and retrieving the ILS, the alignment results in an optimal Instrumental ILS.

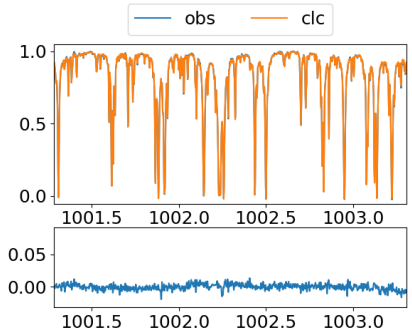

FIGURE 3.5: The example spectra of O_3 for the retrieval.

3.3 Technique of ground-based lidar measurement

Cloud and aerosol have a significant impact on the climate of the earth, which can interfere with the transfer of radiation through the atmosphere. LIDAR is an acronym that refers to Light Detection AnD Ranging. It is an active remote sensing instrument which emits laser pulses into the atmosphere for detection and measurement. The measurement by the COMpact Cloud and Aerosol LIDAR (COMCAL) is used in this study for the detection of the cloud and aerosol over Palau. This section will describe the theoretical basis of lidar remote sensing technology, and give a brief description of the lidar system. Besides, how to derive particle optical properties from lidar data and its related uncertainty are also described.

3.3.1 Elastic lidar equation

Most emitted photons undergo elastic scattering, meaning there is no change in wavelength between the scattered and emitted photons. In the following text, only elastic scattering lidar system are described. Below, the equation outlining the operational mechanism of elastic lidar systems (Eq. 2.1) is introduced.

$$P(\lambda, z) = C \cdot \frac{O(\lambda, z)}{z^2} \cdot \beta(\lambda, z) \cdot \exp(-2 \int_{z_0}^{z} \alpha(\lambda, \hat{z}) dz) \tag{3.20}$$

In the equations provided:

- z is the altitude. It should be noted that we only consider the ground-based lidar system, although the lidar has also been used and mounted in aircraft and satellites.

- β refers to the volumetric backscatter coefficient, with the units $\mathrm{m}^{-1}\mathrm{sr}^{-1}$. The backscatter coefficient describes the potential of an atmospheric layer to act as a mirror which reflects light backwards. It depends on the wavelength λ of the light.

- α refers to the volumetric extinction coefficient, with the units m^{-1}. It depicts how much energy is lost in a beam when it propagates through an atmosphere. The energy is lost either due to scattering σ or absorption a. Thus, $\alpha(\lambda, z) = \sigma(\lambda, z) + a(\lambda, z)$.

- O refers to the overlap fuction between the laser beam and the field of view (FOV) of the receiving telescope. The overlap function quantifies how many photons reach the detector compared to those at the telescope aperture. It starts at zero, increases with distance, and reaches unity when the laser beam fully enters the detector. z^2 accounts for signal intensity decrease with range, representing the lidar's dynamic range. The term $\frac{O(z,\lambda)}{z^2}$ refers to geometric factor of the lidar system, influenced by factors such as the relative alignment of emitter and receiver optical axes, laser beam diameter, divergence, telescope diameter, field of view (FOV), and aperture diameter (Sicard et al., 2020).

- C is the lidar constant, which is the summary of all technical quantities of the lidar:

$$C = P(z_0, \lambda) \cdot \frac{c \cdot \tau}{2} \cdot A \cdot T_{\lambda}^{emis} \cdot T_{\lambda}^{rec} \tag{3.21}$$

This lidar constant linearly depends on the number of emitted photons of the laser per pulse $P(z_0, \lambda)$ and the transmission efficiencies of the emission and recording optics T_{λ}^{emis} and T_{λ}^{rec}. The term $c \cdot \tau / 2$ represents the effective pulse length, indicating the portion of the volume from which back-scattered light is received. A represents the area of the receiving telescope.

By using this equation, it is important to emphasize that these lidar equations hold true when considering single-scattering processes, coherent light emission, and quasi-monochromatic characteristics. Besides, it is assumed that with the high resolution, a variability of the backscatter and extinction coefficient within the step of the altitude is negligible. Besides, the altitude resolution should be longer than the length of the laser pulse.

3.3.2 important definitions for lidar science

By solving the lidar equation, the primary quantities β and α of the lidar equation are derived. As introduced before in Section 3.3.1, both β and α have a contribution from the scattering part of the particle, denoted as β^{par} and α^{par}, respectively. The scatter of the gases is denoted as β^{Ray} and α^{Ray}, respectively. The gas scattering process

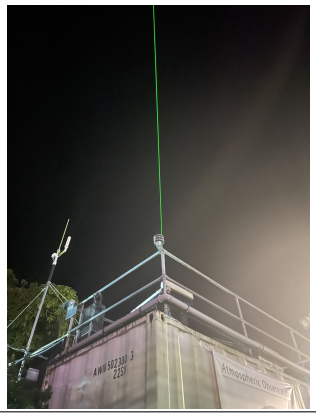

FIGURE 3.6: The picture of COMCAL when the light pulses are vertically emitting during the night.

happens in the clear atmosphere, widely known as Rayleigh scattering (Bucholtz, 1995). The contribution from the absorption to the extinction is denoted as α^{abs}.

When light is scattered or absorbed by one atmospheric constituent, it can no longer interact with other components. Therefore, the total backscatter and extinction are simply the sum of the contributions of the individual components:

$$\beta^{total} = \beta^{par} + \beta^{Ray} \tag{3.22}$$

$$\alpha^{total} = \alpha^{par} + \alpha^{Ray} + \alpha^{abs} \tag{3.23}$$

where α^{abs} represents the absorption part of the molecules influenced by trace gases, such as O_3 (Pope and Fry, 1997) and water vapour (Pope and Fry, 1997).

For multi-wavelength lidar, the Color Ratio (CR) $CR(\lambda_1, \lambda_2)$ is often used to quantify the ratio of the particle backscatter between two different wavelength:

$$CR(\lambda_1, \lambda_2) = \frac{\beta^{par}(\lambda_1)}{\beta^{par}(\lambda_2)}, \lambda_1 < \lambda_2 \tag{3.24}$$

in this definition, since two of the wavelengths should satisfy the relationship $\lambda_1 < \lambda_2$, so $CR(\lambda_1, \lambda_2) \geq 1$.
The size of particles detected by multi-wavelength lidar can be roughly determined by calculating the CR from the two wavelengths used by the lidar system, similar to the Ångström (Ångström, 1929) exponent, a rough estimate of the particle size. The simple relationship between particle size and CR is that the larger the particle size, the closer the CR approaches 1 (Ritter et al., 2016).

Including the COMCAL lidar system used in this study, commonly used lidar systems are equipped with polarized laser emission systems. The Linear DePolarization Ratio (LDPR) δ is defined as the ratio the particle backscatter coefficient β^{par} in polarization states perpendicular and parallel to the laser:

$$\delta = \frac{\beta^{par}(\lambda)_{\perp}}{\beta^{par}(\lambda)_{\parallel}} \tag{3.25}$$

According to the definition of the LPDR, with the particle becomes more spherical, the value of the LPDR decreases (Ritter et al., 2016).

Finally, the important definition of Backscatter Ratio (BSR) is defined as follows:

$$BSR(\lambda) = \frac{\beta^{total}(\lambda)}{\beta^{Ray}(\lambda)} = 1 + \frac{\beta^{par}(\lambda)}{\beta^{Ray}(\lambda)} \tag{3.26}$$

When particle scattering is negligible, that is, there is only Rayleigh scattering in the atmosphere, the value of BSR is approximately equal to 1. Therefore, BSR is used to calibrate lidar signals. In addition, it is a useful value for the detection of aerosols or clouds. This method is introduced in the later section 3.3.5.

3.3.3 Iterative Solution of Lidar Equation

As defined in section 3.20, the lidar equation can be rewritten as follows form:

$$P(\lambda, z)z^2 = S(\lambda, z) = C \cdot \beta(\lambda, z) \cdot \exp(-2\int_{z_0}^{z} \alpha(\lambda, \hat{z})d\hat{z}) \tag{3.27}$$

For this elastic lidar equation, there are two physically unknown terms, the backscatter coefficient β and extinction coefficient α. Collis (1966) introduced a slope method applied to a homogeneous and turbid atmosphere condition when $\alpha^{par} >> \alpha^{Ray}$. However, the condition is rare so this method can only applied in limited cases. In heterogeneous atmosphere conditions, when there are both aerosol and cloud layers and aerosol-free layers (Klett, 1981; Fernald, 1984), the Klett-Fernald approach can be applied. By this approach, the scatter contributed from both particle and molecular is considered. Usually, the relationship between β and extinction coefficient α needs to be assumed:

$$LR(\lambda, z) = \frac{\alpha^{par}(\lambda, z)}{\beta^{par}(\lambda, z)} \tag{3.28}$$

So the two terms can then be replaced by one physically unknown term, via this term Lidar Ratio (LR, in sr). Then the total extinction can be replaced by the sum of the scatter and the absorption part (eq. 3.23), thus the equation 3.27 can be rewritten as:

$$S(\lambda, z) \cdot \exp(-2\int_{z_0}^{z} (\alpha^{Ray} - LR\beta^{Ray})d\hat{z}) = C \cdot \beta(\lambda, z)(-2\int_{z_0}^{z} LR(\hat{z})\beta(\lambda, \hat{z})d\hat{z}) \tag{3.29}$$

The left side of the equation is known since the α^{Ray} and β^{Ray} from Rayleigh scattering can be calculated by air density profile from radiosonde (see section 3.1). So the equation becomes a non-linear differential equation of the second degree with one physically unknown term $\beta(\lambda, \hat{z})$, namely the total backscatter coefficient.

The steps of obtaining the numerically stable solution to derive the backscatter profile from the elastic lidar equation should refer to (Weitkamp, 2006). In this section, the steps are not discussed here for the sake of simplicity. Finally, the solution of the total backscatter coefficient $\beta(\lambda, z)$ is:

$$\beta(\lambda, z) = \frac{S(\lambda, z) \cdot \exp(-2 \int_z^{z_{cal}} (\alpha^{Ray} - LR\beta^{Ray}) d\hat{z})}{\frac{S(\lambda, z_{cal})}{\beta(\lambda, z_{cal})} + 2 \cdot \int_z^{z_{cal}} LR(\lambda, \check{z}) S(\lambda, \check{z}) \exp(-2 \int_{\check{z}}^{z_{cal}} (\alpha^{Ray} - LR\beta^{Ray}) d\hat{z}) d\check{z}} \tag{3.30}$$

where z_{cal} refers to the backscatter calibration range. Refer to Klett (1981), only stable solution can be found in the interactions performed from the far side of the lidar system, hence: $z << z_{cal}$. This final solution (3.30) is called the "Klett solution".

In summary, the solution of the lidar equation is based on the assumption of a lidar ratio LR and leads to a second-degree differential equation, which depends on the calibration of the backscatter as a boundary value. Hence, the uncertainty of the solution $\beta(\lambda, z)$ (backscatter profile) depends on:

- the error of the profile of the lidar signal;

- the chosen of the value of the LR;

- the backscatter calibration.

Errors are introduced due to the signal noise of the lidar system. The error can also introduced because of the air density profiles obtained from radiosonde. To avoid such errors to some extent, the selection of the data according to the background noise is conducted and the maximum errors of the backscatter profiles are also given in the products of the lidar system.

The assumption of LR in the particle layer poses a challenge in real-world scenarios where LR varies vertically due to factors like aerosol particle size, refractive index, and shape. For example, LR can range from approximately 20 sr in the lower troposphere with marine aerosols to 100 sr when combustion aerosol particles are present at higher altitudes (Burton et al., 2013; Giannakaki et al., 2007). The accuracy of the Klett–Fernald method decreases when optically thin clouds are present because their LR differs from that of aerosols, causing convergence issues in lidar solutions. To address this, an iterative LR selection method, developed by Nakoudi, Stachlewska, and Ritter (2021) is employed in this study.

When the iterative LR selection method is applied, backscatter calibration is required. The backscatter calibration range (z_{cal}) is typically placed at a high altitude in the atmosphere where particle scattering is negligible compared to Rayleigh scattering. In this study, z_{cal} was positioned in the lower stratosphere above Palau, typically between 25-28 km. A calibration value for the BSR (Eq. 3.26) needs to be assumed (commonly $BSR355_{cal} = 1.01$ and $BSR532_{cal} = 1.05$, but may adjust in specific cases when there is stratospheric aerosol in the calibration range). This value serves as a boundary condition for the lidar differential equation, which can be solved either

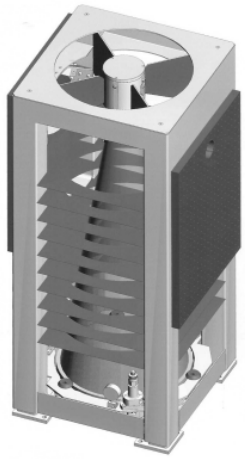

FIGURE 3.7: The outward appearance of the lidar telescope. From Immler et al. (2006), Fig. 1.

backward towards the lidar system or upward from the lidar system. The former solution is numerically stable (Fernald, 1984).

3.3.4 Design of the Lidar System COMCAL

The following part is based on the article by Immler et al. (2006) to briefly introduce the mechanical and optical design of the lidar system COMCAL.

The lidar system COMCAL was built for working in field campaigns on the ground or mobile platforms, for example, ships. It was also designed for automatic operation, allowing one to leave it without continuous maintenance, but only with regular attendance several times a year. The telescope of COMCAL is designed in Newtonian configuration with sending and receiving optics mounted to one rigid frame. As shown in Figure 3.7, The optical components are all held in one telescope frame to ensure the stability and limited set-up of the optical components.

The light pulses are vertically emitted by an Nd: YAG Laser (Quantel Brilliant) at three wavelengths, 1064 nm, 532 nm and 355 nm, the specification of the elastic detector channels are shown in Table3.2. A parabolic mirror collects the backscattered light from the atmosphere. The received light is then redirected by the flat secondary mirror in a breadboard that contains the detector optics (see Figure 3.8). A 90° off-axis parabolic mirror deflects the light by 90° while parallelizing it. A broadband dichroic mirror separates light wavelengths of 355 nm, 532 nm, and 1064 nm. While light at 1064 nm is detected directly by an Avalanche Photo Diode (APD), light at 532 nm and 355 nm is passed through a rotating Glan-Taylor prism that is synchronized with the laser. Thus, light polarised parallel and perpendicular to the polarisation of the laser is detected alternately. Because the same detection channel is used for both polar, this configuration enables depolarization measurement without the need for calibration.

The COMCAL lidar system is pointed vertically and operates during the local nighttime because of local legal regulations. It obtains backscattering profiles with a time

TABLE 3.2: Specifications of the detector channels

Channel (nm)	Pulse Energy (mJ)	max. Transmission	repetition rate (Hz)
1064	120	82%	
532	180	36%	20
355	65	52%	

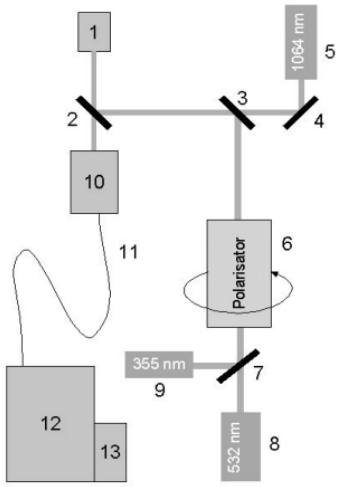

FIGURE 3.8: Schematic diagram of the detector optics: 1: 90° Off-Axis mirror, 2,3,4,7: dichroic mirrors, 5: Detector for 1064 nm Signal (Interference filter, lens, APD), 6: rotating Glan-Taylor prism, 8,9: Detectors for 532 nm and 355 nm signals (Interference Filters, Lens, PMT), 10: Fiber coupler, 11: fibre bundle, 12: Czerny-Turner Spectrograph, 13: Multi-Anode-PMT. From Immler et al. (2006), Fig. 1.

resolution of 135 s and an altitude resolution of 60 m. The vertical range of the profiles is in principle from the ground up to 25 km.

3.3.5 Detection of the cirrus cloud layer from lidar

As described in 3.3.1, the backscatter coefficient β can be obtained by solving the lidar equation by "Klett solution" (3.30). So the BSR as the ratio of the total and the molecular backscattering coefficient as defined by equation 3.26 can be also obtained. Thus, the cloud boundaries can be determined from the profile of the BSR measured by lidar, which is the signal peak of the BSR as a function of the altitude.

To determine the cirrus boundaries, the wavelet covariance transform (WCT) method is applied. The coefficient $W(a,b)$ is the result of the convolution between BSR and a zero-order wavelet function (Haar function). This function usually used to get the planet boundary layer (PBL), for example, Baars et al. (2008), is defined by the following equation:

$$h(\frac{z-b}{a}) = \begin{cases} +1, & b - \frac{a}{2} \leq z \leq b \\ -1, & b \leq z \leq b + \frac{a}{2} \\ 0, & elsewhere \end{cases} \tag{3.31}$$

where a and b are the width and the dilation of the wavelet, respectively. The coefficients $W(a,b)$, which are the convolution results between the $BSR(z)$ and $h(\frac{z-b}{a})$, are:

$$W(a,b) = \frac{1}{a}\int_{z-a/2}^{z+a/2} BSR(z)h(\frac{z-b}{a})dz \tag{3.32}$$

If BSR is in phase or anti-phase with the Haar wavelet, the convolution result shows a local maxima or minima of the $BSR(z)$ as a function of z. Thus, this can be used to determine the inflection point of the BSR, which, corresponds to the bottom or top of the cirrus cloud.

The parameter a is chosen to 500 m, and sensitivity studies show that the change of the value a between 300 m to 900 m does not show major effects on the determination of the cirrus cloud boundaries. The parameter b is the height step in the altitude range where the inflexion points of the BSR are. Thus, the range of the value b should be the altitude range where the signal of the cirrus cloud occurs. Above 10 km altitude, the cirrus clouds are known to be ice clouds, so we take 10 000 m as the minimum value of the parameter b, following a previous study by Cairo et al., 2021. The maximum value of b is 20 000 m which is chosen as the upper limit of the cirrus cloud.

Another important parameter is the threshold $W_{threshold}$ of the W. At which altitude the value of W exceeds this threshold, this certain altitude represents the bottom or top of the cirrus cloud. A dynamic method was applied to determine the threshold of WCT value which represent the base and top height of the cirrus cloud. It is calculated by:

$$W_{threshold}(top) = \max W - \frac{\max W}{10} \tag{3.33}$$

$$W_{threshold}(base) = \min W - \frac{\min W}{-10} \tag{3.34}$$

For cases with more than one cloud layer, we first use this method to obtain the first layer, and then remove the first layer. After that, we use the same method again to the WCT profile without the signal from the first layer until no cloud layer can be filter out.

Figure 3.9 and 3.10 give an example of this method in 6 December 2018. There are two distinct layers of cirrus as shown in Figure 3.9 by the enhancement of BSR from the clear sky background BSR equal to unity. In Figure 3.10, these two lower and higher layers detected by the WCT method are shown.

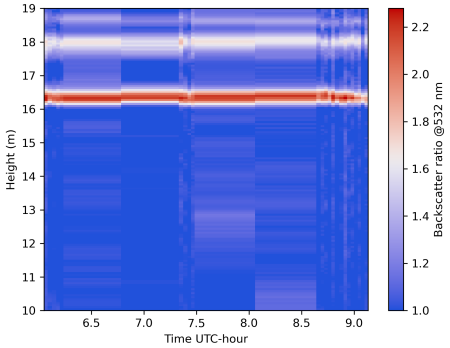

FIGURE 3.9: BSR at 532 nm as a function of time and height measured by lidar on 6 December 2018.
The dashed line shows the time in 8:00 UTC.

The cloud layer detection method we used is WCT, which is based on an integral quantity instead of the differentiation technique in vertical layers based on the direct analysis of a specific threshold of BSR. Since the signal-to-noise ratio (SNR) in the upper troposphere where the cirrus cloud layers occur is often subjected to low value (Nakoudi, Stachlewska, and Ritter, 2021; Dionisi et al., 2013), this WCT method we used to detect the cirrus cloud layer is better than the direct analysis of BSR and has been used for several studies of similar cloud layer detection, e.g. Nakoudi, Ritter, and Stachlewska, 2021; Pandit et al., 2014; Dionisi et al., 2013.

3.4 Models

3.4.1 GEOS-Chem

Overview of the GEOS-Chem model

The global 3-D chemical transport model GEOS-Chem in version 13.0.0 (Bey et al., 2001) are used, driven by meteorology input from the Goddard Earth Observing System (GEOS) of the National Aeronautics and Space Administration (NASA) Global Modeling and Assimilation Office. GEOSChem Classic uses the TPCORE advection algorithm (Lin and Rood, 1996) on the latitude-longitude grid of the archived meteorological data. The model can be driven by the Modern-Era Retrospective Analysis for Research and Applications, Version 2 (MERRA-2) reanalysis of meteorological fields produced by the Global Modeling and Assimilation Office (GMAO) at the Goddard Space Flight Center. The MERRA-2 reanalysis dataset for 1979 to present has the finest horizontal resolution of 0.5° latitude $\times$ 0.625° longitude and with 72 vertical levels (for native use) or 47 vertical levels (for reduced use). The coarsest horizontal resolution option in GEOS-Chem is 4° latitude $\times$ 5° longitude again with 72 or 47 vertical levels. The MERRA-2 reanalysis products are the recommended meteorology source for the classic GEOS-Chem model. It can be conducted using OpenMP shared-memory paralleling. This model is called the GEOS-Chem Classic (GCC) model. Another multi-node variant of GEOS-Chem is the GEOS-Chem High Performance (GCHP) which aims for paralleling running in the mainframe. It is

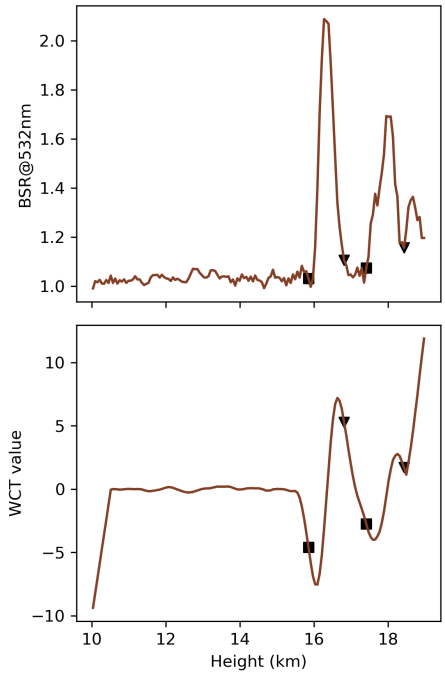

FIGURE 3.10: An example case for the WCT method: (a) BSR at 532 nm and (b) WCT value as a function of height in 8:00 UTC. The squares show the height of the cloud base and the triangles show the height of the cloud top detected by the WCT method.

conducted with MPI distributed-memory parallelization across multiple nodes. The meteorology data in GCHP is the operational GEOS-Forward Processing (GEOS-FP)product, which has the finest horizontal resolution of 0.25° latitude × 0.3125° longitude for 2012 to present. The GEOS-FP reanalysis data products are another optional meteorology input for the classic GEOS-Chem but with limited time coverage.

The grids used in those two models are different. The classic GEOS-Chem model runs in the classic rectilinear grid. But for GCHP, it runs on a specific cubed-sphere grid, which benefits the study in the polar region. For this study, since the focus on the tropics, and the requirement for high-speed running is not so urgent, the GCC model is sufficient. For a simulation in a specific region, the GCC model can be conducted in the nested mode. It requires the GCC model first conducted in the native grid in a coarse resolution to save out the boundary conditions, for example, 4° latitude × 5° longitude globally. Then the model is conducted in a user-specified region with a horizontal resolution of 0.5° latitude x 0.625° longitude in the nested mode. The boundary conditions as an input of the nested simulation are provided by the global simulation conducted before, see Figure 3.11.

GEOS-Chem uses the stand-alone chemical module that performs chemistry, aerosol physics, radiation, emissions, and deposition on 1-D atmospheric columns. In particular, for emissions, the stand-alone software component for computing emissions in global atmospheric models, Harvard–NASA Emission Component (HEMCO) (Keller et al., 2014a) is a software component which is combined with GEOS-Chem. It is used for computing atmospheric emissions from different sources, regions, and species on a user-defined grid. The emission of different species, such as trace gases,

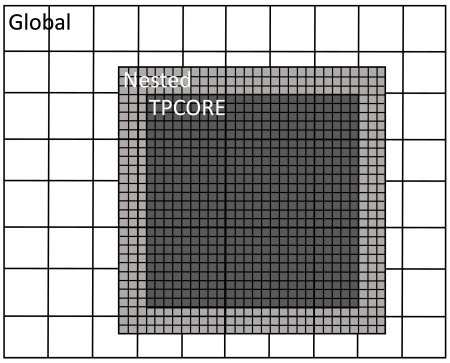

FIGURE 3.11: Schematic diagram of the nested simulation. The outermost box (Global) is the region of the global simulation, with a coarse resolution of 2° × 2.5° or 4° × 5°, which provide boundary conditions for the nested simulation. The next innermost box (Nested) is the region of the nested simulation, with a fine resolution, for example, 0.5° × 0.625°. The innermost box (TPCORE) is the actual box in which the TPCORE advection (Lin and Rood, 1996) algorithm performs. The region between Nested and TPCORE box is the so-called "buffer zone", in which the tracer concentration is overwritten by the 2° × 2.5° or 4° × 5° boundary conditions at the simulation time. The buffer zone is typically 3 grid boxes along each boundary, and this set-up is also used in this study.

different aerosol components, and transport tracers with specified ages, can be defined and controlled by the user through the HEMCO configuration file. It is used to combine, overlay, and update a set of inventories as the user specifies. In addition, HEMCO can be conducted in standalone mode or coupled with other atmospheric models such as the Weather Research and Forecasting (WRF), the NASA GEOS Earth System Model (GEOS ESM) and the Community Earth System Model Version 2 (CESM2) with different usage and grid (Lin et al., 2021; Keller et al., 2014b).

GEOS-Chem model set-up

The basic setup of our model simulation is summarized in Table 3.3. I first used a coarse global simulation with a grid resolution of 2 ° × 2.5° to determine the boundary conditions. Then, I performed nested simulations with the resolution of 0.5° × 0.625° in the tropical zonal domain of 30°N to 30°S. The model runs used 72 vertical layers from the surface up to 10 hPa, and the output was saved for every day.

For the analysis of the passive tracer, the chemistry is switched off in the HEMCO emission configuration file. The emission of the passive trace was manually set as $1 \times 10^{-7}\,\mathrm{kg\,m^{-2}\,s^{-1}}$ in specified domains, which means the emission of the passive tracer is uniformly and constantly emitting in certain regions. The uniform flux within the specified domains was chosen to eliminate the regional dependency on emissions. After the release and the spin-up time, the distribution of the tracer is the result solely of air mass transport and atmospheric circulation.

For the comparison of the non-emission tracer, the simulation of the Sulfur hexafluoride (SF_6) was also conducted. I performed the simulation of SF_6 for the same time period of the passive tracer and with the same resolution of 2° × 2.5° and vertical grid resolution of 72 levels. The emission database of SF_6 is annually gridded

TABLE 3.3: The settings of GEOS-Chem v13.0.0 used in this study

Species	Passice Tracer	SF6
Resolution	$2^\circ \times 2^\circ$ (Global simulation) $0.5^\circ \times 0.5^\circ$ (Nested simulation)	
Meteorology field	Merra-2	
Transport / Convection timestep	600 s	
Emission inventroy	$1 \times 10^{-7}\,\mathrm{kg\,m^{-2}\,s^{-1}}$	EDGAR v4.2

data available at $0.1^\circ \times 0.1^\circ$ global resolution for 1970 - 2008 and taken from the Emission Database for Global Atmospheric Research (EDGAR version 4.2) inventory (Muntean et al., 2018).

For details about the experiment design of the model simulation, please see Section 4.1.1.

3.4.2 Trajectory model: HYSPLIT

To investigate the history and future of cirrus-cloudy air masses in the air measured over Palau, I use Air Resources Laboratory's (ARL) Hybrid Single-Particle Lagrangian Integrated Trajectory model (HYSPLIT) (Stein et al., 2015; Draxler and Hess, 1998) to conduct trajectory analysis. In the trajectory analysis, an air mass is assumed to be a small volume of air with uniform characteristics represented by meteorological parameters, such as temperature, pressure and wind vector. The HYSPLIT model outputs air mass paths projected forwards or backwards in time (trajectories) and is a commonly used method in various scientific contexts, specifically in atmospheric sciences.

HYSPLIT is a complete system for computing air parcel trajectories driven by user-specified meteorological data: 3-D wind fields, temperatures and several other variables on a regular grid at multiple levels and periods. The meteorological data are prepared in a format that HYSPLIT can directly read. In this study, meteorological data were selected from the operational system Global Data Assimilation System (GDAS, Kanamitsu, 1989) ($1^\circ \times 1^\circ$, 3-h temperal resolution, archive in HYSPLIT begin 1, December 2004) from The National Weather Service's National Centers for Environmental Prediction (NCEP). GDAS/NCEP is commonly used for air transport simulation by HYSPLIT(Stein et al., 2015).

HYSPLIT is based on a hybrid calculation method between the Lagrangian and Eulerian methodology. The Lagrangian approach uses a moving coordinate system of reference for the advection and diffusion calculations such as the forward and backward trajectories, which was used in this study. It can also combined with the Eulerian methodology, which uses a fixed 3-D grid as a coordinate system of reference to compute pollutant air concentrations.

In this study, the HYSPLIT model is used to calculate the backward and forward trajectories of the cirrus-cloudy air masses. 30-day backward and forward trajectories were released from the position of the cirrus cloud. The releasing points are calculated from the cloud top and base height with corresponding measurement time from the lidar measurement (see Section 3.3.5). The cirrus clouds are vertically divided into four layers with five heights as the starting points of the trajectories. The time step of the starting point of the cirrus cloud layer is selected as 1 h, based on

the assumption that within 1 h, the variation of the cirrus cloud can be neglected. This assumption is adapted from Cairo et al. (2021), which used a more coarse time gap with 3 h in the trajectory analysis of the cirrus cloud above Palau using a similar gound-based lidar system.

Chapter 4

Results

The Tropical Western Pacific (TWP) plays an important role in global stratosphere-troposphere exchange (STE) and is an active region of Inter-Hemispheric Transport (IHT). Common indicators for transport between the hemispheres like the tropical rain belt are too broad or lack precision in the TWP. In this chapter, we provide a method to determine the atmospheric chemical equator (CE) (Sun et al., 2023), which is a boundary for air mass transport between the two hemispheres in the tropics (Section 4.1). This method used the model output from an artificial passive tracer simulated by the chemical transport model GEOS-Chem in the troposphere. The movement of the CE is investigated in the tropics, which indicates the migration of atmospheric circulation systems and air mass origins. The airmass origins of the trace gases in the TWP region can be characterised by the simulation results of CE (Section 4.2) in TWP where the region is thought to be an essential pathway of STE (Fueglistaler, Wernli, and Peter, 2004; Rex et al., 2014). Thus, the component and the source of the troposphere trace gases in TWP play an important part in the atmospheric composition of the stratosphere. The STE is indicated by the cloud measurement in the UTLS by a ground-based lidar system. To evaluate the STE transport above the TWP region, measurements and analysis of cirrus cloud are presented by the polarization lidar, COMCAL, from 2018 to 2022 over Palau (Section 4.3). The aim is to analyse the cirrus geometrical and optical properties at the TWP region from observations derived with the ground-based lidar system, which fills the gap concerning the coverage of existing ground-based lidar studies in this region. To further investigate the STE transport over this region, HYSPLIT trajectory model simulation is used (Section 4.4). Combined with the trajectories and the cirrus cloud measurement, the mechanism and pathway of STE above the TWP region are investigated.

4.1 Chemical Equator (CE) by model simulation

The following part (Section 4.1) is based on the publications by Sun et al. (2023), which is the publication of this thesis's author. We aim to provide a tool to determine the boundary for air mass transport between the two meteorological hemispheres in the tropics, focusing on the TWP region. This tool can further determine the air mass origin in the TWP boundary layer. Here, we present model simulations of

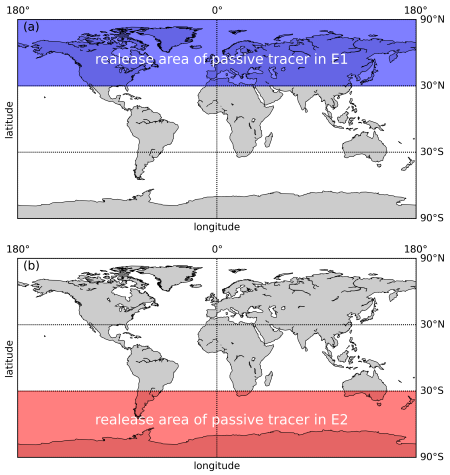

FIGURE 4.1: The releasing area of passive tracer E1 (shown by shaded blue region in the upper plot) and E2 (shown by shaded red region in the lower plot).

a passive tracer to determine this boundary. Following Hamilton et al. (2008), we use the term CE to describe this boundary. This way, we avoid confusion with the tropical rain belt indicated by the conventional ITCZ definition. To assess regional differences only caused by air mass transport, we switched off the chemistry in the model to develop an atmospheric pattern only due to the transport by the analyzed wind fields. This way, we neglect chemical processes and regional dependency of the emissions occurring for real species like CO and SF_6.

4.1.1 Determination of CE

Description of Different Experiments

A series of tracer experiments were made to investigate the CE. As shown in Table. 4.1, two base experiments, Experiment 1 (E1) and Experiment 2 (E2), are carried out to study the air mass transport from both hemispheres by releasing the tracer either in the northern or southern extra-tropics latitude bands (see Figure 4.1). The simulation time of E1 and E2 is from 2014 to 2019 and we take the simulation in 2014 as a spin-up simulation. The tracer experiments follow the same format: the inert chemical tracers with infinite lifetime were released into the atmosphere with the constant flux of $1 \times 10^{-7}\,\mathrm{kg\,m^{-2}\,s^{-1}}$ from the start to the end during each simulation. Similar to the actual vertical extent of the emission of the atmospheric component, the vertical extent of the emission of the passive tracer is from the surface to 1 km. The source domains of the passive tracer are marked by red and blue colors which means the passive tracer released from 30°N - 90°N and 30°S - 90°S, for different hemispheres, respectively.

Apart from these two base experiments, there are other experiments Experiment 3 (E3) - Experiment 5 (E5) designed to investigate the method's stability and ensure that it is robust in different model settings. These experiments and the results are described in more detail in the AppendixA.1. Because of the rapid mixing in the

TABLE 4.1: The settings of two base experiments

Experiment	Release area	Release layer	Simulated time
E1 (NH)	30°N - 90°N, zonally	Surface - 1 km	years (2014 - 2019)
E2 (SH)	30°S - 90°S, zonally		

troposphere, releasing tracers on different altitude ranges does not affect the method. For example, the uniform release of the tracer between the surface and 10 km only affects the spin-up time of each experimental case, not the distribution of the tracer on the ground. This method can also be used to determine the location of CE in other years of interest like E5 (simulating from 2010 to 2015), which differs from the simulation starting time of E1 - E4, indicating good repeatability of this method.

The uniform flux in the zonal range within the extra-tropics was chosen to eliminate the regional dependency on emissions. After release, the tracer first accumulated in the according hemisphere of release and then travelled to the other hemisphere, resulting in a stable north-south gradient pattern as a result of air mass transport and atmospheric circulation. For the sake of simplicity and clarity, the methodology of determining the CE introduced after is described based on E1. In the base experiment E1, the tracer was released in the NH extra-tropics to determine the northern boundary of the CE, which is abbreviated as CE-NH. The setup of the E2 was the same as that of the E1, except that the passive tracer emission region was placed in the SH. With the same method but applied to the simulation results from the E2, we can obtain the southern boundary of the CE called CE-SH.

Figure 4.2a shows a time series of the global distribution of the tracer averaged zonally in six latitude bands for the releasing of the tracer from 30°N - 90°N. After approximately one year of simulation, the linear growth rate is roughly equal in each latitude band. The meridional gradient of the passive tracer is similar to SF_6 shown in Figure 4.2b, supporting the use of a passive tracer for the study of IHT.

Decomposition method

To distinguish air mass transport from either one or the other hemisphere, the decomposition method is applied to the time series of the tracer, thus deriving the trend and the seasonality. An additive model of the decomposition is used:

$$y_t = T_t + S_t + R_t, \tag{4.1}$$

where y_t is the time series of the tracer, T_t is the trend component, S_t is the seasonal component, R_t is the residual component or noise. The subscript t denotes the time.

Figure 4.3 shows the decomposition of the time series of the passive tracer released from 30°N - 90°N. Two grid boxes in the TWP are shown here as examples, one located at 6.0°S, 127.5°E and the other located at 6.0°N, 127.5°E. The trend component in each grid box is a linear increase. The seasonal component of the grid box in the NH (as shown in Figure 4.3a) varied from positive values to negative values year-round, which shows the higher concentration from the higher latitude bands and lower concentration from the lower latitude bands. For the grid box in the SH

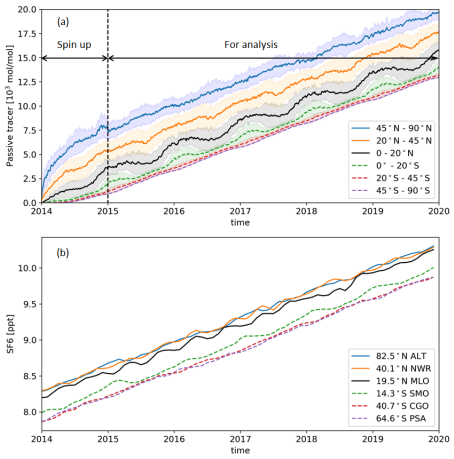

FIGURE 4.2: Comparison of the passive tracer and SF_6. (a) Zonally averaged amount of the passive tracer from GEOS-Chem simulations from 2014 - 2019 as a function of time for three northern (solid lines) and three southern (dashed lines) latitude ranges (0° - 20°, 20° - 45°, 45° - 90°). The value of the concentration of the passive tracer is not meaningful to the studies since we only take into account the relative higher or lower amount of the tracer. 1-σ of the passive tracer of each latitude band is shown in shaded color. (b) SF_6 monthly means from Combined SF_6 data from the NOAA/ESRL Global Monitoring Division at six stations corresponding to the latitude bands in Figure 4.2a (ALT: Alert (82.5°N, 62.3°W), NWR: Niwot Ridge (40.1°N, 105.6°W), MLO: Mauna Loa (19.5°N, 155.6°W), SMO: Cape Matatula (14.3°S, 170.6°W), CGO: Cape Grim (40.7°S, 144.8°E), PSA: Palmer Station (64.6°S, 64.0°W)).

(shown in Figure 4.3b), the seasonal component is positive only when a high concentration of the passive tracer is transported from the NH to this grid box. Otherwise, in other periods, approximately from March to November each year, the air mass from the south has a concentration value of zero, so the seasonal component is also around zero value.

After the decomposition, the trend of the tracer in each grid box can be given as $T_{t,i,j}$, where the subscript t, i, j refer to the time, the longitude and the latitude of the grid box, respectively. The trend in each grid box and each time step are spatially averaged in the domain of -180°S to 180°and 30°S to 30°N:

$$\overline{T_t} = \overline{T_{t,i,j}},\ i \text{ from } -180^\circ \text{ to } 180^\circ,\ j \text{ from } 30^\circ \text{ S to } 30^\circ \text{ N}, \tag{4.2}$$

where $\overline{T_t}$ is the spatial average of the trend which is also the criterion of the CE at each time step t.
The location of the CE in each time step t is given by $\overline{T_t}$, which is the spatial average at each time step of the trend, which indicates the tracer concentration on the CE:

$$CE_t = \left\{\text{where} : C_{i,j,t} = \overline{T_t}\right\}, \tag{4.3}$$

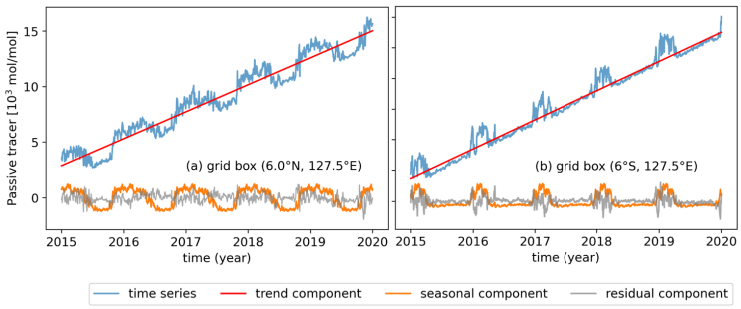

FIGURE 4.3: Time series of the passive tracer (blue line), trend component (red line), seasonal component (orange line), and residual component (grey line) of the passive tracer as a function of time (2015 - 2019) in two example grid boxes (a) [6.0°N, 127.5°E] and (b) [6.0°S, 127.5°E].

where $C_{i,j,t}$ is the tracer concentration in each grid box and each time step t . For example, if the concentration of the tracer (released from 30°N - 90°N) in a grid box is higher than $\overline{T_t}$, this grid box is located on the NH, and vice versa for the SH.

The CE-NH and CE-SH calculated by the decomposition method and the global distributions of the passive tracer averaged in January at each year of the simulation time from 2015 to 2019 are shown in the Figure 4.4. The concentration of the passive tracer gradually increases after the releasing time in both experiment cases. This latitudinal gradient can be clearly seen in the distribution of the passive tracer and is well determined by the CE-NH and CE-SH. There is another common used method to determine the CE or ITCZ from the gradient of the tracer. The comparison of our decomposition method and the gradient method is given in Appendix A.2, and it shows a less robust results by the gradient compared to the decomposition method.

By comparing the results of the two base experiments E1 and E2, we obtain insights into IHT and answer an important question of whether the northern and southern boundaries of the CE coincide with each other when the passive tracer was released in different latitude bands coming from two different hemispheres. The region between these two boundary lines is where interhemispheric mixing happens and is referred to as the CE.

4.1.2 CE and inter-hemispheric exchange

Figure 4.5 shows the daily locations of the CE-NH and the CE-SH by colored scatters. Here, we only present the CE in 2015 as an example. For other years (2016 - 2019) similar distributions of the CE are not given, because of the simplicity. Both CE-NH and CE-SH reach the southernmost position at the end of NH winter and the northernmost position at around 25°N at the end of NH summer, but do not coincide with each other (see Figure 4.5a and Figure 4.5b). In general, the daily CE-SH is further south than the CE-NH. In February, the CE-SH reaches around the southernmost position at 20°S in East Africa, the Indian Ocean, the Central Pacific, and South America. In late August, except for Africa and the Atlantic, the CE-NH reaches its northernmost position at about 20°N.

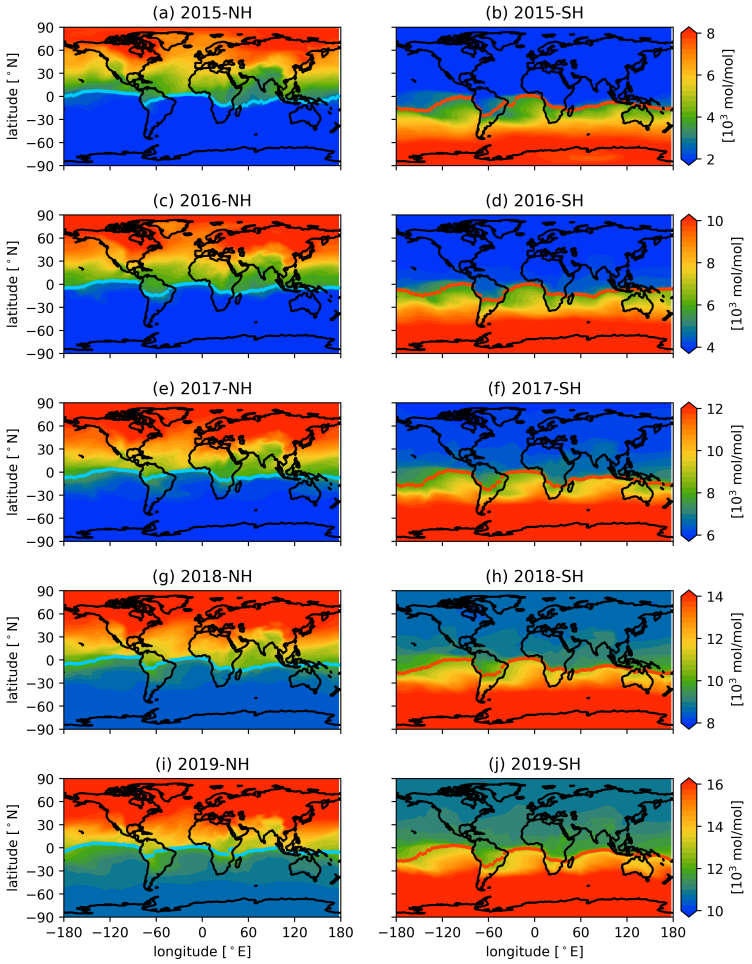

FIGURE 4.4: The surface concentration (mol/mol) of the passive tracer averaged in January at each year of the simulation from 2015 to 2019. The subplots in the left column (a), (c), (e), (g), (i) show the passive tracer released from the NH in Experiment 1 and subplots in the right column (b), (d), (f), (h), (j) show the passive tracer released from the SH in Experiment 2. The blue lines and the red lines show the CE-NH and CE-SH respectively.

The seasonal average of the CE from 2015 to 2019 is shown in Figure 4.6. Here, the CE clearly shows as a belt of meridional extent around the tropics between the northern and the southern boundaries of CE-NH and CE-SH. Since atmospheric transport is a continuous process, we don't expect a single boundary line separating the atmosphere and matter in the NH and SH. The boundary is a belt of longitudinal width in which air masses from the NH exchange and mix with those from the SH. As shown in Figure 4.6a, from December to February, the CE is located south of the equator. After that, the CE moves north from March to August (shown in Figure 4.6b and Figure 4.6c), crossing the equator to reach the geographical NH. In the NH spring and summer, the progressive domination north of the equator by the air mass originating from the SH is characterized by the movement of the CE. In the NH autumn (Figure 4.6d) and winter season (Figure 4.6a) the air flows from the NH gradually strengthen and the boundary moves southward, finally reaching its southernmost position in NH winter (Figure 4.6a). This suggests that the CE lags behind the ground position

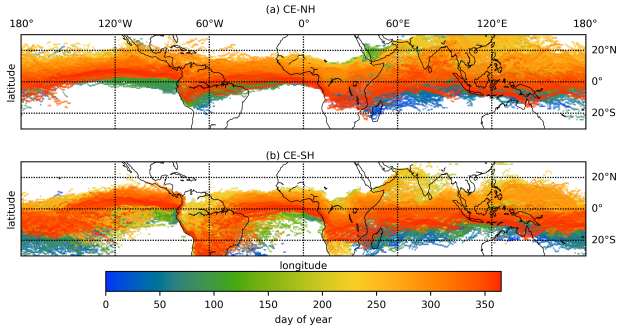

FIGURE 4.5: Daily CE-NH and CE-SH calculated from model simulations of (a) E1 (tracer released in NH) and (b) E2 (tracer released in SH) in 2015; the color shows the day of the year.

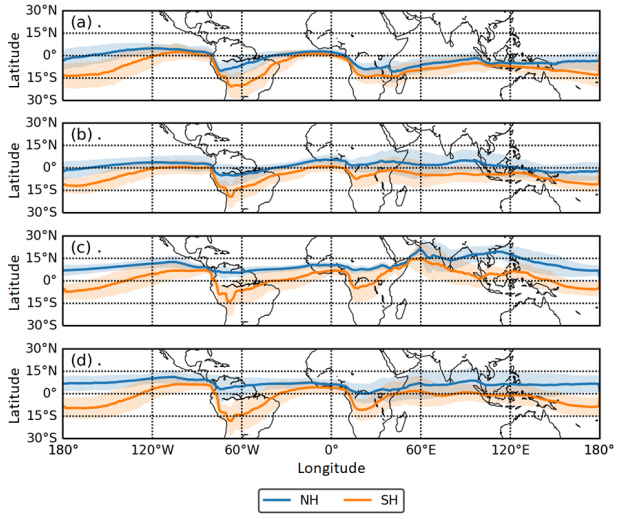

FIGURE 4.6: 5-year (2015 - 2019) averaged seasonal location of CE. (a) December, January, and February. (b) March, April, and May. (c) June, July, and August. (d) September, October, and November. 1-σ of the CE-NH and CE-SH of each season is shown in shaded color.

of the sun by about 3 months and coincides with the time lag of the ITCZ.

To further study the migration of the atmospheric boundary between the two hemispheres and its correlation to atmospheric circulation, we compare the circulation patterns over different regions. Figure 4.8 shows the annual movement of the CE and zonally-averaged 10-m wind vectors in different regions defined as rectangular boxes within the tropical band between 30°S and 30°N (see Figure 4.7): Central & Eastern Pacific (CEP): 180°- 80°W; South America (SA): 80°W - 40°W; Atlantic (AT): 40°W - 15°W; Africa (AF): 15°W - 50°E; Indian Ocean (IO): 50°E - 100°W; Tropical Western Pacific (TWP): 100°E - 180°. The division of the regions is adapted from the definition of tropical regions by Fueglistaler, Wernli, and Peter (2004). In general, the wind convergence zone is not always consistent with the latitude of the CE and follows a similar pattern: it is located south of the equator in winter and north in summer. However there are regional differences as described in the following. In the Central & Eastern Pacific and the Atlantic Ocean, the wind convergence zone

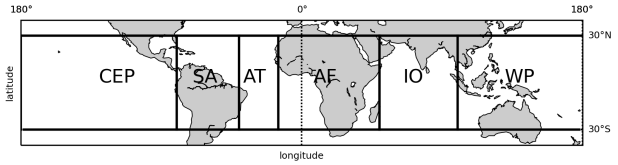

FIGURE 4.7: Definition of geographic regions in this study. Central & East Pacific (CEP): (180°, 80°W); South America (SA): (80°W, 40°W); Atlantic (AT): (40°W, 15°W); Africa (AF): (15°W, 50°E); Indian Ocean (IO): (50°E, 100°E); Tropical West Pacific (TWP): (100°E, 180°); all these regions are with the same latitude range: 30°S - 30°N.

agrees with the CE as shown in Figure 4.8 (CEP) and Figure 4.8 (AT). Here, throughout the year, north-easterly and south-westerly winds meet near the equator from 0° to 10°N, forming a clear convergence zone, while the CE lies in the confluence bands of the winds. The annual movement of the CE is relatively small in the Atlantic and Eastern Pacific, between 5°S and 10°N, indicating weaker seasonal shifts of the tropical circulation in those regions.

The seasonal movement of the CE is larger over the land sectors, i.e. tropical South America and Africa, and wind convergence zone and CE do not coincide, as shown in Figure 4.8 (AF) and Figure 4.8 (SA). In Africa, the confluence zone of north-easterly and south-westerly winds lies north of the CE. This implies that air masses from the NH are transported further south than the location of the wind convergence zone suggests. For South America, we cannot see a pronounced wind field convergence zone in Figure 4.8 (SA). The contrast between the north-easterly winds from the NH and the South-easterly winds from the SH is obvious, possibly due to the distribution of land and sea. In NH winter, from December to February, the CE-SH reaches its overall southernmost position at 15°S in South America.

In summary, the circulation system in the TWP and its interaction with the large-scale atmospheric circulation such as WPM and Hadley cell bring much complexity to the studies in this region. Over the TWP and the Indian Ocean, the annual movement of the CE is larger than over other ocean sectors, such as the Atlantic Ocean and Central & Eastern Pacific. From December to April, north-easterly winds deflect west after crossing the equator and converge with south-easterly winds from the SH between about 0° and 5°S. From May to November, this convergence zone moves northward, while the south-easterly winds turn west after crossing the equator and converge with north-easterly winds north of the equator.

4.1.3 Vertical structure of CE

An advantage of our method of determining hemispheric boundaries is that it allows analysis of the vertical structure of the IHT. The CE are calcuated for each vertical level of the model output. As Figure 4.9 reveals, the CE-NH and CE-SH show less meridional variation at lower levels than at higher ones. In Figure 4.9 we only present the vertical structure of the CE in the TWP (100°E - 180°, 30°S - 30°N, see Figure 4.7).

In general, the vertical sections of the hemispheric boundary of the atmosphere differ with seasons. From January to March, the CE tends to tilt north. During these three

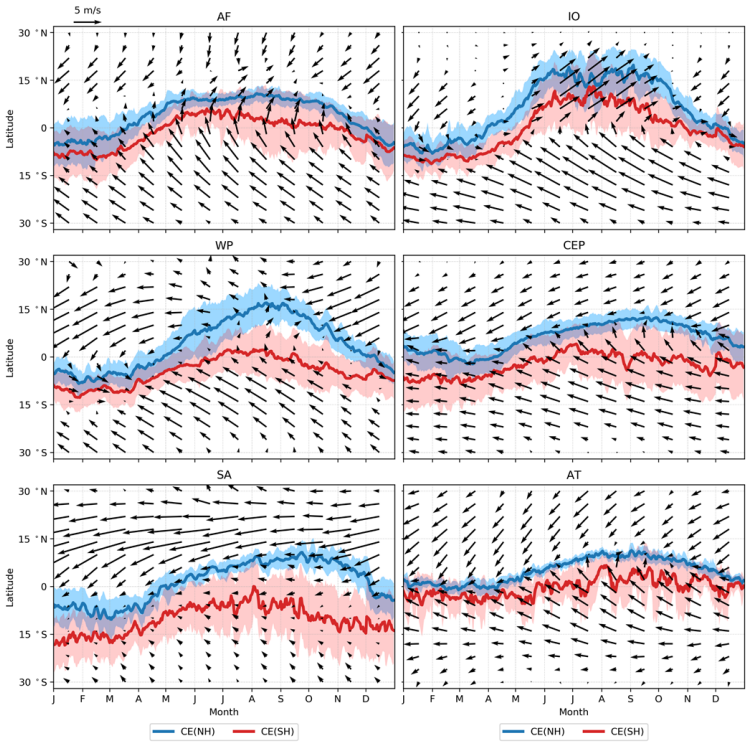

FIGURE 4.8: Monthly averaged 10-m wind vectors (black arrows) and annual movement of the daily CE. The blue lines show the NH boundary and the red lines show the SH boundary. The wind data are the 10-m winds from the ERA5 reanalysis data (Hersbach et al., 2020) averaged from 2015 to 2019. Both the CE and the wind field are space averaged zonally in eight different regions such as Africa (AF) and IO (Indian Ocean). The abbreviations and definition of the region on the top of each subplot are according to Figure 4.7. 1-σ of the CE-NH and CE-SH is shown in shaded color.

months, air masses from the NH below 2 km move south of the geographic equator to about 10°S, while air masses above 2 km south of the geographic equator originate in the SH. In April and May, the oblique structure becomes less pronounced and the CE begins to be vertical to the ground. From June to October, the CE tilts south. It should be noted that the CE-NH slopes southward from the ground up, while the CE-SH is relatively uniform from the ground to 2 km but tilts south in the upper altitude. This indicates that the airmasses originating in the SH near the ground do not move further north in the summer, but stay near the equator, forming a broader meridional mixing region in the boundary layer. In November, the CE-NH is the most uniform with altitude throughout the year and the overall CE is a more narrow band compared to other months. In December, the CE shows a slight sloping trend to the north. These two months, November and December resemble April and May with the most narrow and vertically uniform CE above 2 km throughout the year. They mark the turning points of IHT above 2 km altitude between a more northern and more southern position. In the discussion of the IHT we only take the model level under 8 km into consideration. With increasing altitude, the boundary between the two hemispheres is less pronounced due to the fast horizontal mixing by high-speed winds in the upper troposphere.

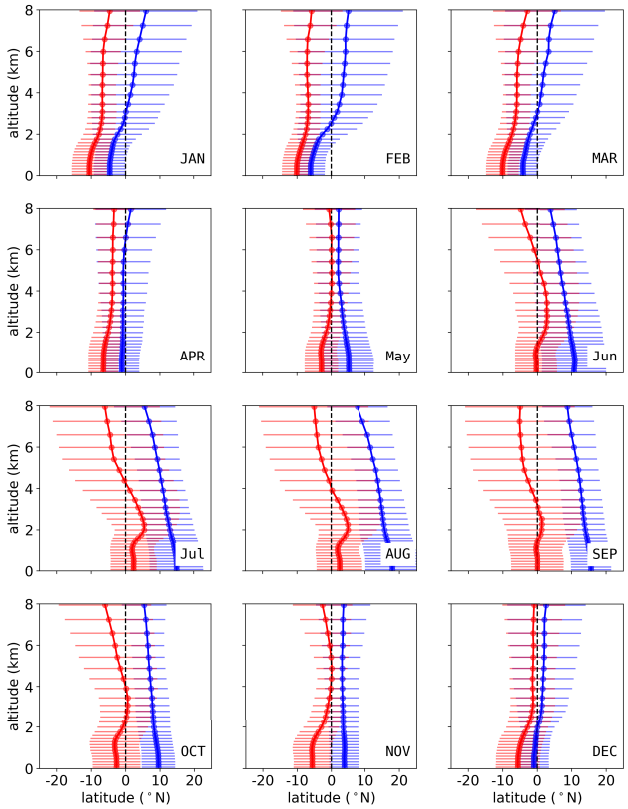

FIGURE 4.9: Monthly averaged (2015 - 2019) CE at different model levels from surface to 8 km. The CE-SH / CE-NH are zonally (100°E-180°) averaged over the TWP region see Figure 4.7. The blue lines show the CE-NH and the red lines show the CE-SH. The dashed black line shows the latitude =0.
1-σ of the CE-NH and CE-SH are given as thin horizontal lines in respective colours.

4.1.4 Tropical rain belt and CE

The rain belt is usually regarded as an indicator of the equatorial convergence zone and thus the boundary for interhemispheric exchange. However, the rain belt in the TWP region is relatively complex due to the seasonal variation of the WPM system. Here, we compare the rain rate with the CE in the TWP region: Figure 4.10 shows the zonal rain rate averaged from 2015 to 2019 and the results of the E1 and E2 simulation as a rate of occurrence, i.e. the number of days that the boundaries of the CE occur at each latitude as a percentage of the total appearance:

$$f_i = \frac{d_i}{\sum d_i}, \tag{4.4}$$

where f_i is the rate, i denotes the latitude, and d_i is the number of days that the CE-SH / CE-NH is located in the latitude i. A higher rate of occurrence indicates a more frequent latitudinal position of the respective CE boundary.

In general, as shown in Fig. 4.10, the meridional range of the CE is more concentrated within a single month compared to the area encompassed by the rain bands. From

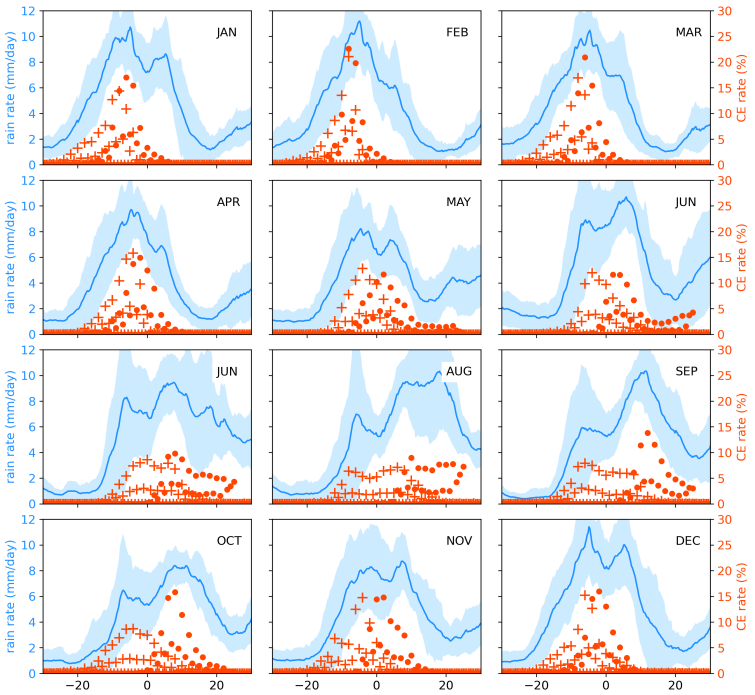

FIGURE 4.10: 5-year averaged (2015 - 2019) monthly rate of the CE-SH and CE-NH (red) with the rain rate (blue) from TRMM (Tropical Rainfall Measuring Mission) products 3B43 (monthly) (Huffman et al., 2007) as a function of latitude averaged over the West Pacific region (same definition as Figure 4.7). The CE-SH is marked by '+' and the CE-NH is marked by dots.

May to October, i.e. in summer and autumn, the southern and northern peak of the rain belt coincide at the southern and northern boundaries of IHT, CE-SH and CE-NH, respectively, indicating that the location of the north-south rain belt during this time is related to actual air mass exchange between the two hemispheres.

Both CE-NH and CE-SH tend to be located at the southern peak of the rain band in the winter and early spring, from December to March. During these months the northern rain band is outside the range of the CE and therefore seems not associated with IHT. This suggests that the northern branch of the rain belt is related to the NH circulation system at around 5 - 10°N.

The seasonal cycle of both CE-NH and CE-SH is shown in Figure 4.11 together with the rain rate in the TWP region. The meridional extent of the transition area between the NH and SH, i.e. the CE, varies with season. As already shown in the monthly results shown in Fig. 4.10, the CE is broader in NH summer than in other seasons. During NH winter (DJF, December–January-February) and spring (MAM, March-April-May), the CE is narrow and the northern part of the rain belt around 10°N is located north of the CE, while the southern part is included. This indicates, that the cause of the precipitation in the northern part of the TWP region is not the convergence of the equatorial flow from the NH and SH, but dependent on regional circulation within the NH. During NH summer (JJA, June-August) the meridional extent of the CE is the largest and includes the northern rain belt. During NH autumn (SON, September-November), the northern border, CE-NH, begins to retreat

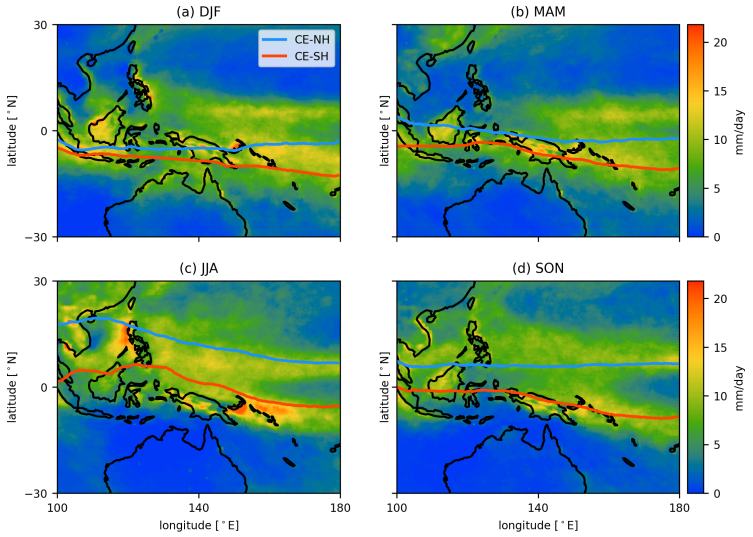

FIGURE 4.11: Seasonal rain rate (color scale) from TRMM (same dataset as Figure 4.10) in the TWP region with the blue line showing CE-NH and the red line showing CE-SH from 2015 - 2019. NH winter: December-February, DJF, NH spring: March-April, MMA, NH summer: June-August, JJA, NH autumn: September-November, SON.

southward, and the CE again becomes more narrow again over the Maritime continent and coincides with the two rain belts in the NH and SH.

4.1.5 Discussion and Summary

The CE is in general not always in agreement with the pattern of the tropical rain belt as defined and analysed by previous studies (e.g., Adam, Bischoff, and Schneider, 2016; Schneider, Bischoff, and Haug, 2014). The seasonal migration of the CE is more stable across the oceans than land, specifically in the East Pacific and the Atlantic. In these two regions, previous studies defined the convergence zone by either the tropical rain belt (Gu, Adler, and Sobel, 2005), low cloud-top temperature (Waliser and Gautier, 1993), or the magnitude of the horizontal gradient of divergence field (Berry and Reeder, 2014).

The seasonal migration of the CE on the continents is tied to the higher complexity of the atmospheric circulation system compared to the ocean. The circulation is modulated by several regional features such as local atmospheric jets and waves, proximity to the oceans, terrain-induced convective systems, moisture recycling, and spatiotemporal variability of land cover and albedo, so the location of the tropical rain belt becomes diffuse and does not coincide with the atmospheric boundary of the hemispheres (e.g., Arraut et al., 2012; Dezfuli et al., 2017; Magee and Verdon-Kidd, 2018). As mentioned in Sect. 4.1.2, the meridional extent of the CE above the continents South America and tropical America is larger than the one near ocean sectors. Considering the land-sea distribution and the complexity of the circulation system over tropical continents, more studies are needed on the regional circulation in tropical continental regions.

Previous studies (Hamilton et al., 2008; Petersen et al., 2010; Zhou et al., 2018; Müller, 2020) based on trace gas observations by aircraft, ozone soundings and FTIR spectrometers in the tropical regions were aimed to gain a better understanding of tropical dynamics. During NH winter, high concentrations of pollution tracers such as CO and Ozone from Southeastern Asia are transported towards the TWP by large-scale circulation, which is modulated by the migration of the CE (Hamilton et al., 2008; Müller et al., 2023c). The method also captured this phenomenon, which is shown in Fig. 4.11 (DJF). The region north of the CE-NH, at around 5°S, is considered the meteorological NH. The FTIR measurements at another tropical site, at Suriname, Paramaribo (5.8°N, 55.2°W), also suggest that the seasonal variation of CH_4 is highly related to IHT (Petersen et al., 2010). In Reunion Island (21°S, 55°E) a high spike of CH_4 coming from the NH was captured by the FTIR measurements in the local summer (December-February) (Zhou et al., 2018). As shown in Fig. 4.6, the CE is located around 20°S during this period, which is consistent with these observations. The consistent results of trace gas observations and our calculations of the CE for the tropical sites underline the potential of the CE as a good tool to determine airmass origin and improve our understanding of tropical dynamics.

In summary, this section introduces the determination method of CE indicating the region where IHT occurs. Daily values of the CE show reasonable agreement with the pattern of the tropical rain belt. By comparing the CE with the wind field in different regions, we find that the confluence of the equatorial flow is consistent with the CE where IHT occurs in the Central & Eastern Pacific and the Atlantic Ocean. In Africa, where the confluence zone is north of the CE, further investigations are needed. The vertical extent of the CE varies with the seasons. It slopes northward from the ground to higher altitudes in winter, is nearly perpendicular to the ground in the spring, and slopes southward in the summer. The tilt of the CE diminishes in the fall and returns to a pattern that is vertical to the ground. The Focuse is on the relationship between the CE and the tropical rain belt in the TWP region. The north-south migration of the CE is not always consistent with the maximum rain rate during the year, especially in the TWP region.

Considering that air mass exchange is a continuous process, we performed simulations with a passive tracer release both in the NH and SH. Its extent varies with season and region. Two cases set in the two symmetry fluxes region in the NH and SH help to obtain a complete pattern of the IHT. This mixing process happens in a transition area, with a continuous gradient rather than a single border separating the atmosphere in the NH and SH. From this transition area, we find that the northern part of the precipitation band in the TWP in winter is more likely caused by the regional circulation rather than the convergence of the equatorial flow from the NH and SH. By combining the CE determined from the two cases, we thus get further insights into the IHT in the TWP region.

4.2 Characterization of trace gases by CE

In the previous Section 4.1, a new tool Chemical Equator (CE) was introduced to investigate interhemispheric air mass transport (IHT) in the tropical region by passive tracer simulations with GEOS-Chem. The so-called CE indicates the region where IHT occurs. This tool, CE, can help us characterize the trace gases, specifically, in the TWP region. In this section, the simulation results will be complemented by

more observational data and measurements from different approaches, such as the ozone balloon sonding, FTIR spectrometer and satellite. Using the CE in combination with observations will allow a more detailed characterization of trace gas transport, sources and sinks in the TWP region.

4.2.1 Measurement and simulation result of trace gases

CO measurements by FTIR spectrometer

The CO measurements are obtained from the FTIR spectrometer. To retrieve the profiles of CO, NDACC spectra in Palau are analyzed with the SFIT4 algorithm. The AVKs for NDACC solar absorption CO retrievals are shown in Figure 4.12. As shown in the Figure (Section 3.2.2), the retrievals have a good sensitivity to the lower and mid-troposphere below 8 km. As described in Section 3.2.2, the trace of matrix AVK, often denoted as Degrees of Freedom (DOF) for signal, indicates the number of independent pieces of information used in the inversion process. The averaged DOF in of CO is 1.1 (0.2, 1σ), which indicates that there is one layer of the information with high sensitivity below 8 km, see Figure 4.12.

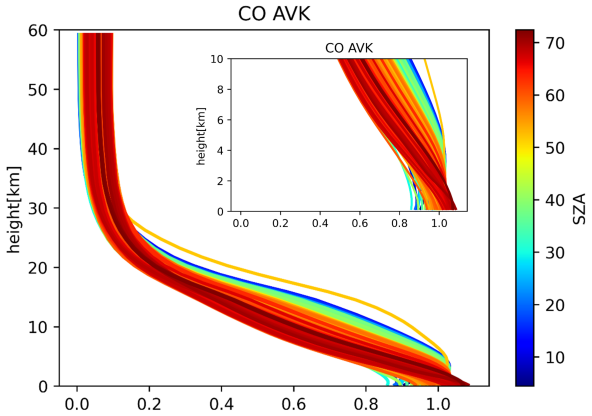

FIGURE 4.12: The column absorption AVKs of CO varies with the solar zenith angle (SZA)

.

The total column of CO (TC_{CO}) is retrievd from the FTIR. The dry-air column-averaged mole fraction of CO (X_{CO}) is the fraction of the total column of gas to the total column of dry air (TC_{air}):

$$X_{CO} = \frac{TC_{CO}}{TC_{air}}, \tag{4.5}$$

$$TC_{air} = \frac{P_s}{g m_{air}^{dry}} - TC_{\mathrm{H_2O}} \frac{m_{\mathrm{H_2O}}}{m_{air}^{dry}}, \tag{4.6}$$

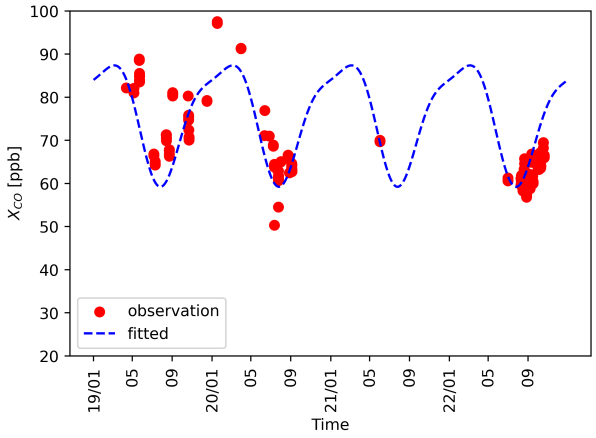

FIGURE 4.13: The time series of the X_{CO} measured by FTIR spectrometer and the fitted measurements in Palau.

where P_s is the surface pressure. TC_{H_2O} is the total column of H_2O. The constant g, m_{H_2O} and m_{air}^{dry} is the gravitational acceleration, molecular mass of H_2O and dry air respectively.

A periodic function as described by Zhou et al. (2018), with a period of 1 year was used to fit the time series of X_{CO}, which is:

$$y(t) = a_0 t + a_1 sin(2k\pi t + F_1) + a_2 sin(2k\pi t + F_2) + c + \epsilon, \tag{4.7}$$

where a_1, a_2, F_1, F_2 are periodic parameters, $y(t)$ is the fitted measurements (X_{CO}) as a function of t which is the day of year. $a_0 t$ is the annual growth. The term $a_1 sin(2k\pi t + F_1)$ and $a_2 sin(2k\pi t + F_2)$ are the periodic variations, representing the seasonal cycle. c is the intercept. ϵ is the residual between the measurements and fitting function.

The measurements and the fitted function of X_{CO} are shown in Figure 4.13. The X_{CO} is lowest from July to September (< 70 ppb) and there are enhancements in from January to May (> 85 ppb). The extreme minimum measurements of X_{CO} (<60 ppb) in the summer of 2020 could be caused by the lockdown in the nearby regions such as Malaysia or the Philippines and locally in Palau because of the Corona pandemic. Since the measurements of X_{CO} is of the most sensitivity from surface to 8 km (see Figure 4.12), the variations of X_{CO} throughout the year can be used to characterize the tropospheric air combined with the model simulation of CE.

Lower and mid tropospheric O_3 measurements by ozone sondes

The O_3 measurements are obtained by ECC ozone soundes lanched in PAO. From the balloon-borne observations, the profiles of O_3 are obtained. To obtain the local tropospheric O_3, the dry-air column-averaged mole fraction of O_3 in the lower and mid troposphere is calculated. In this study, the layer between the surface and 8 km are taken as the lower and mid troposphere, which is consistent with the most sensitive layer of CO measurements by FTIR. Similar to Equation 4.5, but the total

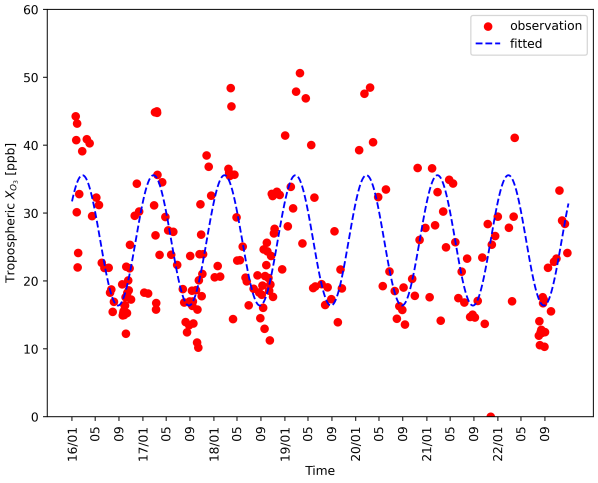

FIGURE 4.14: The time series of the tropospheric X_{O_3} measured by ozone sondes and the fitted measurements in Palau.

column of gas (TC_{gas}) and air (TC_{air}) are replaced by the partial column of O_3 (PC_{O_3}) and air (PC_{air}) in the layer between surface and 8 km, which is calculated by:

$$TroposphericX_{O3} = \frac{PC_{O_3}}{PC_{air}}, \tag{4.8}$$

$$PC_{O_3} = \int_0^{7km} n_{O_3} dz / \int_0^{7km} n_{air}^{dry} dz, \tag{4.9}$$

where the n_{O_3} and n_{air}^{dry} is the molecular number of O_3 and dry air which can be obtained from the ozone sonde measurements.

The measurements and the fitted function (same format as CO, Equation 4.7) of tropospheric X_{O_3} are shown in Figure 4.14. Similar to the X_{CO}, there are peaks of tropospheric X_{O_3} (> 40 ppb) from January to May in NH winter and early spring, and lower (< 20 ppb) in the NH summer from July to September. These seasonal variations of the tropospheric X_{O_3} as well as the X_{CO} are much related to the different airmass origins throughout the year, which can be characterized by the CE and will be described in Section 4.2.2.

CH_4 and CO measurements by satellite

Column-averaged dry air mole fractions of CH_4 and CO (X_{CH_4} and X_{CO}) are obtained from the radiance measurements from the TROPOspheric Monitoring Instrument (TROPOMI) aboard the Sentinel-5 Precursor satellite mission (Veefkind et al., 2012). Here I use the latest release of the WFMD (Weighting Function Modified Differential Optical Absorption Spectroscopy) product (v1.8) (Schneising et al., 2023) and interpolate it onto a 2° × 2° grid. For this, each measurement is assigned to a single grid cell and the weighted average of all measurements per cell is calculated. For details about the satellite mission, please see Appendix B.1.

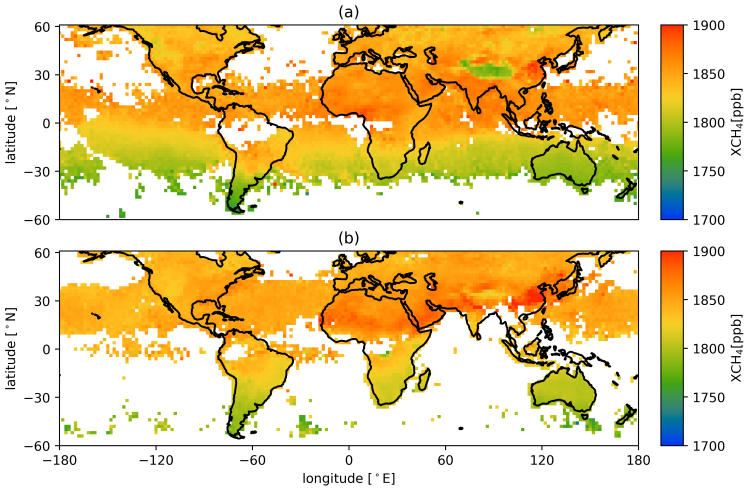

FIGURE 4.15: Sentinel-5 Precursor satellite X_{CH_4} vertical columns (ppbv) averaged for (a) January 2019 and (b) July 2019.

Figure 4.15 and Figure 4.16 display the X_{CH_4} and X_{CO} measurements from Sentinel-5 Precursor satellite data products. In July, there are data gaps in the SH ocean area for CH_4, primarily due to retrieval algorithm issues specific to methane. Both X_{CH_4} and X_{CO} exhibit noticeable latitudinal gradients, with higher concentrations in the Northern Hemisphere and lower concentrations in the Southern Hemisphere.

Within regions in the tropics, such as tropical Indian Ocean in Figure 4.15 (a), Figure 4.16 (a) and (b) significant gradients in X_{CH_4} and X_{CO} are observed between the Northern and Southern Hemispheres. Moreover, localized enhancements in X_{CO} are observed in specific regions, such as central Africa, Southeast Asia, and northern South America. These enhancements obscure the sharp north-south gradient in the tropics, indicating complex spatial patterns.

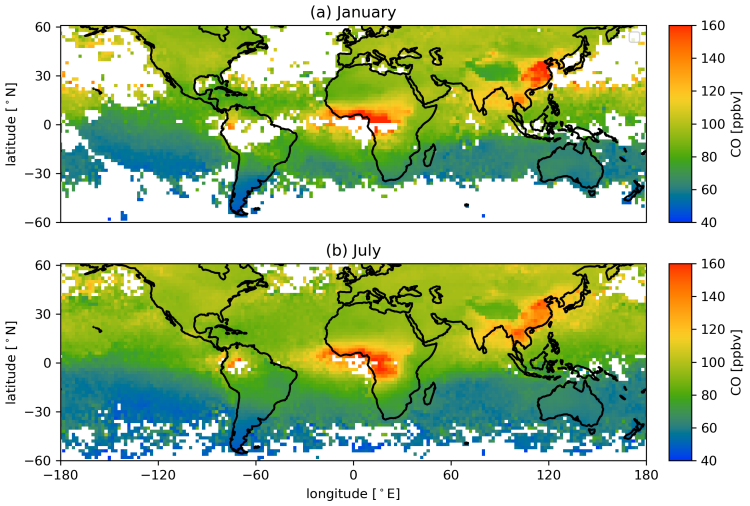

FIGURE 4.16: Sentinel-5 Precursor satellite X_{CO} vertical columns (ppbv) averaged for (a) January 2019 and (b) July 2019.

SF_6 Simulations by GEOS-Chem

SF_6 is a common tracer to constrain time scales of IHT (e.g., Geller et al., 1997; Waugh et al., 2013; Yang et al., 2019) and thus to characterize the trace gases measurements. Simulations of SF_6 were conducted using GEOS-Chem, as described in Section 3.4.1. Figure 4.17 illustrates the results of these simulations. Similar to CH_4 and CO (shown in Figures 4.15 and 4.16), there is a noticeable latitudinal gradient in the concentration of SF_6.

In both January and July, a clear and sharp north-south gradient in SF_6 concentration is observed in the latitude band near the equator. However, there is also a regional variation in SF_6 emissions in specific areas, such as Southeast Asia and North America. In these regions, emissions obscure the boundary between the NH and SH, affecting the overall distribution of SF_6.

The sharp gradients in trace gases within the tropics suggest an IHT phenomenon between the hemispheres. The boundary of this IHT phenomenon can be delineated by CE and will be further discussed in the following section.

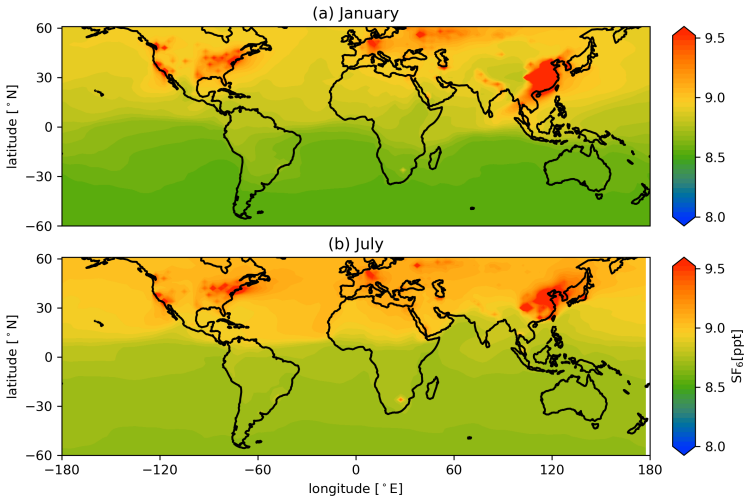

FIGURE 4.17: SF_6 surface concentration (ppb) simulated by GEOS-Chem averaged for (a) January 2019 and (b) July 2019.

4.2.2 Characterization of trace gases by CE in TWP

In Section 4.1, a novel method called CE is introduced to investigate interhemispheric air mass transport (IHT) in the tropics through passive tracer simulations using GEOS-Chem. The term CE stands for the area where IHT takes place. The seasonal shift of the CE reflects alterations in the circulation system, leading to varied sources of air masses in specific regions. Therefore, combining CE analysis with trace gas measurements allows for a more precise characterization of the concentration variations of these trace gases in the TWP region.

Figure 4.18 illustrates the annual motion and zonal mean 10-m wind vector for the TWP region CE. Comparing the latitude of Palau with that of CE, it is evident that Palau is situated in different hemispheres at different times of the year. From

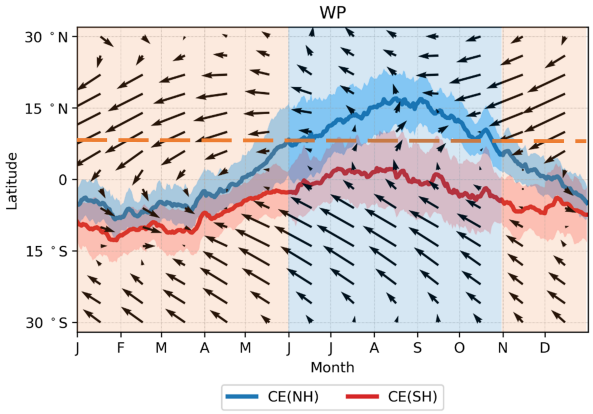

FIGURE 4.18: Monthly averaged wind vectors (black arrows) and annual movement of the daily CE in TWP with color shading to distinguish the relative positions of Palau and CE.
The blue lines show the NH boundary and the red lines show the SH boundary. The latitude of Palau is marked by the dashed orange line. The orange-shaded area denotes the period when Palau is located in the north of the CE, and the blue-shaded area denotes the period when Palau was located in the south of the CE.
The wind data are the 10-m winds from the ERA5 reanalysis data (Hersbach et al., 2020) averaged from 2015 to 2019. Both the CE and the wind field are space averaged zonally in the TWP region.

November and December to May of the following year, Palau is in the southern hemisphere because its latitude is north of CE. Conversely, from June to October, Palau is in the NH, specifically in the transition zone, as its latitude falls within the CE area.

This result suggests that the air masses over Palau have different origins depending on their position relative to the CE. Further analysis of the monthly average wind field reveals that from November and December to May of the following year, the air mass over Palau is primarily influenced by NH air masses, highlighted by the orange-shaded area in Figure 4.18. Conversely, from June to October, the atmosphere over Palau is predominantly shaped by SH air masses or in the transition area of the CE, marked by the blue-shaded area.

This seasonal change in CE can be used to characterize variations in the atmospheric trace gas content throughout the year. Figure 4.19 shows the characterization of X_{CO} obtained from FTIR measurements by CE. As mentioned previously (section 4.2.1), X_{CO} is lowest from July to September (< 70 ppb) and highest from January to May (> 85 ppb). The orange-shaded area (November, December to May) indicates that the Palau location is in the north of CE, so the air comes from NH, bringing higher concentrations of CO. FTIR spectrometer measurements of X_{CO} also show maximum values from January to May. In contrast, during other times of the year (June to October), Palau is located in SH and has lower X_{CO} as measured by the FTIR spectrometer. The same features can be seen for the characterization of tropospheric O_3 measurements. Most tropospheric maximum O_3 measurements are obtained during periods when the CE is south of Palau and vice versa.

To better understand the implication of the CE position on air composition, satellite

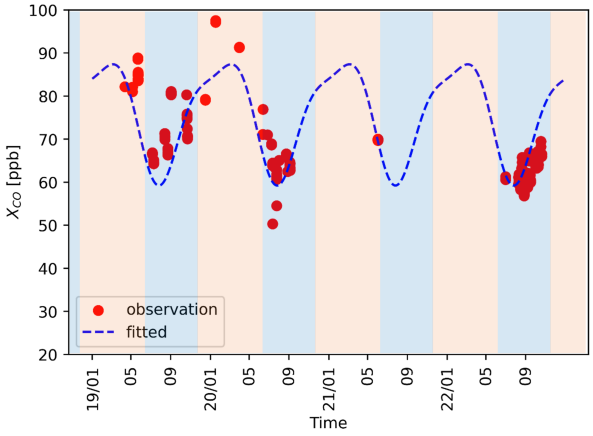

FIGURE 4.19: The time series of the X_{CO} measured by FTIR spectrometer and the fitted measurements in Palau, with color shading to distinguish the relative positions of Palau and CE.
The shaded area corresponds to the Figure 4.18, where the orange-shaded area denotes the time period when Palau locates in the north of the CE, and the blue-shaded area denotes the time period when Palau locates in the south of the CE.

measurements of X_{CH_4} and X_{CO} and model simulation of SF_6 are presented together with the CE in Figure 4.21, Figure 4.22 and Figure 4.23. The CE and the north-south gradient of CH_4 in the Indian Ocean and Eastern Pacific in January and Africa in July are well consistent with each other. For CO, the sharp gradient of X_{CO} is also consistent with the location of CE, apart from some hotspots with high X_{CO} emission, for example, southeast Asia and mid-Africa. This indicates the CE has good potential to illustrate the IHT inferred by observations.

However, due to the lack of data coverage, it is relatively difficult to see the distribution of X_{CH_4} in the SH in July. The X_{CH_4} distribution is also affected by sources in the SH and chemical removal process. This means the X_{CH_4} is not monotonically rising like the inert artificial tracer used in our study and does not show a clear distinction between NH and SH. For SF_6, there are large emissions in South East Asia, which may be emitted into the CE area, and the SH emission in South America, which may impact the latitudinal gradient of the SF_6. Apart from those emissions regions, the SF_6 distribution mostly shares the features of an artificial tracer, i.e. the monotonic rise, and therefore has been used for similar studies(e.g., Geller et al., 1997; Waugh et al., 2013; Yang et al., 2019).

4.2.3 Summary and discussion

Multiple instruments including ozone sonde and FTIR spectrometry have been used to obtain measurement of trace gases since 2016. Seasonal changes in CO and O_3 are associated with large-scale circulation and exchanges between the two hemispheres. The low CO and O_3 are in summer and early autumn and high CO and O_3 in winter and early spring can be characterized by the seasonal shifts of the CE.

Both trace gases with different measurement approaches such as ground-based FTIR spectrometer, ozone sonde and satellite can be characterized by CE. For trace gases

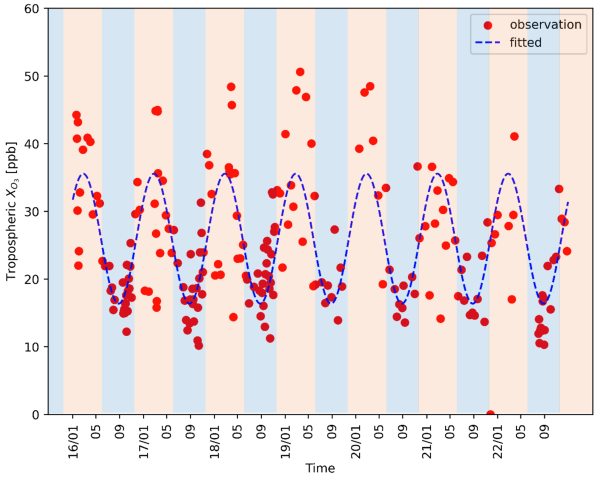

FIGURE 4.20: The time series of the tropospheric X_{O_3} measured by ozone sondes and the fitted measurements in Palau and the fitted measurements with color shading to distinguish the relative positions of Palau and CE.
The shaded area corresponds to the Figure 4.18, where the orange-shaded area denotes the time period when Palau locates in the north of the CE, and the blue-shaded area denotes the time period when Palau locates in the south of the CE.

measured in a single site, the seasonal variations of the trace gas measurements are well constrained by the distinguish relative positions of the site and CE in a specific region. The global distribution of trace gases obtained from satellite and model also shows the well consistency between the north-south gradient and CE. The consistent results of trace gas observations and our calculations of the CE for the tropical sites underline the potential of the CE as a good tool to determine airmass origin and improve our understanding of tropical dynamics.

Besides, to assess regional differences only caused by air mass transport, the chemistry in the model is switched off to develop an atmospheric pattern only due to the transport by the analyzed wind fields. Since CE is simulated and calculated through artificial trace gases with constant emission and no chemical process, chemical processes and regional dependency of the emissions occurring for real species like CO and SF_6 can be neglected.

CH_4 have a relatively long lifetime and clear latitudinal gradient which has the potential as tracers to investigate IHT (Patra et al., 2011; Law et al., 2008; Lin and Rood, 1996). The atmospheric tracer transport model intercomparison project (Trans-Com) investigated IHT by non-reactive tropospheric species such as CO_2, CH_4 and SF_6 and provided a comprehensive understanding of the differences in tracer distribution between the northern and southern hemispheres and studies IHT (Krol et al., 2018). It has a very long atmospheric lifetime (580 - 3200 yr) (Ravishankara et al., 1993; Morris et al., 1995; Ray et al., 2017), a large and constant growth rate during the last two decades (Rigby et al., 2010; Hall et al., 2011) and anthropogenic sources primarily over the NH. However, tracers with significant north-south gradients (such as CO, CH_4 and SF_6) are locally diverse and can be affected by human activities. So, to eliminate the regional dependency on human activities and the chemical processes with other species, an artificial tracer without such features as used in this study, the CE

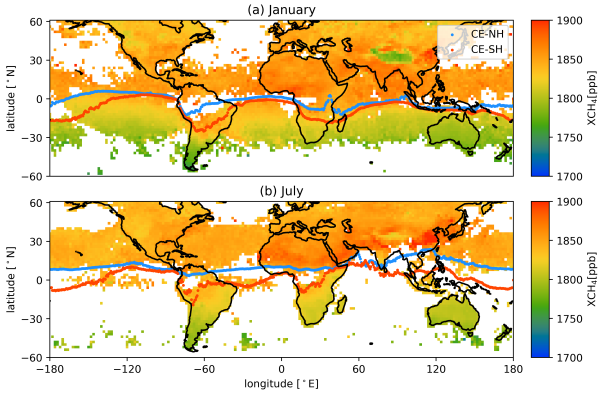

FIGURE 4.21: CE with Sentinel-5 Precursor satellite X_{CH_4} vertical columns (ppbv) averaged for (a) January 2019 and (b) July 2019. The blue dots show the NH boundary and the red dots show the SH boundary.

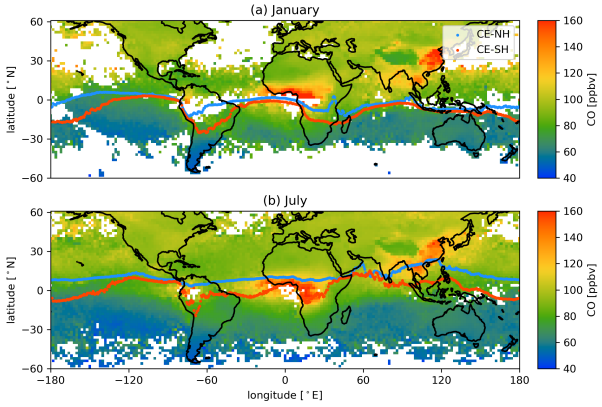

FIGURE 4.22: CE with Sentinel-5 Precursor satellite X_{CO} vertical columns (ppbv) averaged for (a) January 2019 and (b) July 2019. The blue dots show the NH boundary and the red dots show the SH boundary.

simulation, is better to investigate IHT and characterize the trace gas measurements in the tropics.

The simulation results will be complemented by more observational data such as the ground-based observation network in the future. Using the CE in combination with observations will allow a more detailed characterization of trace gas transport, sources and sinks in the TWP region. Since the TWP is an area of the active troposphere to stratosphere exchange, the seasonal and in particular vertical characteristics of the CE will be valuable for studies of troposphere to stratosphere exchange.

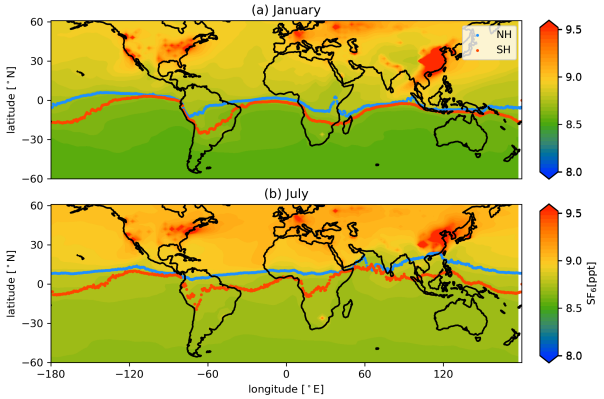

FIGURE 4.23: CE with SF_6 surface concentration (ppb) simulated by GEOS-Chem averaged for (a) January 2019 and (b) July 2019. The blue dots show the NH boundary and the red dots show the SH boundary.

4.3 Cirrus cloud measured by ground-based Lidar

In this section, measurements, and analysis of cirrus cloud by the polarization lidar, COMCAL, from 2018 to 2022 over Koror, Palau in the TWP region are presented. The long-term observations from ground-based lidar can provide intensive and extensive measurements over one specific region compared to satellite data with coarse temporal resolution. Thus, it can improve the understanding of the formation mechanisms of the cirrus cloud in different seasons and meteorological conditions over the TWP region, where the region is thought to be an essential pathway of STE (Fueglistaler, Wernli, and Peter, 2004; Rex et al., 2014). This study aims to analyze the cirrus geometrical and optical properties at the TWP region from observations derived by the ground-based lidar system, which partly fills the gap concerning the coverage of existing ground-based lidar studies in this region.

4.3.1 Occurrence of the cirrus cloud from Lidar measurement

From April 2018 to August 2022, we get 332 hours of measurements within 10 months. A total of 140 days can be used and cirrus are detected. To assess the impact of cirrus clouds on regional climate, understanding their frequency is crucial, especially in tropical regions, and across various months and seasons. To achieve this, the percentage occurrence (PO) of cirrus clouds at different altitude levels is calculated using COMCAL lidar cloud layer datasets. This calculation involves determining the ratio of profiles with cirrus clouds at a specific altitude bin to the total number of profiles available. The duration is quantified for which cirrus clouds appear in various altitude bins whenever lidar is activated to study the PO of cirrus clouds as a function of altitude and time. The ratio of the cirrus cloud occurrence time to the overall lidar duration time at each altitude bin yields the cirrus cloud PO at that altitude bin (Pandit et al., 2015). The PO are quantified at each altitude bin of 0.1 km from 10 km to 20 km.

The time series of the monthly mean PO of cirrus clouds in Palau from April 2018 to August 2022 is shown in Figure 4.24. The number of cirrus layers detected by Lidar is shown by the number in Figure 4.24. The peak altitude of PO occurs in the range of

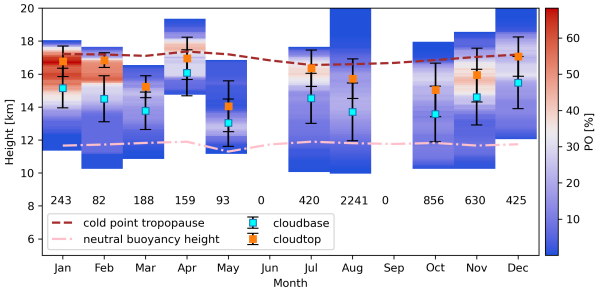

FIGURE 4.24: Cirrus monthly percentage occurrence (PO) in Palau by ComCAL. The numbers in the figure refer to the detected cirrus layers. The cyan and orange square with 1-σ shows the height of the cloud base and the top of the cloud base. The height of CPT and LMS averaged in each month was calculated by the meteorology profiles from radiosondes by the Weather Service Office of Palau, the same as Figure 4.30.

15 km to 18 km in most months, with lower PO values near LMS altitude. This indicates that cirrus clouds frequently occur in the upper part of the TTL (above 15 km), close to the CPT, while cirrus clouds occur less frequently at the lower boundary of the TTL. The seasonal pattern of the height of the cirrus cloud layer and the peak of PO is consistent with the CPT, with minimal in July and August then increasing till December and from January to March next year stable, the reach to maximal height in April.

On a yearly average, as shown in Figure 4.25, the PO are quantified in each season against altitude The maximum PO of cirrus clouds is 22% at about 16 km and 1 km beneath the height of the CPT. From December to February (December-January-February, DJF), the PO is the largest with a peak in 16 km of 42%. There is the largest faction of cirrus above the CPT in DJF compared to other seasons, followed by March-April-May (MAM), and the least in June-July-August (JJA). In MAM, there are two peaks of PO in TTL, one at around 13 km and another slightly above or around the CPT. This feature in spring is different from other seasons with only one peak below the height of CPT. The previous one-month campaign conducted by Cairo et al., (2012) in spring also reported this two-peak feature of the cirrus cloud over Palau (Cairo et al. (2021), Figure 3). For details about the PO of cirrus in each month, please see Appendix B.2.

4.3.2 Properties of the cirrus cloud over Palau

Geometrical and Thermodynamic Properties of Cirrus Cloud

The frequency of occurrence of geometrical properties, which are the Geometrical Thickness (GT), cloud base and cloud top height and thermodynamic properties, which are cloud base and top temperature and mid-cloud temperature are shown in Figure 4.26 and Figure 4.27, respectively. The statistical details are given in Table 4.2.

The geometrically thinnest cirrus layer is in spring (mostly less than 2 km), followed by autumn and winter and the geometrically thickest in summer, as shown in Figure

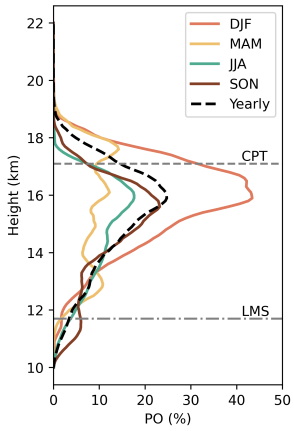

FIGURE 4.25: PO of cirrus in Palau during December-January-February (DJF, red line), March-April-May (MAM, yellow line), June-July-August (SON, green line), Septermber-October-November (SON, brown line) and yearly averaged (dashed black line). Yearly mean height CPT (grey dashed line) and LMS (dotted dashed) are shown.

4.26a-e. Only in winter and summer, the GT is more than 4 km with a frequency of 2% and 10%, respectively. The annual averaged GT of cirrus is mostly distributed between 1 - 2 km with an annual average of 1.4 ± 0.7 km (see Table 4.2), and only a few cases more than 4 km.

The distribution of the Cloud base height is spread between 10 and 18 km, shown in Figure 4.26 j. In winter, the height of the cloud base is slightly higher than in the other seasons with an average value of 15.3 ± 1.4 km (see Table 4.2), compared with around 14 km in other seasons (Figure 4.26 f-j). For the distribution of cloud top, see Figure 4.26 k-o, the annual peak is 17 km. The higher the cloud top is the more frequent they become, except in spring, where we see a second maximum below 13 km. In winter, the probable range of the height of the cloud top is narrower between 14 and 17 km, compared with other seasons between 12 and 17 km.

The temperature of the cloud is derived from the radiosondes launched each day at 12h UTC by the Weather Service Office of Palau. The cloud layers are matched with the temperature profiles launched at 12:00 UTC / 21:00 local time. As shown in Figure 4.27 a-e, the cloud base temperature is evenly distributed between -85 °C and -45 °C with frequency around 0.1 to 0.2, and the average cloud base temperature is -71.7 ± 11.5 °C (see Table 4.2). For the cloud top temperature, the most probable temperature is concentrated in the range -85 °C and -80 °C with a frequency of about 0.4, shown in Figure 4.27 f-j. This is a very cold temperature and approaches the temperature of the annually averaged CPT (-83.8 °C), see Figure 4.30. Except for spring, the highest frequency range of cloud top heights in the other three seasons were all between -85 °C and -80°C, and the frequencies all reached 0.4. As for the mid-cloud temperature, shown in Figure 4.27 k-o, the distribution is similar to the cloud top temperature. The coldest cirrus layer is in winter. The mid-cloud temperature of less than -85 °C only occurred in winter with a frequency of 0.14. The annual mean of the mid-cloud temperature is -73.8 ± 9.8 °C.

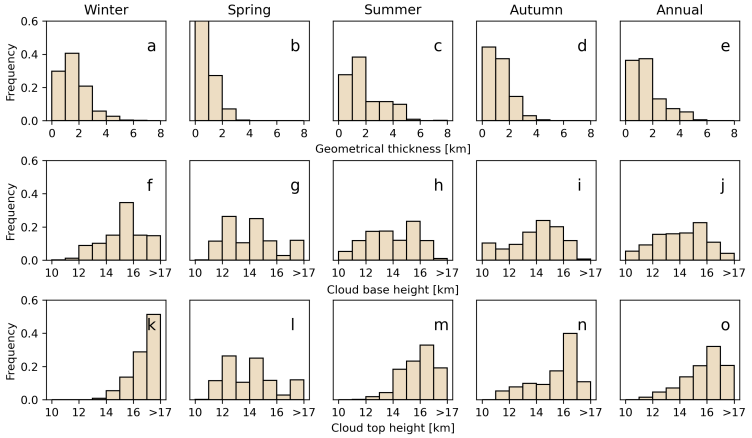

FIGURE 4.26: Frequency of occurrence of the seasonal and annual GT of cloud (a-e), cloud base height (f-j) and cloud top height (k-o). The bin size is 1 km.

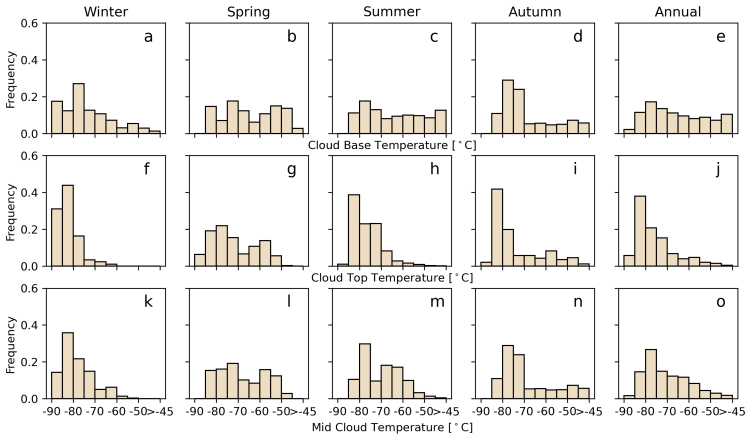

FIGURE 4.27: Frequency of occurrence of the seasonal and annual cloud base temperature (a-e), cloud top temperature (f-j) and mid-cloud temperature (k-o). The bin size is 5 ° C.

Optical Properties of Cirrus Cloud

An overview of the optical properties of cirrus including Cloud Optical Depth (COD), depolarization, and color ratio (CR) are presented in Figure 4.28 and the statistical details are listed in Table 3. According to our measurements, the COD is distributed in a broad range with a minimum of 0.001 and a maximum of 2.1. It can be seen from Figure 4.28a-e that the COD is mainly concentrated in the range of 0-0.2. In all seasons, the fraction of a COD between 0 and 0.1 is about 0.75. The annual average COD is 0.25, and only in summer, the average COD is larger than 0.3, followed by 0.19 in autumn, the winter and the lowest COD in spring, see Table. 3. From the frequency distribution, compared with other seasons, only summer has a larger number of clouds with a COD of 0.3 to 0.5 (Figure 4.28c).

The depolarization ratio is ranging from values very close to zero to 0.69. As shown in Figure 4.28f-j, the frequency of the range 0-0.1 is slightly larger than other ranges,

TABLE 4.2: Seasonal and annual mean and standard deviation statistics for cirrus geometrical and optical properties

Cirrus Properties	Annual	Winter	Spring	Summer	Autumn
Cloud base temperature (° C)	-71.7 ± 11.5	-73.7 ± 10.9	-67.9 ± 12.5	-63.4 ± 13.6	-64.5 ± 13.4
Cloud top temperature (° C)	-75.9 ± 9.0	-82.5 ± 4.8	-71.9 ± 10.1	-76.4 ± 6.8	-73.9 ± 11.4
Mid-cloud temperature (° C)	-70.4 ± 10.4	-78.1 ± 7.1	-67.9 ± 10.8	-69.9 ± 9.0	-69.0 ± 12.0
Geometrical thickness (km)	1.5 ± 0.9	1.6 ± 0.9	1.0 ± 0.5	1.9 ± 1.2	1.4 ± 0.7
Cloud base height (km)	14.1 ± 1.7	15.3 ± 1.4	14.0 ± 1.7	13.9 ± 1.8	14.0 ± 1.7
Cloud top height (km)	15.8± 1.4	16.9 ± 1.0	15.1 ± 1.6	15.8 ± 1.2	15.4 ± 1.6
COD	0.25 ± 0.45	0.17 ± 0.33	0.15 ± 0.30	0.33 ± 0.53	0.19 ± 0.35
ETTCi[1]/SVC/Thin/Thick (%)	1.6/32/46/22	6.2/39/47/14	2.0/46/43/11	0.7/28/43/29	0.6/32/54/14
Colour ratio (355/532)	1.6 ± 0.5	1.5 ± 0.5	1.6 ± 0.4	1.1 ± 0.1	1.6 ± 0.5
depolarization ratio (%)	31 ± 19	34 ± 22	25 ± 16	36 ± 18	24 ± 16

[1] ETCCi (Immler et al., 2007) is a customized sub-classification of cirrus with an optical thickness defined as less than 0.005, which belongs to SVC. The sum of the fraction of SVC, Thin and Thick cirrus equals 1, which should not include the fraction of ETTCi.

about 0.19, followed by the range 0.3-0.4, about 0.18. The depolarization ratio is slightly lower in spring and autumn than in winter and summer. However, all seasonal averaged values of the depolarization ratio are closed to 0.3 (Table 4.2), which indicates the ice cloud particles are irregular in most cases.

As for the CR, shown in Figure 4.28k-o, it varied mainly between 1.1 and 2.5, with an annual average of 1.6 ± 0.5. In summer, the CR is much lower than in other seasons, with a high frequency (0.85) of CR between 1.1 and 1.25. This indicates that there are bigger ice particles during summer than in other seasons. This also can be explained by the movement of the CE. During the monsoon season, when Palau is located in the south of the CE or in the transition area, the TTL is humid and warm because of the intensive convective activities during this time. Under this circumstance, a great amount of deep convective cells occur in tropical oceanic regions and generate the spreading anvils with long-lived cirrus with larger particle size compared with in the other seasons. Comparing our CR values (annual mean of 1.6 ± 0.5) with similar studies, Voudouri et al. (2020) reported CR values of 1.50 ± 0.80 in Gwal Pahari (28.43 °N, 77.15°E) in India and 1.40 ± 1.10 in Elandsfontein (26.25°S, 29.43°E) in South Africa, aligning with our results.

Figure 4.29 a shows the frequency of clouds with different values of COD against the cloud base. Visible thick and thin cirrus occurs in 12 - 14 km, and the cirrus becomes optically thinner at higher altitudes. SVC usually occur in 16 km. Apart from the three typical types of cirrus as defined by Sassen and Cho (1992), we use a subdivision definition of the cirrus cloud of COD less than 0.005, which is an Extremely Thin Tropical Cirrus (ETTCi), adapted from Immler et al. (2007). ETTCi account for 1.6% of the total number of cirrus measured over Palau, and the peak of frequency altitude of 18 km for ETTCi is even higher than the peak of CPT (17 km), see the dashed line in Figure 4.29 a. The dehydration of tropospheric air before it enters the stratosphere is associated with the occurrence of the occurrence of ETTCi. The details about the STE and the measurements of the clouds will be discussed in section 4.4.

The seasonal and annual occurrence of different types of cirrus is shown in Figure 4.29 b. The most prevalent type of cirrus in Palau is the optically thin cloud accounting for 47%, followed by SVC (32%) and thick cirrus (22%), and the least is ETTCi (0.27%). The SVC has a higher frequency of occurrence in spring and winter than in summer and autumn. In summer, thick cirrus and SVC appear at almost the same frequency (about 28%), which is also the season with the highest frequency of thick cirrus. For ETTCi, this cirrus was observed only in winter and summer, with a higher frequency in winter (0.89%).

4.3.3 Comparison of the cirrus cloud in different tropical sites

There have been many previous studies using airborne in-situ instruments and ground-based lidars to measure cirrus clouds in the tropical region with the probably earliest back to 1976 by (Uthe and Russell, 1977) in Kwajalein island (8°N, 116°N) to many different sites, e.g. Platt, Scott, and Dilley (1987), Platt et al. (1998), Sassen and Benson (2001), Comstock and Jakob (2004), Pace et al. (2003), Das, Chiang, and Nee (2009), Pandit et al. (2014). However, there is still a lack of information and knowledge that needs to be filled by long-term measurement over the TWP region. This study partly filled the gap of measurements in this region.

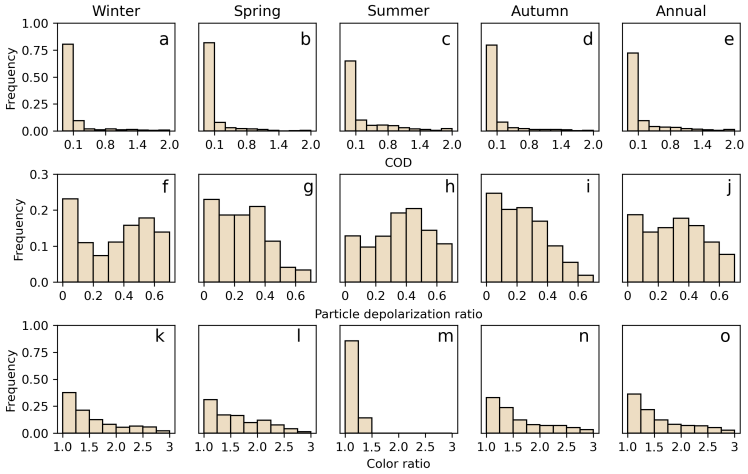

FIGURE 4.28: Frequency of occurrence of the seasonal and annual COD (a-e) particle depolarization ratio (f-g) and color ratio (k-o). The bin size for a-e is 0.2, for f-j is 0.1 and for f-j is 0.25.

The cirrus clouds observed in Palau are colder compared with other places in the tropics , see Table 4.3. Table 4.3 shows an overview of the cloud properties in the tropical site and the results from satellite measurements (Tropics ± 30°). From Table 4.3, compared with other stations in the tropics, Palau has higher CBH and CTH. Except for Nauru Island (Comstock and Jakob, 2004), which is also located in the warm pool, the western Pacific Ocean, its CTH is 16.5-17.0 km, which is similar to that of Palau. Besides, the cloud temperature in Palau is the lowest, which can be explained by the fact that the western Pacific region has the lowest temperatures at TTL (Fueglistaler, Wernli, and Peter, 2004).

The results of the coldest cloud above Palau shed light on the possible transport pathways from the TTL to the stratosphere. Although transport pathways and mechanisms of tropospheric air masses across TTL remain an active research question and need to be studied in detail. This possible transport pathway needs to be further investigated through trajectory models focusing on the temperature and humidity history of the cirrus cloud.

4.3.4 Summary and discussion

In this section, the measurements and analysis of cirrus clouds are presented. The overall percentage occurrence of cirrus over Palau is 51.3% of the entire sampling time of the lidar. The annual mean GT of cirrus cloud is about 1 – 2 km, rarely with GT higher than 3 km. The cloud base height of the cirrus is evenly distributed in all seasons between 10 and 18 km. The cloud top height is concentrated mainly at 15 - 17 km, which is close to the CPT, especially during winter. A previous study based on the ground-based Lidar in Palau during the spring season by Cairo et al. (2021) showed cloud occurrence extends throughout the whole TTL with two defined peaks, one at 10-13 km and the other at or below the CPT. Our results of PO in the spring season (MAM), see Figure 4.25 are partly consistent with it, one at around 13 km and another slightly above or around the CPT. This feature in spring is different from other seasons. As Cairo et al. (2021) suggested, this feature measured

TABLE 4.3: Statistics for cirrus properties in the tropical region.

Site	CBH	CTH	GT	Temperature	Literature
Koror (7.3°N, 134.5°E)	**14.1 ± 1.7**	**15.8± 1.4**	**1.5 ± 0.9**	**-74 ± 10**	
Gwal Pahari (28.43° N, 77.15° E)	9.0 ± 1.5	10.6 ± 1.8	1.5 ± 0.7	-33 ± 6	Voudouri et al. (2020)
Elandsfontein (26.25° S, 29.43° E)	9.2 ± 0.8	10.8 ± 0.9	1.6 ± 0.7	-34 ± 5	
Chung-Li (24.58° N, 121.10° E)	12.3 ± 2.2	14.4 ± 1.7	1.5 ± 0.7	-	Das, Chiang, and Nee (2009)
Gadanki (13.5° N, 79.2° E)	13.0 ± 2.2	15.3 ± 2.0	2.3 ± 1.3	-65 ± 12	Pandit et al. (2014)
Hululu (4.1° N, 73.3° E)	11.9 ± 1.6	13.7 ± 1.4	1.8 ± 1.0	-58 ± 11	Seifert et al. (2007)
Amazonia (2.9° S, 59.9° W)	12.9 ± 2.2	14.3 ± 1.9	1.4 ± 1.1	-60 ± 15	Gouveia et al. (2017)
Nauru Island (0.5° S, 166.9° E)	-	16.5 – 17.0	-	-	Comstock and Jakob (2004)
Tropics ± 30°	-	14.3 ± 1.7	0.6 ± 0.2	-66 ± 10	Martins, Noel, and Chepfer (2011)

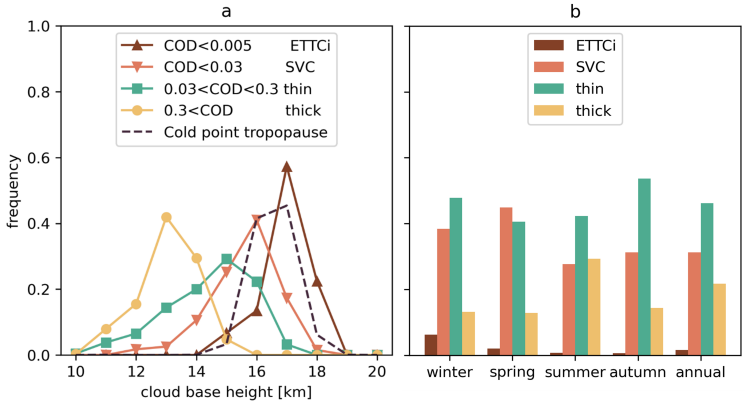

FIGURE 4.29: (a) Frequency of occurrence of the cloud base height with different COD as indicated by different colours and markers. The dashed line shows the distribution of the height of the CPT. (b) Seasonal and annual frequency of occurrence of the ETTCi, SVC, thin and thick cloud. Since the frequency of ETTCi is very low compared to several other clouds, it is difficult to see its exact frequency of occurrence in the figure; please see Table 4.2 for details of its value. Note that ETCCi (Immler et al., 2007) is a customized sub-classification of cirrus with an optical thickness defined as less than 0.005, which belongs to SVC. The sum of the fraction of SVC, Thin and Thick cirrus equals 1, which should not include the fraction of ETTCi.

in springtime time is highly related to the local atmospheric temperature anomalies and Madden–Julian Oscillation (MJO). The occurrence of the cirrus cloud was in phase with the MJO phase and the observations of clouds in the lower part of TTL (10 - 13 km) can be attributed to the convective activities locally (Virts and Wallace, 2014).

Previous studies based on satellite / ground-based Lidar focused on the tropic regions (e.g., Virts et al., 2010; Martins, Noel, and Chepfer, 2011; Cairo et al., 2021) have elucidated that seasonal variations in cirrus clouds in the TTL, specifically the lower part of it (10 - 13 km) are profoundly influenced by the changing monsoon seasons and relatively dry periods. This variation in convective activities in tropical regions is typically reflected by the ITCZ (Virts and Wallace, 2014; Virts and Wallace, 2010). Moreover, as mentioned in Section 4.1, the CE provides a more accurate picture of the interhemispheric exchange, i.e., the location of the convective zone (Sun et al., 2023). Our results of the optical properties, specifically CR, of the clouds also manifest a correlation between the convection zone and the cloud measurements. In summer (June-July-August), the CE is located in the latitude of Palau, (see Figure 4.18) indicating an enhancement of the convective clouds induced by the converging zone. During this period, the CR is significantly lower with an averaged value of 1.1 ± 0.1 (532/355 nm), see Figure 4.28 k-o and Table 4.2) than in other seasons and annual mean (1.6 ± 0.5, 532/355 nm). Combining our observations of cloud optical properties with the location of the CE, we verify that cirrus clouds have larger ice crystals and higher COD in the summer with lower CR (see Figure 4.28), which is more likely to originate from convective events. In contrast, in other seasons CE moves to the south of the Palau and is less influenced by large-scale convergence zones, and based on our radar measurements, cirrus CRs are larger and ice crystal particles smaller, and these high cirrus clouds are more likely to originate from in

situ dry freezes (Flury, Wu, and Read, 2012; Sassen, Wang, and Liu, 2008; Immler et al., 2007).

Satellite-based studies showing increased cirrus cloud PO in the TTL during NH winter (Zou et al., 2020; Sassen, Wang, and Liu, 2008). Zou et al. (2020) reported the cirrus clouds above the tropopause heights were detected in December-February with a frequency of 15% than June-August of 8% in the tropics (± 20 °). Besides, the Relative humidity with respect to ice (RHi) from the flight measurements over the TWP region showed the highest RHi over the TWP, and the associated persistent cirrus formation during the same period of the flight measurement (Schoeberl et al., 2019). They suggest that such high RHi in TTL during winter are associated with the adiabatic upward motion in this region and induced the ice cloud formation. Our measurements of cirrus clouds during winter are consistent with these previous results, with the coldest and highest cirrus cloud layer during winter. Moreover, the seasonal distribution of the vertical distribution of PO (Figure 4.25, DJF) suggests that cirrus clouds in winter are also most frequent close to the CPT (30-40% of the total observations of that season). Besides, compared with other sites in the tropical region(Table 4.3), Palau has higher CBH and CTH and the lowest cloud temperature. Such features of the thin and cold cirrus above Palau indicate that the occurrence of this cloud is related to the location where the pathway between the troposphere air into the stratosphere occurs.

As previous studies suggested, the SVC (see Section 2.2.3) is related to the dehydration of tropospheric air before it enters the stratosphere and is recognized as an implication for the air originating in the TTL and then entering the stratosphere (Jensen et al., 2010). From our measurements, COD of less than 0.1 accounted for 70% of the measurements. We detected some cirrus cloud layers with ETTCi layers of COD less than 0.005, adapted from the definition of Immler et al. (2007). The occurrence of the ETTCi accounts for 1.6% of the overall cirrus cases over Palau. We identified one peak of the mid-cloud height frequency for ETTCi, which is situated at 17 km, coinciding with that of CPT height. Although SVC is typically used to locate STE, our observations indicate that SVC is not concentrated at the CPT height above Palau but rather at 15 km which is much lower than the height of CPT about 16 to 18 km. Therefore, we suggest that ETTCi serves as a more reliable indicator for STE than SVC, given its consistent altitude with CPT.

4.4 Stratosphere-Troposphere Exchange over Tropical Western Pacific

This section describes the upper air transport and STE paths in the tropical cirrus cloud region through cloud measurements by Lidar and trajectory analyses by HYSPLIT (Lagrangian trajectory model, 3.4.2). The upper air paths of STE are highly correlated with the dehydration process of the upper air at the TTL, which is a prerequisite for cirrus cloud formation. The air slowly rising from the troposphere to the stratosphere is readily dried to saturation pressure over ice so the cirrus cloud with very low COD is formed by this process in the TTL region (Spichtinger et al., 2003; Jensen et al., 2005). This cloud formation mechanism described by the dehydration process suggests that horizontal advection rather than vertical motion of

the TTL would flow into a cold trap with very low temperatures (Holton and Gettelman, 2001), which leads to a dehydration process of the air in the region, which then rises adiabatically in the cold trap by the release of the latent heat (Schoeberl et al., 2019). In this section, the STE paths over the TWP in different seasons will first be determined in conjunction with the cirrus measurements and their trajectory analysis.

As discussed in section 4.1, the seasonal variations of the circulation system over the TWP are highly correlated with the movement of the CE, which will impact the origin of the low-level air masses over the TWP. The seasonal variations of the trace gas observations can be categorized by the CE, as discussed in Sect. Thus, in the TWP region, the TTL upper air transport paths, i.e., the STE channels, are given by observations of clouds and model simulations of their trajectories, and atmospheric transport in the free troposphere and boundary layer is given by observations of trace gases and simulations of CE. Linking the two, we investigate how seasonal variations in trace gas measurements affect the atmospheric composition of the stratosphere through different STE channels.

This section finalizes the combination of upper air paths in the TTL with lower air transport in the boundary layer and free troposphere and complements the classical four-path STE theory Figure 2.11 by incorporating seasonal differences. We further pointed out the mechanisms influencing the source and transport paths of air masses over the TWP region, i.e., the movement of the CE affects the lower air transport and the seasonal cycle of the minimum temperature in the cold trap related to the upper air pathways. Understanding the sources and transport paths of air masses over the TWP is crucial for unraveling the origin of atmospheric constituents in the global stratosphere.

4.4.1 STE and cloud measurement from Lidar

In order to understand the correlation between the cirrus clouds in TTL and STE path, the analysis combining the properties of the clouds and TTL features in different seasons is needed.

The TTL features which are shown by the height and temperature of CPT and LMS estimated from the radio soundings launched in Palau weather station (see Section 3.1) are given in Figure 4.30. The lowest height is around 16 km and the highest temperature is around 195 K of CPT, which occurs in the summer from June to August in Palau. In winter, the coldest CPT temperature approaches 185 k in December, January, and February. This specific lowermost temperature of CPT is important for the dehydration process of the optically thin cirrus in TWP. The height and temperature of LMS representing the lowest boundary of the TTL are shown in Figure 4.30 (b). It can be seen that the height and temperature of LMS have no clear seasonal variation compared to CPT. The height of LMS stays stable at about 11.6 km and a temperature of 347 K.

As mentioned in Section 4.3, Figure 4.29 a, the optically thinner clouds tend to stay in a higher altitude. The most frequent mid-cloud height of the ETTCi is at 18 km and even higher than the CPT. In order to analyze the details of the features of CPT and its relationship to the mid-cloud height in different seasons, the distance from the mid-cloud height of clouds grouped by their optical depth to the height CPT is

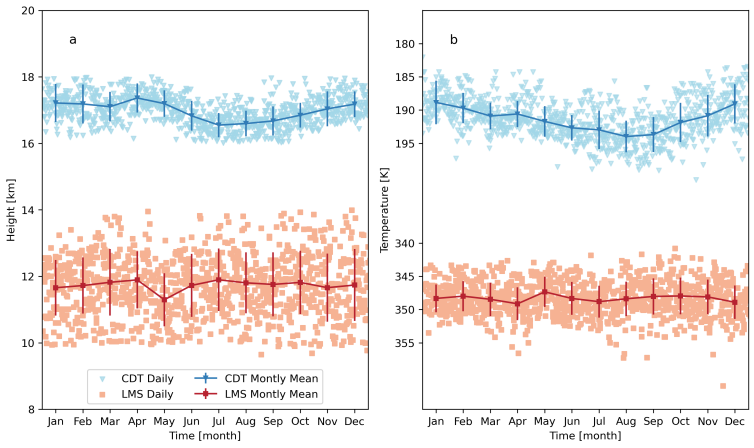

FIGURE 4.30: Daily and Monthly averaged (a) height (km) and (b) temperature (K) of CDT (red) and LMS (blue) during the COMCAL Lidar operation time in 2018, 2019 and 2022. Monthly mean and with 1- σ standard error of the data is shown by a red line and error bar, respectively. Daily data is shown by the square triangle and square for CDT and LMS, respectively. The meteorology profiles are from radio soundings by the Weather Service Office of Palau, see section 3.1.

calculated and shown in Figure 4.31. The height of CPT is calculated from the temperature profiles measured by radio soundings launched over Palau and matched to the date of the cloud measurements. The distance from CPT to the height of the mid-cloud layer is calculated by:

$$\begin{aligned} d_{Cirrus} &= H_{CPT} - H_{Mid-cloud}, \\ H_{Mid-cloud} &= (Cirrus_{base} + Cirrus_{top})/2 \end{aligned} \tag{4.10}$$

where d_{Cirrus} is the distance from CPT to the mid-cloud height of cirrus cloud layers measured by Lidar. The height of the mid-cloud height ($H_{Mid-cloud}$) is the average height of the cirrus cloud base and top derived from the same measurement time point. The CPT is calculated from temperature profiles obtained on the same day of the lidar measurement. For simplicity, for example, the distance from CPT to the mid-cloud height of different types of cirrus, e.g., SVC, thin, thick and ETTCi cirrus cloud refers to d_{SVC}, d_{thin}, d_{thick} and d_{ETTCi}, respectively.

The annual results of all cirrus distance indicates that most cirrus are distributed below 1 to 2 km of the CPT. For cirrus higher than CPT, the frequency is about 0.1 of the total cases, and the majority of those clouds that are higher than CPT are in the range of 1 km above the CPT. For thin cirrus, only a few cases that the cloud layers are higher than CPT, typically occur in winter and summer. The distributions of d_{thin} and d_{Cirrus} are similar to each other, which is not surprising since thin cirrus is the predominant type of cirrus cloud measured over Palau (see Figure 4.29b).

For thick cirrus, the most frequent d_{thick} is in the range of 3 to 4 km below the CPT about 13 to 14 km, which is typically the height of LNB and is also the height of LMCO (the level of main convective outflow, Section 2.2.2). This infers that the thick clouds measured above Palau are relative to the avail cirrus related to the outflow of the convective clouds. Moreover, there were no cases with thick clouds above the

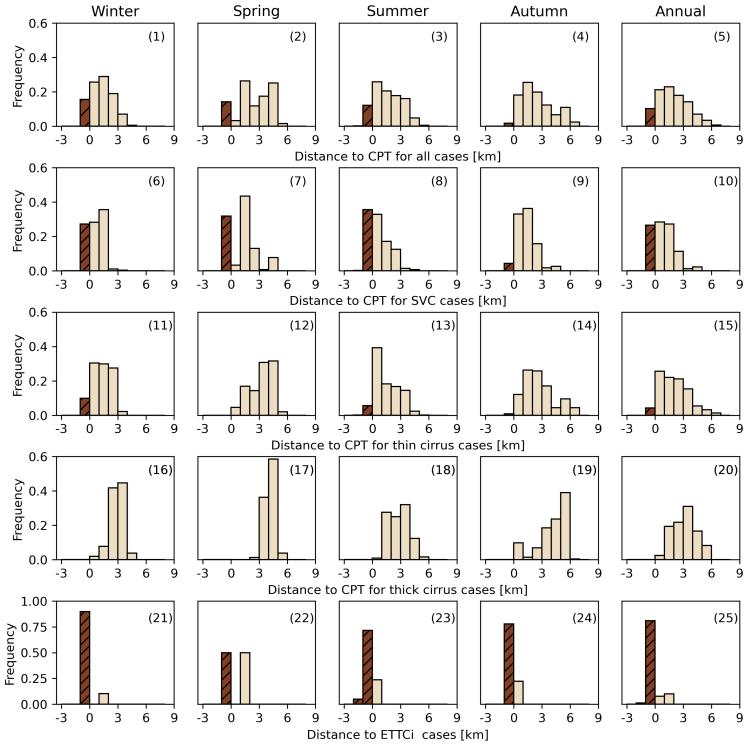

FIGURE 4.31: Frequency of occurrence of the seasonal and annual distance from the mid-cloud height for the cases of (1-5) all cirrus cloud (6-10) SVC (11-15) thin cirrus (16-20) thick cirrus and (21-25) ETTCi to the height of CPT. The bin size is 1 km. The bin is marked by the brown-hatched for the mid-cloud height higher than the height of CPT.

CPT. It indicates that for most cases, the highest altitude the convection cell can reach is LNB, and becomes equilibrium with the ambient atmosphere. This suggests that in most cases the highest altitude a convective cell can reach is the LNB, from which it flows out. Unless the air mass carrying detached ice crystals is further dehydrated at higher altitudes where the air is supersaturated and cirrus clouds with less COD, e.g., thin, SVC, and ETTCi cirrus clouds can be formed.

The ETTCi are the rare cases measured over Palau compared with other optically thicker cirrus. However, the ETTCi is very important because of its indication to the STE. In each season and annual mean, ETTCi is usually observed to be higher than CPT, with less than 25% of cases lower than CPT. In winter, About 90% of the cases in winter are with d_{ETTCi} of 1 km above CPT, which indicates the airmass transits into the stratosphere through the path in the cold trap above the TWP region in winter. Due to the exceptionally cold environment temperature in the upper TTL over Palau (can lower to 185 K, see Figure 4.30 b) during this period, the dehydration process in the air mass favours its slow and continuous rise. In this path, the formation of ETTCi occurs in parallel with the dehydration and slow rise of the air mass.

4.4.2 STE indicated by case studies of cirrus cloud

To study the cirrus in the upper troposphere above Palau in detail, typical two case studies of different types of cirrus are presented. To better understand the mechanism of the formation of the cloud layer, the profiles of temperature and RHi in the upper air on the same day of the lidar measurements are also presented and analyzed. The path of the STE is indicated by the cloud measurements from the lidar and the forward and backward trajectories of the clouds.

Typical case 1: 13 December 2018

The first case, on 13 December 2018 (Figure 4.32), shows a typical situation measured over Palau with two layers of clouds. During the measurement period, an SVC/ETTCi is detected at about 18 km, and one thin cirrus is detected at 14.5 to 16 km, as seen in Figure 4.32a. The COD of each cloud layer at the time point of the measurements is presented in Figure 4.32b.

The radio-sounding balloon was launched at 12:00 UTC, and Figure 4.32d presented the profiles of temperature. The height of the CPT is about 18 km, with a cold point temperature of about 185 K. The RHi calculated from the temperature and relative humidity obtained from the radio sounding are presented in Figure 4.32c. The RHi is increasing from about 14.5 km, where there is also the base of the lower cloud layer. The maximum RHi is about 140% at 18 km, which is the altitude of the SVC/ETTCi and the CPT. This supersaturated and cold environment near CPT suggests a condition that led to further dehydration of the air mass flow in the altitude range above 14 km up to the CPT. Throughout this process, cirrus clouds with very low COD were formed, such as the SVC and ETTCi. From the Lidar measurement over Palau, the SVC and ETTCi are typically detected in the range 2 km beneath and above the CPT (see Figure 4.31(6-10) and (21-25)), for example in this case 17.5 to 18.5 km on 13 December 2018.

The TTL over the TWP warm pool is the so-called "cold trap" (Holton and Gettelman, 2001) which plays an important role in the Stratosphere-troposphere Exchange (STE). As shown in Figure 2.9, the cold center in 100 hPa (about 16 km) is located above the TWP region in an annual mean map, and the coldest center is also located over the TWP region in January as shown by the white dashed line of the isothermal of 189 K in Figure 2.10. This also agrees with the temperature profiles measured over Palau on 13 December 2018, with a cold point of 185.2 K, as shown in Figure 4.32d. When the TTL air mass drifts horizontally through the large-scale circulation into a cold trap, the low-temperature conditions enable the air mass to further release latent heat and finally rise into the stratosphere.

In order to further analyze the path of STE with different cloud types on this day, the 30-day backward and forward trajectory for the upper and lower cloud layers are presented in Figure 4.32e-h. We started one trajectory each hour from 5 points inside the cloud. In detail, the releasing points are calculated from the cloud top and base height with the corresponding measurement time of the lidar. The cirrus clouds are vertically divided into four layers with five heights inside the cloud layer as the height of the starting points of the trajectories. The time step of the starting point of the cirrus cloud layer is 1 h.

For the backward trajectory of the upper cloud, the long-distance trajectories in the tropics are the dominant patterns. For several backward trajectories at a high altitude (17 km -19 km), there are circling patterns inside the cold traps. While for the lower cloud layer, most of the backward trajectories are from the long distance in lower altitudes less than 12 km.

From the forward trajectories, shown in Figure 4.32f and h, after the air parcel reaches the height of the upper cloud layer, which is about 18 km, only trajectories circling inside the cold trap over the TWP region ascend further and reach 20 km. The trajectory of the case for the upper cloud layer measured on 13 December 2018 coincides with Path 4 of classic STE pathways (see Figure 2.11), where the air parcels flowed long distances in the TTL until they reached the cold trap and circled in it, eventually reaching the stratosphere. As the air parcels exited the cold trap, they descended to lower altitudes of less than 17 km, circled and slowly descended in mid and lower altitudes (15 - 17 km) of TTL, and finally entered the troposphere. This transport mode refers to Path 2 of classic STE pathways (Figure 2.11), where the air mass flows within the TTL and descends outside the cold trap, eventually descending into the troposphere. For the forward trajectories of the lower cloud layer, the situation is similar to the upper cloud layer. Only inside the cold trap, the heights of the trajectories were higher than this cloud layer (>16 km), while trajectories outside it tend to stay at lower altitudes.

Typical case 2: 1 August 2022

Another case on 1 August 2022, is presented by Figure 4.33. During the measurement period, two layers of cirrus were detected, which is similar to the case on 13 December 2018. The lower cloud layer stays at about 14 km with a GT of 1 km, and most of the COD of the lower cloud layer is higher than 0.1 and even higher than 0.3, namely thin and thick cirrus, respecively. The upper cloud layer stays below the CPT of about 17.5 km during the measurement time, as shown in Figure 4.33d. The COD of this layer was less than 0.03 and even less than 0.005 at specific measurement time points. So the upper layer cloud is the SVC and ETTCi, which is very similar to the first case on 13 December 2018.

The temperature and RHi are presented in Figure 4.33 c and d. The RHi was less than 100% in the whole vertical range from 10 km to 20 km, which shows the relatively dryer environment than the winter case on 13 December. Even below the height of cloud bases of both cloud layers, the environment was less than 100%. The cold point in this case was about 190 K which is higher than the winter case, indicating the less intensive cold trap over TWP. The lower RHi below the CPT indicates that the cold trap during this time is not cold enough to further dehydrate the air parcels flowing in it.

The trajectory results for this case are also presented. The backward trajectory of the upper cloud layer shows a stable circling pattern above 19 km in the NH inner tropical regions (10 °N) and a lower descending pattern in the SH. This suggests the large-scale descending air mass in the UTLS for the summer case in contrast with the ascending air mass below the CPT shown by the winter case.

From the forward trajectories, almost all the air masses descended from the cloud layer height of about 18 km to a lower altitude of less than 16 km. The results of the trajectories and measurements on 1st August 2022 suggest that even though

the SVC and ETTCi were formed near the CPT in the low-temperature layer, they would disappear later because of the less intensive cold trap and the associated non-supersaturated environment. The air parcels in this upper cloud layer slowly descended and finally entered the troposphere. This transport mode refers to Path 2 of classic STE pathways (Figure 2.11), where the air mass flows within the TTL and descends because of the less intensive cold trap over the TWP region, eventually descending into the troposphere.

For the lower cloud layer, most of the backward trajectories are from the long distance in lower altitudes less than 12 km similar to the winter case. The forward trajectories of the lower cloud layer show that air parcels descended to altitudes lower than the cloud height (< 14 km). This transport pattern of the lower cloud layer is Path 2 and 3 of classic STE pathways (Figure 2.11). Before the air parcel reached LNB/EL about 14 km the latent heat of the parcels was fully released and generated widespread anvils at this altitude. The temperature is very low and the freezing of the liquid droplets forms long-lived cirrus as the cloud layers detected by the lidar measurements in this case. After that, the air parcels flowed through the TTL region and eventually descended to low altitudes.

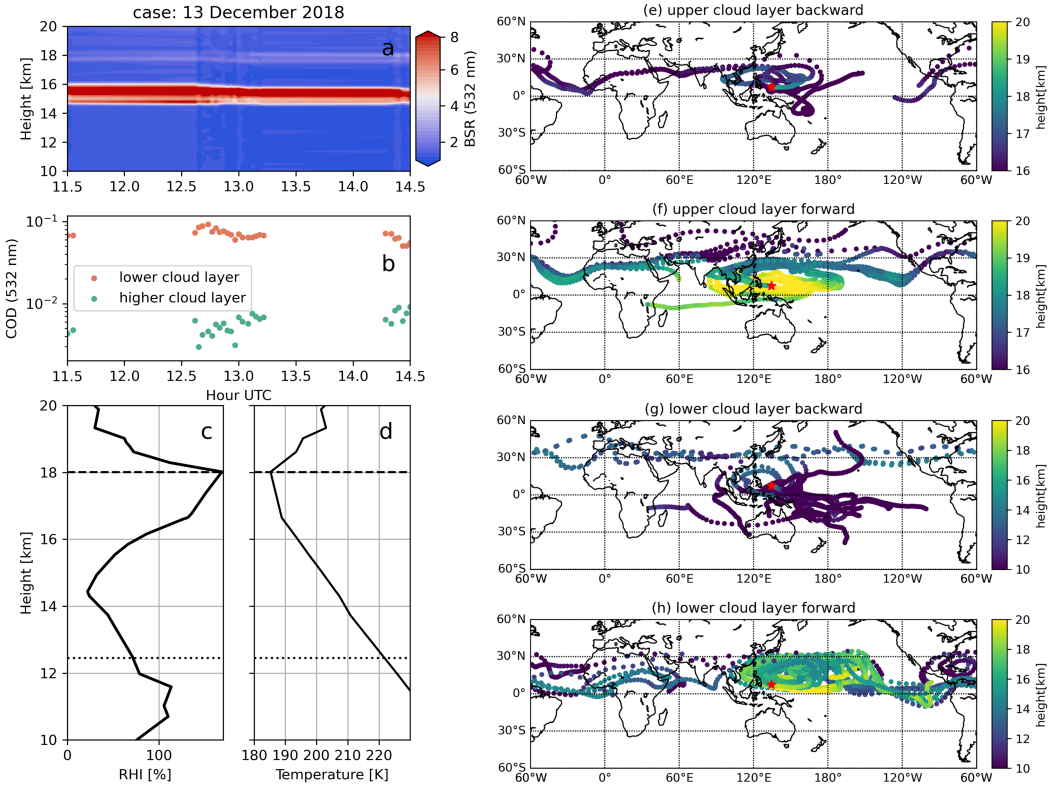

FIGURE 4.32: Measurements and trajectory analysis of a typical case study on 13 December 2018. Figure 4.32a shows the BSR at 532 nm as a function of time and altitude. Figure 4.32b are the COD at 532 nm of the cloud layers as a function of time corresponding to Figure 4.32a. Two cloud layers are detected on this day, the COD of the upper layer and the lower layer is marked by green and red dots, respectively. Figure 4.32c shows the RHi profiles as a function of height. Figure 4.32d shows the temperature profiles as a function of height. The temperature and RHi profiles are obtained from the radio soundings launched at the Palau weather station (see Section 3.1). The horizontal lines indicate the altitude range of the TTL between the CPT height (dashed line) and the height of LMS (dotted line) calculated by the temperature profiles each day. Figure 4.32e - h displays the trajectories of the cloud layer corresponding to Figure 4.32a. Figure 4.32 e and g display the backward trajectories while f and h display the forward trajectories, respectively, for the upper (e and f) and lower cloud layer (g and h). The colors of the scatter in the trajectory plot depict the height of the trajectory points. To see the set-up of the trajectory model, please refer to Section 3.4.2. RHi: the Relative Humidity with respect to ice.

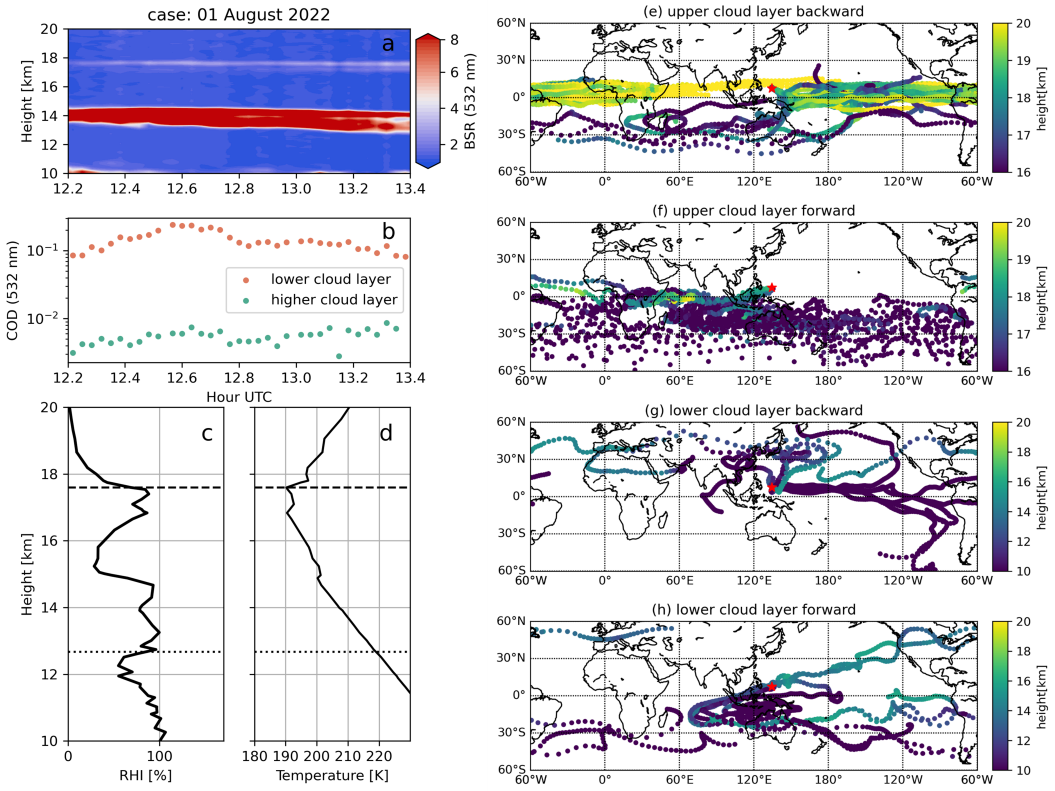

FIGURE 4.33: Measurements and trajectory analysis of a typical case study on 1 August 2022. The description of the plots is the same as Figure 4.33 but for a different day on 1 August 2022.

TABLE 4.4: Information of the case studies

	Case 13 December 2018	**Case 01 August 2022**
Height of CPT [km]	18.0	17.5
Temperature of CPT [K]	185.2	190.2
Cloud types (upper)	SVC, ETTCi	SVC, ETTCi
Cloud types (lower)	thin	thin, thick
Pathway	Path 2 and 4	Path 2 and 3

4.4.3 Pathway of STE from trajectory analysis

Based on the analysis of the trajectory simulation by the HYSPLIT trajectory model, the pathways of STE in winter and summer are compared and presented. The trajectories were released from the cirrus cloud layer in TTL by the lidar measurements on all available months. The setup and details for the trajectory model simulation are described in Section 3.4.2. Here, the results of trajectories in August and December, which are the most representative months for winter and summer are presented and discussed in detail.

Source of the air masses in TTL over Palau

The start of the trajectory is divided into two layers, 12 - 16 km and above 16 km, which represent cirrus clouds measured at the lower and upper levels of the TTL. For simplicity, the trajectories released from 12 - 16 km are referred to as $Traj_{low}$ and those above 16 km are referred to as $Traj_{up}$.

In December, most of the air masses in $Traj_{up}$ come from the lower levels of the TTL (< 16 km), as seen from Figure 4.34 a. This suggests that for cirrus clouds staying in the upper layers of the TTL, they are formed by gradual dehydration in the rising air mass. Compared to $Traj_{up}$, more $Traj_{low}$ are higher than the height of the start point and coming from long-distance transport. But the dominant trajectories are still lower than the start point which indicates a mostly ascending process.

In August, $Traj_{up}$ and $Traj_{low}$ have similar characteristics. In the tropics ($\pm 30^{\circ}$) air masses come from higher altitudes relative to the starting point. This suggests that over the summer tropics, the air masses originate mostly from downwelling transport over the NH tropical at the TTL. In terms of the large-scale circulation system, this is consistent with the characteristics of the upper down-welling branch of the Hadley cell, with cold air sinking at the TTL on a large scale. Both $Traj_{up}$ and $Traj_{low}$ are at lower altitudes in the extratropics. In the NH subtropics (30° N - 60° N), there are lower tropopause heights and associated higher ambient temperatures in the upper troposphere atmosphere. So there is a large-scale upward process of air masses from the subtropics into the tropics, i.e., the upper branch of the Ferrel cell.

In summary, the source of the air masses over the TWP region in TTL is different between summer and winter. In winter, the air masses are coming from the lower altitude with large-scale up-welling. In contrast, for summer, the air masses sources are dominated by the large-scale downwelling transport in tropical regions and up-welling from sub-tropical long-distance transport.

Pathway of STE in TTL over Palau

The forward trajectory simulations of the cloud layers were conducted to understand the forward path of the air masses in the TTL. The simulation results for December and August are presented in Figure 4.34e-f. The releasing points of the trajectories were also divided into the upper and lower layers similar to the backward analysis.

In December, most of the air masses that can continue to rise to higher altitudes are located within the confines of the cold trap, which is the cold temperature center over the TWP region in winter (shown in Figure 4.34i). For $Traj_{up}$, higher air masses further descend into lower altitudes out of the cold trap in the tropical region and subtropics within the 30-day time span of the trajectory. For $Traj_{low}$, the results show that most of the air masses stay inside the cold trap and slowly ascend for at least 30 days.

In August, the forward paths of the air masses mostly descend to a lower altitude. Most of the trajectory in August will sink into the SH tropics. Some of the trajectories in the equatorial Indian Ocean will continue to rise. A few of the $Traj_{up}$ may even rise to heights greater than 20 km, which enters the stratosphere similar to the winter season. However, the proportion of trajectories that continue to rise is much smaller

than in winter. This suggests that in the upper TTL, the STE path over the TWP through very low temperatures into the stratosphere is still dominant due to the effect of cold traps.

The temperature over the TWP region in 100 hPa is presented in Figure 4.34i and j. There is a cold center with the lowest temperature which refers to the cold trap located over the TWP region both in December and August. The lowest temperature of about 189 K in December is also located over TWP, and as mentioned before, only forward trajectories inside the cold trap can uplift and reach the stratosphere. In August, the cold center moves westward and spreads out over the North Indian Ocean. This is also consistent with the results of the summer forward trajectory simulation.

Overall, the results of air trajectories over the TWP show seasonally characterized transport pathways. The seasonal characteristics of the transport paths are closely related to the upper layer temperature of the TTL in the corresponding season and the location of the minimum temperature of the cold trap. In summer, the trajectories of the air masses are consistent with a large-scale circulation background. They are controlled by the upper branch of the Hadley circulation in the TTL, showing a transport path of large-scale cold air sinking. In winter, on the other hand, the air masses show a large-scale slowly ascending transport path in the cold trap, influenced by the very low temperature in the upper TTL. For the air masses flow outside the cold trap, they are consistent with the sinking path of the Hadley circulation in the upper layer of TTL.

The previous analysis was based on the backward and forward trajectories released in December and August which represent winter and summer, respectively. For trajectory simulations by HYSPLIT on other months, please see Appendix B.3.

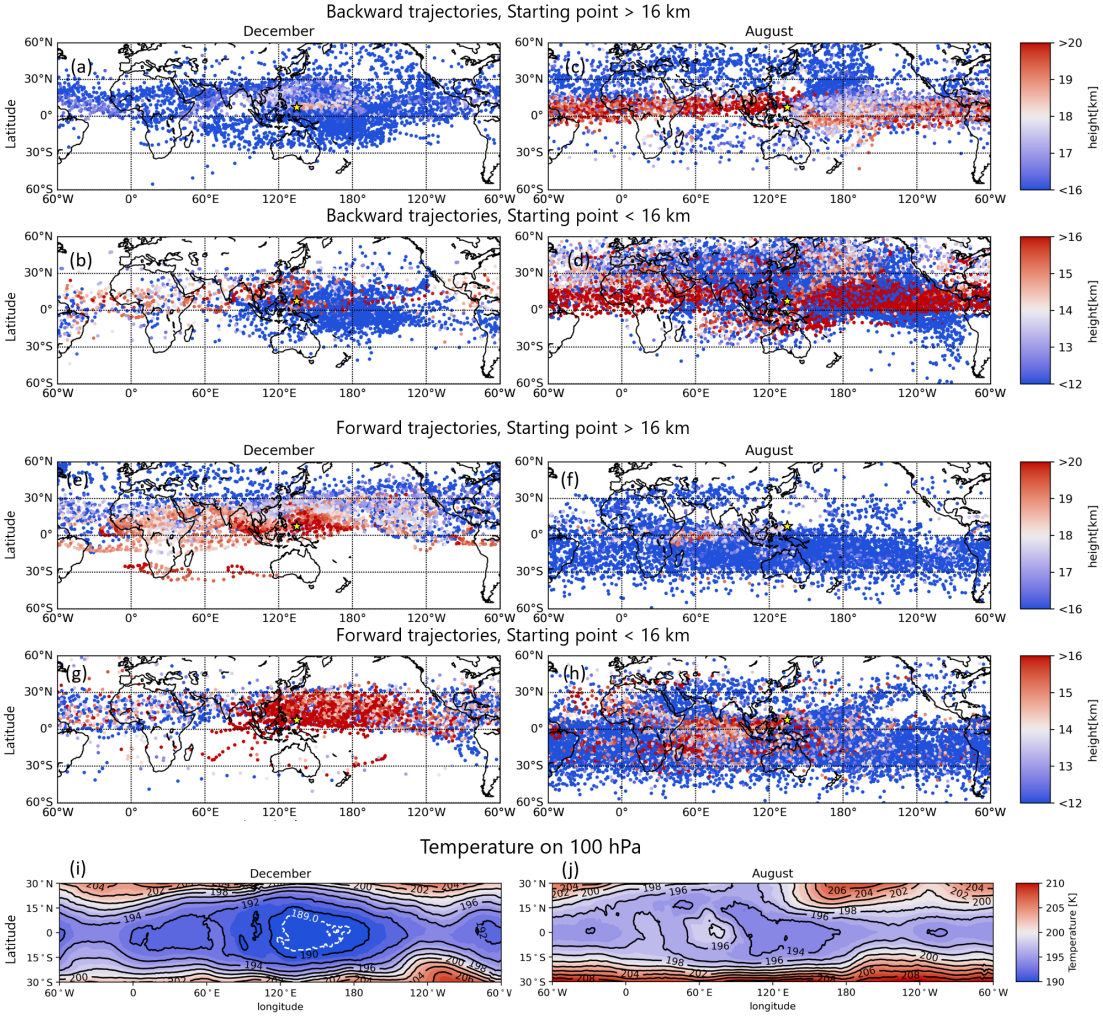

FIGURE 4.34: 30-days (a)-(d) backward and (e)-(h) forward trajectory starting from the cloud layer and maps on 100 hPa of (i) December and (j) August averaged temperature (in K) fields. The height of the start point is divided into two groups: 12 - 16 km and higher than 16 km, as noted on the plots, Figure4.34(a), (c), (e) and (i) are trajectory groups with starting point higher than 16 km; Figure4.34(b), (d), (g) and (h) are trajectory groups with starting point higher than 16 km. The location of Palau which is the start point of the trajectory is marked by the yellow markers in the figure. Trajectory points are output at hourly intervals, and in Figure4.34(a)-(d) and (e)-(h), the trajectory points are sparsified at intervals of 20 points for clarity of display. The white dashed line shows the isothermal line of 189 K in December. The temperature data are from the ERA5 reanalysis data (Hersbach et al., 2020).

4.4.4 Summary and discussion

In this section, the transport paths of the TTL over the TWP area are analyzed by combining cirrus lidar measurements and trajectory model simulations. The principle finding is that only cirrus cloud layers measured in winter have forward trajectories further up into the stratosphere, providing observational support to the long-standing assumption in trajectory models that the primary path of the STE is over the winter TWP region. (Fueglistaler, Wernli, and Peter, 2004; Fueglistaler and Fu, 2006; Bergman et al., 2012b).

We first compare distances from the CPT to the mid-cloud height for different types of cirrus clouds. Although the SVC is usually taken as the indicator of the STE in the upper TTL (Reverdy et al., 2012), we found that the most dominant height of SVC is about 16 km (Figure 4.29) and evenly distributed 1 - 3 below the CPT (Figure 4.31 (6)-(10)). This suggests that the SVC is not a good indicator of STE processes for air masses. We suggest optically thinner cirrus cloud with COD less than 0.005, the ETTCi (Immler et al., 2007) to better indicate the relationship between the STE process and the cirrus cloud. This cloud is dominantly distributed 1 km above the CPT (Figure 4.31) which suggests a possible better indicator of STE than SVC.

With two typical cases measured in different seasons, we combine meteorological conditions, measurements of cirrus clouds in the TTL and their trajectory simulation results. Our measurements provide a demonstration for the classical four transport paths of STE (see Section 2.3, Figure 2.11, Fueglistaler, Wernli, and Peter, 2004; Bergman et al., 2012a) in the TWP region. The characteristics of cirrus clouds, such as the altitude at which they are located, and the geometric and optical thickness of the clouds are very similar in both seasons. However, the meteorological conditions are different, with supersaturation just reaching the clouds in summer. In winter, the humidity is much higher and much greater than the supersaturation compared to the summer season case. Combining the results of the trajectory simulations for both, it is found that the air mass at the height of the cloud in winter rises further due to dehydration, and the upper-level cloud can even reach the stratosphere. In contrast, air masses in summer descend after reaching the CPT and do not reach the stratosphere.

The Backward and forward trajectory simulations are performed based on cloud measurements to study the upper-air transport path and its seasonal characteristics. The summer trajectory results show that the vast majority of the sources and destinations of air masses are consistent with a large-scale circulation in the TTL. Large-scale cold air sinks in the upper down-welling branch of the Hadley circulation close to the CPT over the tropical regions. Only a small fraction of the air masses over the northern Indian Ocean are able to enter the stratosphere. In winter, it is distinguished from the sinking transport path of cold air in the upper branch of the Hadley circulation. Due to the presence of cold traps, large-scale updrafts replace the cold-air sinking circulation background. Air masses in the cold trap can rise further into the stratosphere. In conjunction with the 100 hPa temperature field, the location of the cold trap is consistent with the region of the large-scale rising air mass.

By cloud layer measurements and trajectory simulations, we demonstrate the four transport paths of upper air over the TWP in different seasons. In the previous sections, through model simulations and observations, we used CE to obtain the source and seasonal variation of the bottom layer of air masses in the troposphere

over the TWP region. Combining the transport paths in the lower troposphere and upper air, we give the complete transport path over the TWP considering seasonal characteristics, as shown in Figure 4.35. The four transport paths over the TWP region are shown by the arrows, with different cloud types, such as convection cells, thin cirrus, SVC, associated with different transport paths. In summer, there is only one path where air mass can reach the stratosphere over the TWP region, the overshooting tops penetrating the TTL, which refers to Path 1. The STE by overshooting tops occur randomly in all seasons, and (Fueglistaler et al., 2009; Pommereau, 2010). The airmass outflows from the convection cloud and avail-shaped cirrus clouds are formed. The air mass outflows from it in LNB or in the upper layer of TTL and finally sinks to the free troposphere for Path 2 and Path 3. The typical altitude of a convection cloud over a tropical region is the LNB / EL, at about 14 km as shown by Path 2 in Figure 4.35. Cloud measurements also show high frequency of the thick clouds below 14 km in TTL over Palau. Path 2 happens when the outflow of the convection is over LNB, thus the air mass circulates longer time in the upper layer of TTL than Path 3 (Bergman et al., 2012a; Takahashi, Luo, and Stephens, 2017).

However, Path 4 only occurs in winter, associated with the strong cold trap during this time, depicted by the upper yellow ellipses over the TWP region, as shown in 4.35b. As mentioned before, the low temperature near CPT over the TWP region favours the dehydration process of the air mass. The SVC and ETTCi cloud are usually detected near the CPT (Immler et al., 2007; Pandit et al., 2015). Our trajectory simulations show the large-scale uplift in the cold trap in winter replaces the cold-air sinking circulation in the down-welling branch of the Hadley cell in other seasons. This is consistent with the cold trap scheme from the previous studies (Holton and Gettelman, 2001; Fueglistaler, Wernli, and Peter, 2004; Fueglistaler et al., 2009; Bergman et al., 2012b).

Moreover, the air mass origins are shown by the blue/red circles at the beginning of the arrows. The blue and red curves and the two blue arrows in the lower part of the figure show the location of the CE, which is centered on (a) the 10 °N in summer and (b) the 10 °S in winter (for details on the vertical structure of the CE, see Figure 4.9). The blue and red circles in the figure indicate the continental airflow from NH (Southeast Asia) and the clean ocean airflow from SH (Pacific Ocean), respectively.

Controlled by the north-south movement of the CE in different seasons, the dominant air mass origins are different. The clean air from SH blows to Palau in summer, through different transport paths into TTL. The short-lived species from the ocean such as Br_y and I_y can be injected into the stratosphere through Path 1 by the intensive overshooting tops. In contrast, the NH, specifically, Southeast Asia, are the dominant air mass origins over the TWP region in winter, bringing high content of species related to human activities, such as O_3, CO and NOx. This is characterized by the FTIR and the ozone sonde measurements in Section 4.2. The air mass from Southeast Asia then via the vertical transport path into TTL. As mentioned in Section 2.3.2, there are low values of OH and O_3 thus low oxidizing capacity in the TWP region, especially in cold traps, (see Figure2.13). Thus, Path 4 with a high possibility to transport the short-lived species into the stratosphere before such species are oxidized and removed in the air. This scheme of Path 4 over the TWP region in winter has a large impact on the atmospheric composition in the stratosphere and finally impacts the global climate. However, further quantifying the short-lived species by direct measurements such as aircraft and satellites over the TWP region in the cold trap is needed to further validate this process.

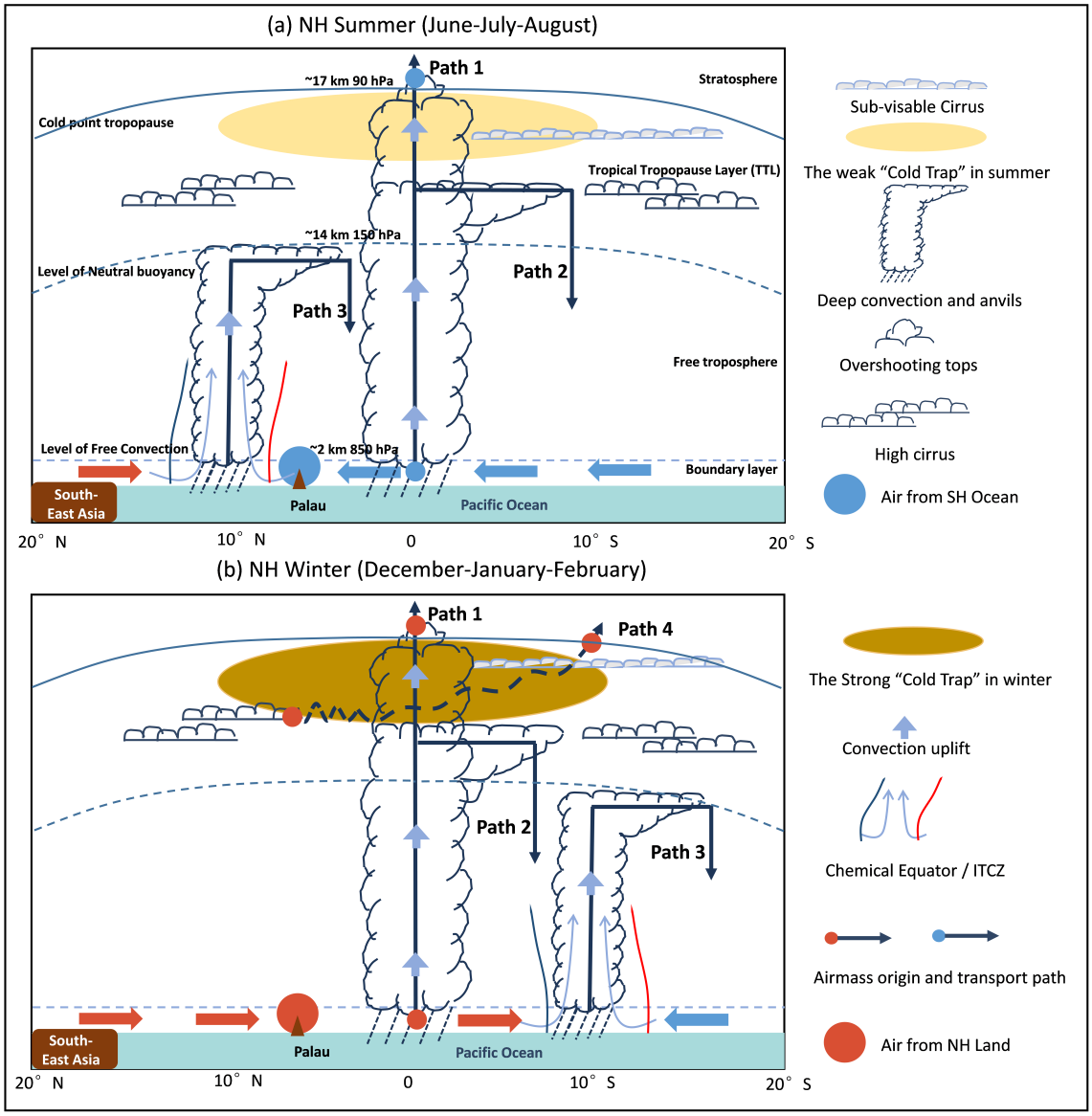

FIGURE 4.35: Schematic diagram of transport and paths over the TWP region associated with the longitudinal seasonal transitions of the circulation systems (ITCZ/CE) and the resulting changes in the sources of air masses in the (a) summer (June-July-August) and (b) winter (December-January-February). The descriptions of the icon are given on the right of the Figure. The transport and paths over the TWP are supplemented with seasonal variations in their characteristics from Figure 2.11.

Chapter 5

Summary and outlook

5.1 Summary

The major pathway for air entering the stratosphere is over the Tropical Western Pacific (TWP) region (Fueglistaler, Wernli, and Peter, 2004; Bergman et al., 2012a), and this key region have a major effect on modifying the atmospheric composition in the stratosphere (Rex et al., 2014; Villamayor et al., 2023). The model simulations and measurements from the atmospheric observatory located in Koror, Palau (7.34°N, 134.47°E), in the center of the Pacific warm pool, are used to study the transport paths over this key region. The objective of my PhD is to study the pathways of STE over the TWP region and exploit the usage of FTIR and ground-based Lidar measurements for this topic.

The atmospheric transport in the TWP region is highly related to the movement of the circulation system, the Inter-Tropical Convergence Zone (ITCZ) associated with the up-welling branch of Hadley cell in the tropics (Adam, Bischoff, and Schneider, 2016; Berry and Reeder, 2014). Since the indicator of ITCZ such as tropical rain belt is not accurate enough in the TWP region (Schneider, Bischoff, and Haug, 2014), we developed a method called Chemical Equator (CE) by the simulations of an artificial passive tracer to indicate the migration of atmospheric circulation systems and air mass origins. We compared CE with the tropical rain belt, a common indicator for airmass origins from ITCZ theory, we found that CE is not always consistent with the maximum rain rate during the year, especially in the TWP region.

Then, seasonal variations in tropospheric columns of CO and ozone measured by FTIR spectroscopy and ozone sondes were characterized using CE. The low CO and O_3 are in summer and early autumn and high CO and O_3 in winter and early spring can be characterized by the seasonal north-south movement of the CE. Thus, the effects of transport on the atmospheric composition in the troposphere over the TWP region were verified with observations and model results. These results suggest that CE has a good potential to be utilized to distinguish between different origins of air masses influenced by atmospheric large-scale circulation factors.

The upper-air observations were conducted for the cirrus cloud layers by ground-based polarization Lidar. The occurrence of the cirrus clouds and their geometrical, thermodynamic and optical properties were quantified and analysed. The annual

cycle of the cloud layer height and cloud temperature is consistent with the Cold Point Tropopause (CPT), with maximum cloud layer height, highest CPT in winter and minimum cloud layer, lowest CPT in summer. The measurements show that the cirrus clouds observed in Palau are colder compared with other places in the tropics. The high occurrence of the colder cirrus cloud layer coincides with the phenomenon that there is a colder temperature closely below the CPT compared with everywhere else in the tropics.

To relate the atmospheric transport in the Upper troposphere and Lower Stratosphere (UTLS) region to the measurements of the cloud layer, we conducted Lagrangian trajectory simulations based on the cloud layer measurements. Considering the seasonal cycle of the CPT over the TWP region, the cloud layers measured and the trajectory simulations in winter and summer were compared. The principle finding is that only cirrus cloud layers measured in winter have forward trajectories further up into the stratosphere, lending observational support to the long-standing assumption in trajectory models that the primary path of the STE is over the winter TWP region (Fueglistaler, Wernli, and Peter, 2004; Fueglistaler and Fu, 2006; Bergman et al., 2012a). Combining trajectory results and the temperature fields, it indicated that due to the presence of a cold trap (Holton et al., 1995; Holton and Gettelman, 2001) in winter. This is an exceptionally cold center over the TWP upper layer near CPT, large-scale updrafts replace the cold-air sinking circulation background which is the down-welling branch of the Hadley cell.

Finally, we provide an atmospheric transport scheme over the TWP region combining measurements in Palau and model simulations. In the lower altitude from surface to free troposphere, it is characterized by the north-south movement of CE, and its position associated with the air mass origin can be determined by the simulation of the passive tracer. In the UTLS region above TWP, the measurements of cloud layers and the trajectories validate the pathways of the stratosphere-troposphere exchange. The clean air from the Pacific Ocean blows to Palau in summer, and the short-lived species from the ocean such as Bry and Iy can be injected into the stratosphere through the overshooting tops which rarely penetrate into the stratosphere (frequency about 0.5% over the TWP (Pommereau, 2010)). In contrast, Southeast Asia, has the dominant air mass origins over the TWP region in winter, bringing high content of anthropogenic species, such as O_3, CO and NOx. The air mass from Southeast Asia then via the vertical transport path inside the cold trap into the stratosphere.

5.2 Outlook

Although there are gaps and uncertainties in the measurements of such short-lived species and anthropogenic species over the TWP region, specifically in the cold trap, the atmospheric transport scheme can still be supported by the model simulations and the cloud layer measurements in the upper air over Palau. Considering the vertical resolution of the FTIR measurements of such species, future work can focus on satellite-based measurements over the TWP region, and lend more observational support to the theory of the pathways from the troposphere to the stratosphere.

There has been an ongoing debate about whether the short-lived species can be transported into the stratosphere through the cold trap scheme (Fueglistaler and Fu, 2006; Pommereau, 2010). The time scale of the cold trap scheme is as long as 60 days. The assumption and explanation for this is the low oxidizing capacity associated with low OH content in the atmosphere over the TWP region, especially in the cold trap (Rex et al., 2014). The species can stay longer in the atmosphere before being oxidized and removed. However, there have been no direct estimations of the OH content in the atmosphere, and it is only based on the model simulation. Although challenging, the direct estimations of the OH and the related low oxidizing capacity are the key to the cold trap scheme of STE.

The seasonal cycle of the transport scheme over the TWP region is based on the general atmosphere circulation systems. However, equatorial climate variation, for example, El Niño and La Niña, is of great importance in understanding the atmosphere transport process. Future work about the transport scheme over the TWP region considering the equatorial climate variations is needed.

In the context of global warming, a number of recent studies have reported that cold traps in the tropics (e.g. Pandit et al., 2015; Bourguet and Linz, 2023) have become weaker and that the UTLS O_3 has also become impoverished due to an increase in short-lived species (Villamayor et al., 2023). While there is now more discussion and partial confirmation of the former, the implications of the weakening cold trap for STE have not received sufficient attention. At the same time, changes in the STE pathway also bring about effects on the stratospheric chemical composition. So the question of whether this is related to the depletion of the tropical stratospheric ozone layer and to what extent it will affect the global climate also needs to be answered.

Appendix A

Additional Description of Model Simulation

A.1 Sensitivity study for CE: Experiment 3 to Experiment 5

E3 to E5 are three supplement case studies with different emission regions and vertical layers compared to E1 and E2; the setting of the simulations are shown in Table. A.1. These cases are aimed to test the stability of our method to determine the CE. It should be noted that the north-south gradient of this passive tracer is the initial condition of the method and the definition of the CE. So, the emissions of the tracer must exist continuously in one hemisphere to create and maintain this gradient, rather than an equilibrated atmosphere.

A.2 CE by Gradient Method

The CE calculated from the latitudinal gradient of the passive tracer is shown in Fig. A.1. In some regions, such as Easter Pacific and Atlantic Ocean, the gradient-based CE is consistent with the CE calculated by the trend as the method used in the main text of the study. But in general, the gradient-based CE is less stable than the trend-based CE in most areas, which shows a better potential to use the method based on trend to determine the CE than by the gradient. In some cases, e.g. Fig. A.1b between -130 and -160 °E the gradient found by the steepest gradient does not make sense.

TABLE A.1: The settings for experiment E3 to experiment E5

Experiment	Release area	Release layer	Simulated time
E3	30°N - 70°N, -180°- 180°	Surface - 1 km	5 years (2014 - 2019)
E4	30°N - 90°N, -180°- 180°	Surface - 10 km	5 years (2014 - 2019)
E5	30°N - 90°N, -180°- 180°	Surface - 1 km	5 years (2010 - 2015)

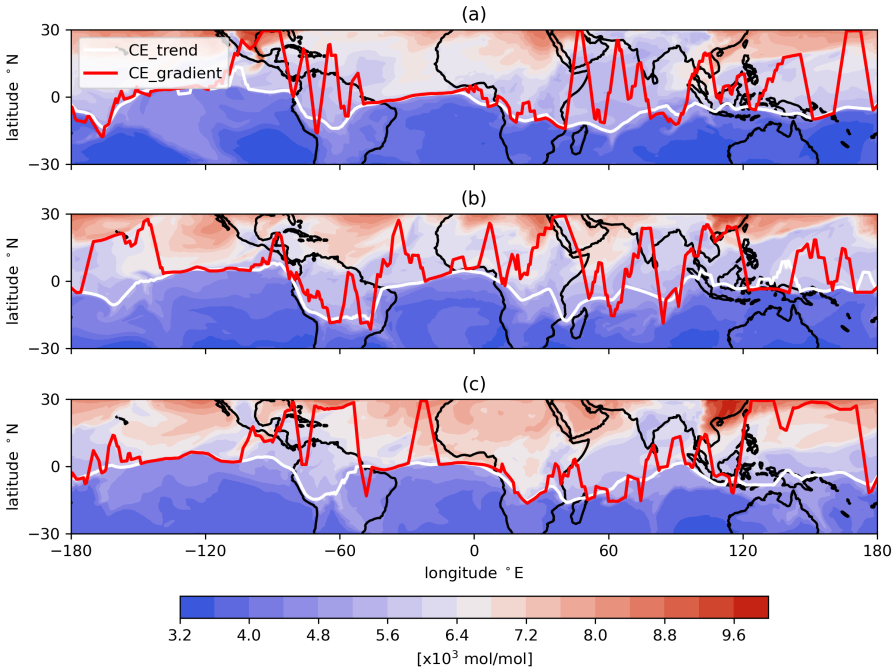

FIGURE A.1: The CE which is calculated by the trend (CE_{trend}, solid black line) compares to the CE which is calculated by the latitudinal gradient of the passive tracer ($CE_{gradient}$, dashed dot line). The upper, middle, and lower plots are CE with the distribution of the passive tracer on 1, 15, and 31 January 2016.

Appendix B

Additional Description of Measurements and Results

B.1 CH_4 and CO Products from TROPOMI

The Sentinel-5 Precursor satellite mission (Veefkind et al., 2012) was launched on 13 October 2017 carrying a single scientific instrument, TROPOMI, which is a nadir-viewing passive grating imaging spectrometer. The satellite is positioned in a near-polar, sun-synchronous orbit and has a swath width of 2600 km, which allows for daily coverage of the Earth. The retrieval is however dependent on sun-lit, cloud-free scenes which limits the daily coverage. The instrument consists of four spectrometers measuring radiances in the ultraviolet, ultraviolet-visible, near-infrared, and short-wave infrared bands. XCH_4 and XCO used in this study are retrieved from TROPOMI measurements of sunlight reflected by Earth's surface and the atmosphere in the SWIR wavelengths (2300 - 2389 nm). The spatial resolution is 5.5 × 7 km^2 at nadir. The Weighting Function Modified Differential Optical Absorption Spectroscopy (WFMD) TROPOMI data product (Schneising et al., 2019) provides column-averaged dry air mole fractions of both CH_4 and CO. Here we use the latest release of the WFMD product (v1.8) (Schneising et al., 2023) and process it onto a 2° × 2° grid. For this, each measurement is assigned to a single grid cell and the weighted average of all measurements per cell is calculated. The measurements are weighted using the inverse standard deviation to disadvantage measurements with high uncertainty. Additionally, only measurements with a quality flag (qf) and qf=0 (good) are included. Data coverage is therefore limited over regions with many clouds (e.g. tropics) or challenging measurement conditions.

B.2 The measurement hours of the Lidar system

The measurement hours of the lidar system and the time of the cirrus cloud occurrence in each month are shown in Figure A. The total duration hours of the lidar

system were 332 hours during the period 2018 to 2022. Cirrus cloud layers are being detected each month. The time of the occurrence of the cirrus cloud is also shown each month with the total duration time of the lidar system. There were no successful measurements by ComCAL in June and September because of the technique issues.

It should be noted that the uncertainty of the yearly averaged PO can be due to the gap between our observations and the uneven duration time of the lidar each month. We have a specifically long duration time of Lidar in August, as shown in Fig. B.1 since we made an intensive measurement during the Asian Summer Monsoon Chemical & CLimate Impact Project (ACCLIP) campaign in August 2022. Apart from that, the other months are with a similar range of duration time. Even though the duration time in July and August is very different, the PO with 44% in July and 47.7% in August is within the acceptable difference in the same season. This gives us confidence that a longer duration time does not introduce large uncertainty.

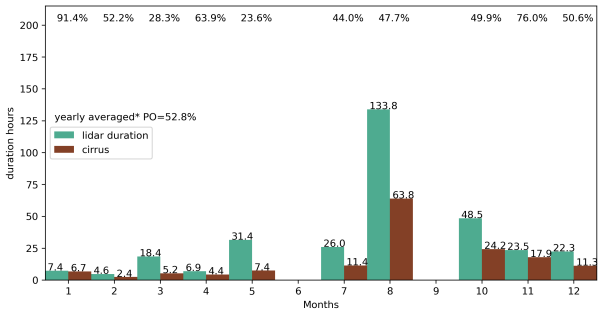

FIGURE B.1: Monthly measurement hours of the lidar system and cirrus cloud occurrence in Palau. The number in the upper plot refers to the average PO of cirrus out of the total duration time of the lidar system in each month. *The yearly averaged PO is calculated within the 10 months we had observations.

B.3 HYSPLIT trajectory simulations

The backward and forward trajectory simulations of the cloud layers were conducted to understand the forward path of the air masses in the TTL. The simulation results for other months as a supplement of Figure 4.34 are presented in Figure B.2 and Figure B.3, respectively. The start of the trajectory is divided into two layers, 12 - 16 km and above 16 km, which represent cirrus clouds measured at the lower and upper levels of the TTL.

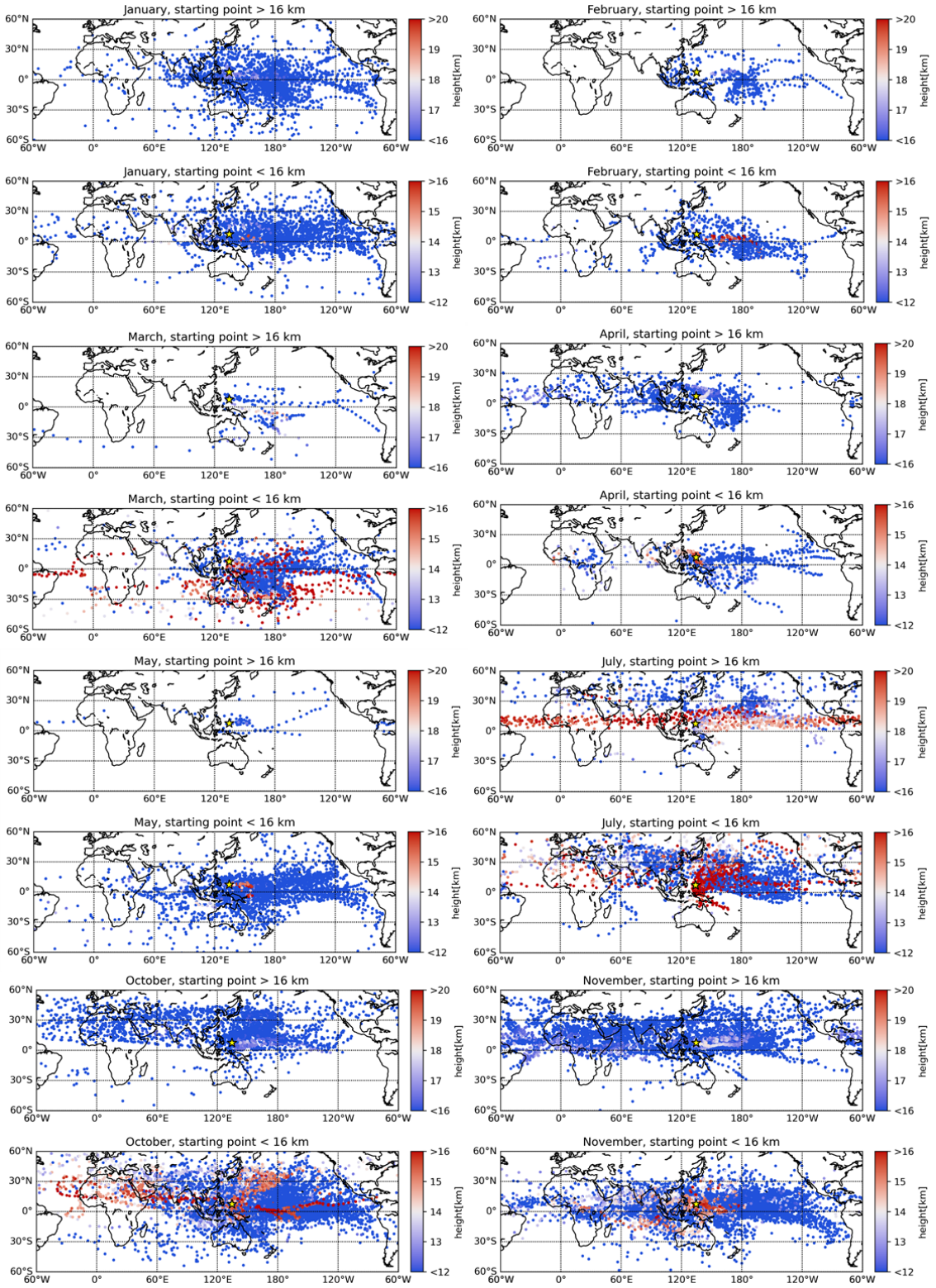

FIGURE B.2: Backward trajectory simulations on other months as a supplement of Figure 4.34. The location of Palau which is the start point of the trajectory is marked by the yellow markers in the figure. Trajectory points are output at hourly intervals, and in this figure, the trajectory points are sparsified at intervals of 20 points for clarity of display.

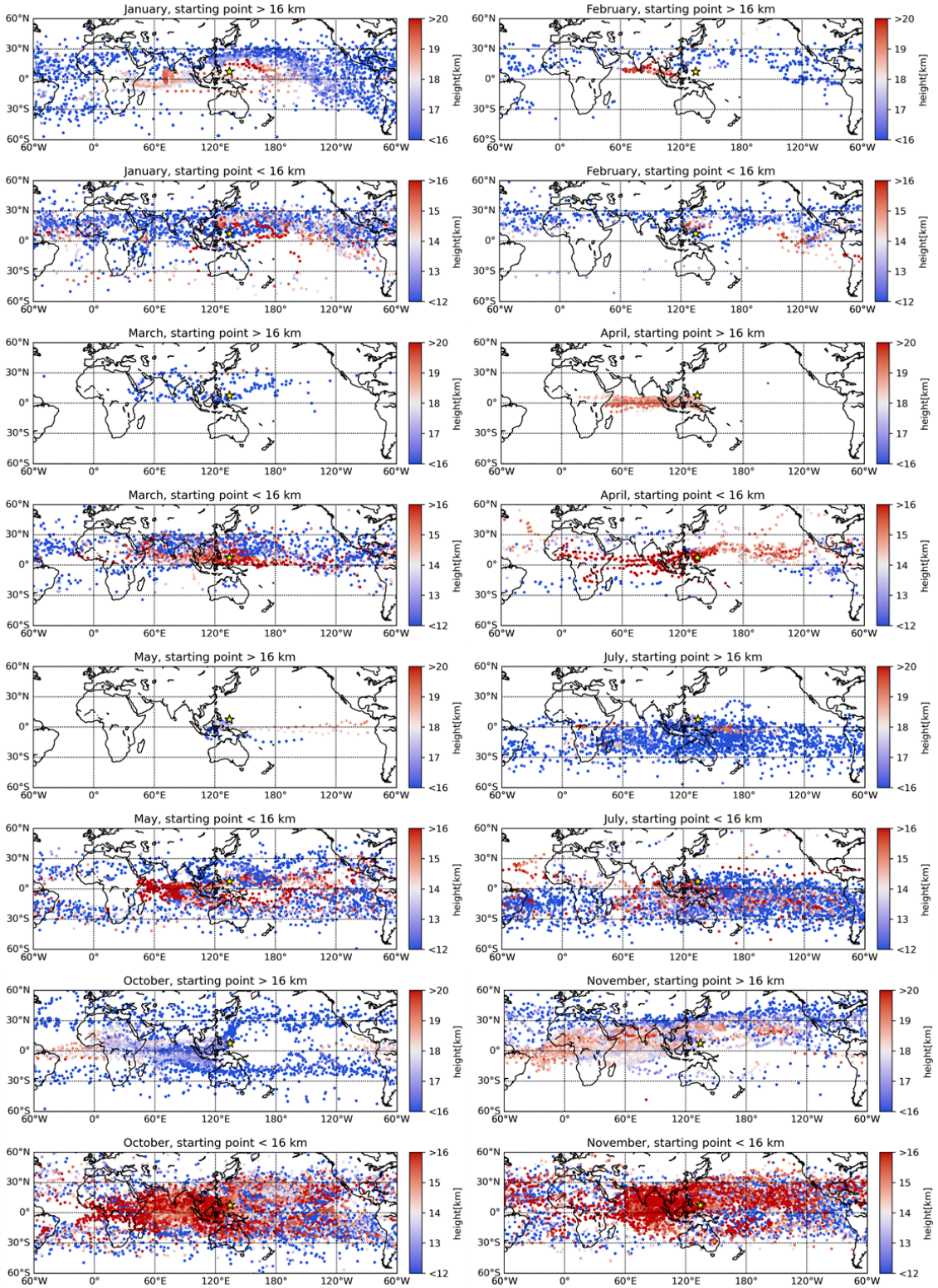

FIGURE B.3: forkward trajectory simulations on other months as a supplement of Figure 4.34. The location of Palau which is the start point of the trajectory is marked by the yellow markers in the figure. Trajectory points are output at hourly intervals, and in this figure, the trajectory points are sparsified at intervals of 20 points for clarity of display.

Bibliography

Adam, Ori, Tobias Bischoff, and Tapio Schneider (2016). "Seasonal and Interannual Variations of the Energy Flux Equator and ITCZ. Part I: Zonally Averaged ITCZ Position". In: *J. Climate* 29.9, pp. 3219 –3230. DOI: 10.1175/JCLI-D-15-0512.1. URL: https://journals.ametsoc.org/view/journals/clim/29/9/jcli-d-15-0512.1.xml.

Ångström, Anders (1929). "On the atmospheric transmission of sun radiation and on dust in the air". In: *Geografiska Annaler* 11.2, pp. 156–166.

Arraut, Josefina Moraes et al. (2012). "Aerial Rivers and Lakes: Looking at Large-Scale Moisture Transport and Its Relation to Amazonia and to Subtropical Rainfall in South America". In: *J. Climate* 25.2, pp. 543 –556. DOI: 10.1175/2011JCLI4189.1. URL: https://journals.ametsoc.org/view/journals/clim/25/2/2011jcli4189.1.xml.

Baars, H. et al. (2008). "Continuous monitoring of the boundary-layer top with lidar". In: *Atmospheric Chemistry and Physics* 8.23, pp. 7281–7296. DOI: 10.5194/acp-8-7281-2008. URL: https://acp.copernicus.org/articles/8/7281/2008/.

Basconcillo, Joseph, Eun-Jeong Cha, and Il-Ju Moon (2021). "Western North Pacific tropical cyclone activity in 2018: A season of extremes". In: *Scientific reports* 11.1, p. 14350. DOI: 10.1038/s41598-021-93824-2.

Bergman, John W et al. (2012a). "Seasonal differences of vertical-transport efficiency in the tropical tropopause layer: On the interplay between tropical deep convection, large-scale vertical ascent, and horizontal circulations". In: *Journal of Geophysical Research: Atmospheres* 117.D5. DOI: 10.1029/2011JD016992.

Bergman, John W. et al. (2012b). "Seasonal differences of vertical-transport efficiency in the tropical tropopause layer: On the interplay between tropical deep convection, large-scale vertical ascent, and horizontal circulations". In: *Journal of Geophysical Research: Atmospheres* 117.D5. DOI: https://doi.org/10.1029/2011JD016992. eprint: https://agupubs.onlinelibrary.wiley.com/doi/pdf/10.1029/2011JD016992. URL: https://agupubs.onlinelibrary.wiley.com/doi/abs/10.1029/2011JD016992.

Berry, Gareth and Michael J. Reeder (2014). "Objective Identification of the Intertropical Convergence Zone: Climatology and Trends from the ERA-Interim". In: *J. Climate* 27.5, pp. 1894 –1909. DOI: 10.1175/JCLI-D-13-00339.1. URL: https://journals.ametsoc.org/view/journals/clim/27/5/jcli-d-13-00339.1.xml.

Bey, Isabelle et al. (2001). "Global modeling of tropospheric chemistry with assimilated meteorology: Model description and evaluation". In: *J. Geophys. Res.* 106.D19, pp. 23073–23095. DOI: https://doi.org/10.1029/2001JD000807. eprint: https://agupubs.onlinelibrary.wiley.com/doi/pdf/10.1029/2001JD000807. URL: https://agupubs.onlinelibrary.wiley.com/doi/abs/10.1029/2001JD000807.

Birner, T., D. Sankey, and T. G. Shepherd (2006). "The tropopause inversion layer in models and analyses". In: *Geophysical Research Letters* 33.14. DOI: https://doi.org/10.1029/2006GL026549. eprint: https://agupubs.onlinelibrary.wiley.com/doi/pdf/10.1029/2006GL026549. URL: https://agupubs.onlinelibrary.wiley.com/doi/abs/10.1029/2006GL026549.

Bjerknes, Jakob (1969). "Atmospheric teleconnections from the equatorial Pacific". In: *Monthly weather review* 97.3, pp. 163–172.

Blum, Edward K and Sergey V Lototsky (2006). *Mathematics of physics and engineering*. World Scientific Publishing Company. Chap. 2, p. 98. ISBN: 978-981-256-621-8.

Boothe, Alexander C and Cameron R Homeyer (2017). "Global large-scale stratosphere–troposphere exchange in modern reanalyses". In: *Atmospheric Chemistry and Physics* 17.9, pp. 5537–5559.

Bourguet, S. and M. Linz (2023). "Weakening of the tropical tropopause layer cold trap with global warming". In: *Atmospheric Chemistry and Physics* 23.13, pp. 7447–7460. DOI: 10.5194/acp-23-7447-2023. URL: https://acp.copernicus.org/articles/23/7447/2023/.

Bucholtz, Anthony (1995). "Rayleigh-scattering calculations for the terrestrial atmosphere". In: *Applied optics* 34.15, pp. 2765–2773.

Burton, SP et al. (2013). "Aerosol classification from airborne HSRL and comparisons with the CALIPSO vertical feature mask". In: *Atmospheric Measurement Techniques* 6.5, pp. 1397–1412.

Cairo, F. et al. (2021). "Lidar observations of cirrus clouds in Palau (7°N, 134°E)". In: *Atmospheric Chemistry and Physics* 21.10, pp. 7947–7961. DOI: 10.5194/acp-21-7947-2021. URL: https://acp.copernicus.org/articles/21/7947/2021/.

Christian, Kenneth et al. (2019). "Radiative forcing and stratospheric warming of pyrocumulonimbus smoke aerosols: First modeling results with multisensor (EPIC, CALIPSO, and CATS) views from space". In: *Geophysical Research Letters* 46.16, pp. 10061–10071.

Collis, RTH (1966). "Lidar: a new atmospheric probe". In: *Quarterly Journal of the Royal Meteorological Society* 92.392, pp. 220–230.

Comstock, Jennifer M. and Christian Jakob (2004). "Evaluation of tropical cirrus cloud properties derived from ECMWF model output and ground based measurements over Nauru Island". In: *Geophysical Research Letters* 31.10. DOI: https://doi.org/10.1029/2004GL019539. eprint: https://agupubs.onlinelibrary.wiley.com/doi/pdf/10.1029/2004GL019539. URL: https://agupubs.onlinelibrary.wiley.com/doi/abs/10.1029/2004GL019539.

Danielsen, Edwin F. (1982). "A dehydration mechanism for the stratosphere". In: *Geophysical Research Letters* 9.6, pp. 605–608. DOI: https://doi.org/10.1029/GL009i006p00605. eprint: https://agupubs.onlinelibrary.wiley.com/doi/pdf/10.1029/GL009i006p00605. URL: https://agupubs.onlinelibrary.wiley.com/doi/abs/10.1029/GL009i006p00605.

Das, Subrata Kumar, Chih-Wei Chiang, and Jan-Bai Nee (2009). "Characteristics of cirrus clouds and its radiative properties based on lidar observation over Chung-Li, Taiwan". In: *Atmospheric Research* 93.4, pp. 723–735. ISSN: 0169-8095. DOI: https://doi.org/10.1016/j.atmosres.2009.02.008. URL: https://www.sciencedirect.com/science/article/pii/S0169809509000672.

DeMott, Paul (2002). *Cirrus: Laboratory studies of cirrus cloud processes*. Oxford University Press, pp. 102–135.

Dessler, AE (2002). "The effect of deep, tropical convection on the tropical tropopause layer". In: *Journal of Geophysical Research: Atmospheres* 107.D3, ACH–6.

Dezfuli, Amin K. et al. (2017). "Validation of IMERG Precipitation in Africa". In: *J. Hydrometeorol.* 18.10, pp. 2817 –2825. DOI: 10.1175/JHM-D-17-0139.1. URL: https://journals.ametsoc.org/view/journals/hydr/18/10/jhm-d-17-0139_1.xml.

Dionisi, D. et al. (2013). "Midlatitude cirrus classification at Rome Tor Vergata through a multichannel Raman–Mie–Rayleigh lidar". In: *Atmospheric Chemistry and Physics*

13.23, pp. 11853–11868. DOI: 10.5194/acp-13-11853-2013. URL: https://acp.copernicus.org/articles/13/11853/2013/.

Dirksen, RJ et al. (2014). "Reference quality upper-air measurements: GRUAN data processing for the Vaisala RS92 radiosonde". In: *Atmospheric Measurement Techniques* 7.12, pp. 4463–4490.

Draxler, Roland R and GD Hess (1998). "An overview of the HYSPLIT_4 modelling system for trajectories". In: *Australian meteorological magazine* 47.4, pp. 295–308.

Fernald, Frederick G (1984). "Analysis of atmospheric lidar observations: some comments". In: *Applied optics* 23.5, pp. 652–653.

Ferrel, W (1856). "Essay on the winds and ocean currents". In: *Nashville J. of Medicine and Surgery* 11, pp. 287–301.

Flury, T., D. L. Wu, and W. G. Read (2012). "Correlation among cirrus ice content, water vapor and temperature in the TTL as observed by CALIPSO and Aura/MLS". In: *Atmospheric Chemistry and Physics* 12.2, pp. 683–691. DOI: 10.5194/acp-12-683-2012. URL: https://acp.copernicus.org/articles/12/683/2012/.

Folkins, Ian, Samuel J Oltmans, and Anne M Thompson (2000). "Tropical convective outflow and near surface equivalent potential temperatures". In: *Geophysical Research Letters* 27.16, pp. 2549–2552.

Folkins, Ian et al. (1999). "A barrier to vertical mixing at 14 km in the tropics: Evidence from ozonesondes and aircraft measurements". In: *Journal of Geophysical Research: Atmospheres* 104.D18, pp. 22095–22102. DOI: 10.1029/1999JD900404.

Fu, Qiang, Yongxiang Hu, and Qiong Yang (2007). "Identifying the top of the tropical tropopause layer from vertical mass flux analysis and CALIPSO lidar cloud observations". In: *Geophysical Research Letters* 34.14.

Fu, Qiang, Maxwell Smith, and Qiong Yang (2018). "The Impact of Cloud Radiative Effects on the Tropical Tropopause Layer Temperatures". In: *Atmosphere* 9.10.

ISSN: 2073-4433. DOI: 10.3390/atmos9100377. URL: https://www.mdpi.com/2073-4433/9/10/377.

Fueglistaler, S and Q Fu (2006). "Impact of clouds on radiative heating rates in the tropical lower stratosphere". In: *Journal of Geophysical Research: Atmospheres* 111.D23.

Fueglistaler, S., H. Wernli, and T. Peter (2004). "Tropical troposphere-to-stratosphere transport inferred from trajectory calculations". In: *Journal of Geophysical Research: Atmospheres* 109.D3. DOI: https://doi.org/10.1029/2003JD004069. eprint: https://agupubs.onlinelibrary.wiley.com/doi/pdf/10.1029/2003JD004069. URL: https://agupubs.onlinelibrary.wiley.com/doi/abs/10.1029/2003JD004069.

Fueglistaler, S. et al. (2005). "Stratospheric water vapor predicted from the Lagrangian temperature history of air entering the stratosphere in the tropics". In: *Journal of Geophysical Research: Atmospheres* 110.D8. DOI: https://doi.org/10.1029/2004JD005516. eprint: https://agupubs.onlinelibrary.wiley.com/doi/pdf/10.1029/2004JD005516. URL: https://agupubs.onlinelibrary.wiley.com/doi/abs/10.1029/2004JD005516.

Fueglistaler, S. et al. (2009). "Tropical tropopause layer". In: *Reviews of Geophysics* 47.1. DOI: https://doi.org/10.1029/2008RG000267. eprint: https://agupubs.onlinelibrary.wiley.com/doi/pdf/10.1029/2008RG000267. URL: https://agupubs.onlinelibrary.wiley.com/doi/abs/10.1029/2008RG000267.

Fujiwara, M. et al. (2009). "Cirrus observations in the tropical tropopause layer over the western Pacific". In: *Journal of Geophysical Research: Atmospheres* 114.D9. DOI: https://doi.org/10.1029/2008JD011040. eprint: https://agupubs.onlinelibrary.wiley.com/doi/pdf/10.1029/2008JD011040. URL: https://agupubs.onlinelibrary.wiley.com/doi/abs/10.1029/2008JD011040.

Gao, Si et al. (2020). "Western North Pacific tropical cyclone activity in 2018: A season of extremes". In: *Scientific reports* 10.1, p. 5610. DOI: 10.1038/s41598-020-62632-5.

Geller, L. S. et al. (1997). "Tropospheric SF6: Observed latitudinal distribution and trends, derived emissions and interhemispheric exchange time". In: *Geophys. Res. Lett.* 24.6, pp. 675–678. DOI: https://doi.org/10.1029/97GL00523. eprint: https://agupubs.onlinelibrary.wiley.com/doi/pdf/10.1029/97GL00523. URL: https://agupubs.onlinelibrary.wiley.com/doi/abs/10.1029/97GL00523.

Gettelman, A and P. M. de Forster (2002). "A climatology of the tropical tropopause layer". In: *Journal of the Meteorological Society of Japan. Ser. II* 80.4B, pp. 911–924.

Gettelman, A. and T. Wang (2015). "Structural diagnostics of the tropopause inversion layer and its evolution". In: *Journal of Geophysical Research: Atmospheres* 120.1, pp. 46–62. DOI: https://doi.org/10.1002/2014JD021846. eprint: https://agupubs.onlinelibrary.wiley.com/doi/pdf/10.1002/2014JD021846. URL: https://agupubs.onlinelibrary.wiley.com/doi/abs/10.1002/2014JD021846.

Gettelman, A. et al. (2009). "The Tropical Tropopause Layer 1960–2100". In: *Atmospheric Chemistry and Physics* 9.5, pp. 1621–1637. DOI: 10.5194/acp-9-1621-2009. URL: https://acp.copernicus.org/articles/9/1621/2009/.

Gettelman, Andrew et al. (2004). "Radiation balance of the tropical tropopause layer". In: *Journal of Geophysical Research: Atmospheres* 109.D7. DOI: https://doi.org/10.1029/2003JD004190. eprint: https://agupubs.onlinelibrary.wiley.com/doi/pdf/10.1029/2003JD004190. URL: https://agupubs.onlinelibrary.wiley.com/doi/abs/10.1029/2003JD004190.

Giannakaki, E et al. (2007). "Optical and geometrical characteristics of cirrus clouds over a Southern European lidar station". In: *Atmospheric Chemistry and Physics* 7.21, pp. 5519–5530.

GMAO (2015). *tavgU_2d_ocn_Nx: MERRA-2 tavgU_2d_ocn_Nx: 2d,diurnal,Time-Averaged,Single-Level,Assimilation,Ocean Surface Diagnostics V5.12.4*. Greenbelt, MD, USA, Goddard Earth Sciences Data and Information Services Center (GES DISC), Accessed: [2023-03-23], at doi: 10.5067/KLNAVGAX7J66.

Gouveia, D. A. et al. (2017). "Optical and geometrical properties of cirrus clouds in Amazonia derived from 1 year of ground-based lidar measurements". In: *Atmospheric Chemistry and Physics* 17.5, pp. 3619–3636. DOI: 10.5194/acp-17-3619-2017. URL: https://acp.copernicus.org/articles/17/3619/2017/.

Grossmann, Klaus U., Oleg Gusev, and Peter Knieling (2006). "The distribution of carbon monoxide in the upper mesosphere and lower thermosphere during CRISTA-1 and -2". In: *Journal of Atmospheric and Solar-Terrestrial Physics* 68.15. CRISTA 1and2 Results in the Mesosphere and Lower Thermosphere, pp. 1764–1780. ISSN: 1364-6826. DOI: https://doi.org/10.1016/j.jastp.2006.05.022. URL: https://www.sciencedirect.com/science/article/pii/S136468260600157X.

Gu, Guojun, Robert F. Adler, and Adam H. Sobel (2005). "The Eastern Pacific ITCZ during the Boreal Spring". In: *J. Atmos. Sci.* 62.4, pp. 1157 –1174. DOI: 10.1175/JAS3402.1. URL: https://journals.ametsoc.org/view/journals/atsc/62/4/jas3402.1.xml.

Hadley, George (1735). "VI. Concerning the cause of the general trade-winds". In: *Philosophical Transactions of the Royal Society of London* 39.437, pp. 58–62. DOI: 10.1098/rstl.1735.0014. eprint: https://royalsocietypublishing.org/doi/pdf/10.1098/rstl.1735.0014. URL: https://royalsocietypublishing.org/doi/abs/10.1098/rstl.1735.0014.

Haladay, Taryn and Graeme Stephens (2009). "Characteristics of tropical thin cirrus clouds deduced from joint CloudSat and CALIPSO observations". In: *Journal of Geophysical Research: Atmospheres* 114.D8. DOI: https://doi.org/10.1029/2008JD010675. eprint: https://agupubs.onlinelibrary.wiley.com/doi/pdf/10.1029/2008JD010675. URL: https://agupubs.onlinelibrary.wiley.com/doi/abs/10.1029/2008JD010675.

Hall, B. D. et al. (2011). "Improving measurements of SF_6 for the study of atmospheric transport and emissions". In: *Atmos. Meas. Tech.* 4.11, pp. 2441–2451. DOI: 10.5194/amt-4-2441-2011. URL: https://amt.copernicus.org/articles/4/2441/2011/.

Hamilton, Jacqueline F. et al. (2008). "Observations of an atmospheric chemical equator and its implications for the tropical warm pool region". In: *J. Geophys. Res.* 113.D20. DOI: https://doi.org/10.1029/2008JD009940. eprint: https://agupubs.onlinelibrary.wiley.com/doi/pdf/10.1029/2008JD009940. URL: https://agupubs.onlinelibrary.wiley.com/doi/abs/10.1029/2008JD009940.

Hase, Frank, Thomas Blumenstock, and Clare Paton-Walsh (1999). "Analysis of the instrumental line shape of high-resolution Fourier transform IR spectrometers with gas cell measurements and new retrieval software". In: *Applied Optics* 38.15, pp. 3417–3422.

Henz, Daniel R. (2010). "A MODELING STUDY OF THE TROPICAL TROPOPAUSE LAYER". In: URL: https://api.semanticscholar.org/CorpusID:13044470.

Hersbach, Hans et al. (2020). "The ERA5 global reanalysis". In: *Q. J. Roy. Meteor. Soc.* 146.730, pp. 1999–2049. DOI: https://doi.org/10.1002/qj.3803. eprint: https://rmets.onlinelibrary.wiley.com/doi/pdf/10.1002/qj.3803. URL: https://rmets.onlinelibrary.wiley.com/doi/abs/10.1002/qj.3803.

Highwood, EJ and BJ Hoskins (1998). "The tropical tropopause". In: *Quarterly Journal of the Royal Meteorological Society* 124.549, pp. 1579–1604.

Holton, James R and Andrew Gettelman (2001). "Horizontal transport and the dehydration of the stratosphere". In: *Geophysical Research Letters* 28.14, pp. 2799–2802. DOI: 10.1029/2001GL013148.

Holton, James R et al. (1995). "Stratosphere-troposphere exchange". In: *Reviews of geophysics* 33.4, pp. 403–439.

Immler, F. et al. (2008a). "Correlation between equatorial Kelvin waves and the occurrence of extremely thin ice clouds at the tropical tropopause". In: *Atmospheric Chemistry and Physics* 8.14, pp. 4019–4026. DOI: 10.5194/acp-8-4019-2008. URL: https://acp.copernicus.org/articles/8/4019/2008/.

Immler, F. et al. (2008b). "Correlation between equatorial Kelvin waves and the occurrence of extremely thin ice clouds at the tropical tropopause". In: *Atmospheric Chemistry and Physics* 8.14, pp. 4019–4026. DOI: 10.5194/acp-8-4019-2008. URL: https://acp.copernicus.org/articles/8/4019/2008/.

Immler, Franz et al. (2006). "A new LIDAR system for the detection of Cloud and aerosol backscatter, depolarization, extinction, and fluorescence". In: *Reviewed and revised papers presented at the 23rd International Laser Radar Converence, 24-28 July 2006 Nara Japan, Editors: Chikao Nagasawa, Nobuo Sugimoto, I*, pp. 35–38.

Immler, Franz et al. (2007). "Cirrus clouds, humidity, and dehydration in the tropical tropopause layer observed at Paramaribo, Suriname (5.8°N, 55.2°W)". In: *Journal of Geophysical Research: Atmospheres* 112.D3. DOI: https://doi.org/10.1029/2006JD007440. eprint: https://agupubs.onlinelibrary.wiley.com/doi/pdf/10.1029/2006JD007440. URL: https://agupubs.onlinelibrary.wiley.com/doi/abs/10.1029/2006JD007440.

Jaeglé, Lyatt et al. (2001). "Chemistry of HOx radicals in the upper troposphere". In: *Atmospheric Environment* 35.3, pp. 469–489.

Jensen, E. J. et al. (2005). "Ice supersaturations exceeding 100% at the cold tropical tropopause: implications for cirrus formation and dehydration". In: *Atmospheric Chemistry and Physics* 5.3, pp. 851–862. DOI: 10.5194/acp-5-851-2005. URL: https://acp.copernicus.org/articles/5/851/2005/.

Jensen, E. J. et al. (2010). "Ice nucleation and cloud microphysical properties in tropical tropopause layer cirrus". In: *Atmospheric Chemistry and Physics* 10.3, pp. 1369–1384. DOI: 10.5194/acp-10-1369-2010. URL: https://acp.copernicus.org/articles/10/1369/2010/.

Jensen, Eric J. et al. (1996). "Dehydration of the upper troposphere and lower stratosphere by subvisible cirrus clouds near the tropical tropopause". In: *Geophysical Research Letters* 23.8, pp. 825–828. DOI: https://doi.org/10.1029/96GL00722. eprint: https://agupubs.onlinelibrary.wiley.com/doi/pdf/10.1029/96GL00722. URL: https://agupubs.onlinelibrary.wiley.com/doi/abs/10.1029/96GL00722.

Kanamitsu, Masao (1989). "Description of the NMC global data assimilation and forecast system". In: *Weather and forecasting* 4.3, pp. 335–342. DOI: https://doi.org/10.1175/1520-0434(1989)004<0335:DOTNGD>2.0.CO;2.

Keller, C. A. et al. (2014a). "HEMCO v1.0: a versatile, ESMF-compliant component for calculating emissions in atmospheric models". In: *Geoscientific Model Development* 7.4, pp. 1409–1417. DOI: 10.5194/gmd-7-1409-2014. URL: https://gmd.copernicus.org/articles/7/1409/2014/.

— (2014b). "HEMCO v1.0: a versatile, ESMF-compliant component for calculating emissions in atmospheric models". In: *Geoscientific Model Development* 7.4,

pp. 1409–1417. DOI: 10.5194/gmd-7-1409-2014. URL: https://gmd.copernicus.org/articles/7/1409/2014/.

Klett, James D (1981). "Stable analytical inversion solution for processing lidar returns". In: *Applied optics* 20.2, pp. 211–220.

Kley, D et al. (1996). "Observations of near-zero ozone concentrations over the convective Pacific: Effects on air chemistry". In: *Science* 274.5285, pp. 230–233.

Kley, D et al. (1997). "Tropospheric water-vapour and ozone cross-sections in a zonal plane over the central equatorial Pacific Ocean". In: *Quarterly Journal of the Royal Meteorological Society* 123.543, pp. 2009–2040.

Krämer, M. et al. (2016). "A microphysics guide to cirrus clouds – Part 1: Cirrus types". In: *Atmospheric Chemistry and Physics* 16.5, pp. 3463–3483. DOI: 10.5194/acp-16-3463-2016. URL: https://acp.copernicus.org/articles/16/3463/2016/.

Krol, M. et al. (2018). "Age of air as a diagnostic for transport timescales in global models". In: *Geoscientific Model Development* 11.8, pp. 3109–3130. DOI: 10.5194/gmd-11-3109-2018. URL: https://gmd.copernicus.org/articles/11/3109/2018/.

Krüger, K., S. Tegtmeier, and M. Rex (2008). "Long-term climatology of air mass transport through the Tropical Tropopause Layer (TTL) during NH winter". In: *Atmos. Chem. Phys.* 8.4, pp. 813–823. DOI: 10.5194/acp-8-813-2008. URL: https://acp.copernicus.org/articles/8/813/2008/.

Law, R. M. et al. (2008). "TransCom model simulations of hourly atmospheric CO2: Experimental overview and diurnal cycle results for 2002". In: *Global Biogeochemical Cycles* 22.3. DOI: https://doi.org/10.1029/2007GB003050. eprint: https://agupubs.onlinelibrary.wiley.com/doi/pdf/10.1029/2007GB003050.

URL: https://agupubs.onlinelibrary.wiley.com/doi/abs/10.1029/2007GB003050.

Lee, June-Yi and Bin Wang (2014). "Future change of global monsoon in the CMIP5". In: *Climate Dynamics* 42, pp. 101–119. DOI: 10.1007/s00382-012-1564-0.

Levy, H (1971). "Normal atmosphere: Large radical and formaldehyde concentrations predicted". In: *Science* 173.3992, pp. 141–143.

Lin, H. et al. (2021). "Harmonized Emissions Component (HEMCO) 3.0 as a versatile emissions component for atmospheric models: application in the GEOS-Chem, NASA GEOS, WRF-GC, CESM2, NOAA GEFS-Aerosol, and NOAA UFS models". In: *Geoscientific Model Development* 14.9, pp. 5487–5506. DOI: 10.5194/gmd-14-5487-2021. URL: https://gmd.copernicus.org/articles/14/5487/2021/.

Lin, Shian-Jiann and Richard B. Rood (1996). "Multidimensional Flux-Form Semi-Lagrangian Transport Schemes". In: *Mon. Weather. Rev.* 124.9, pp. 2046 –2070. DOI: 10.1175/1520-0493(1996)124<2046:MFFSLT>2.0.CO;2. URL: https://journals.ametsoc.org/view/journals/mwre/124/9/1520-0493_1996_124_2046_mffslt_2_0_co_2.xml.

Loberto, Tom Di (2014). *the Walker Circulation: ENSO's atmospheric buddy*. https://www.climate.gov/news-features/blogs/enso/walker-circulation-ensos-atmospheric-buddy. Accessed: 2023-11-06.

Magee, Andrew D. and Danielle C. Verdon-Kidd (2018). "On the relationship between Indian Ocean sea surface temperature variability and tropical cyclogenesis in the southwest Pacific". In: *Int. J. Climatol.* 38.S1, e774–e795. DOI: https://doi.org/10.1002/joc.5406. eprint: https://rmets.onlinelibrary.wiley.com/doi/pdf/10.1002/joc.5406. URL: https://rmets.onlinelibrary.wiley.com/doi/abs/10.1002/joc.5406.

Martins, E., V. Noel, and H. Chepfer (2011). "Properties of cirrus and subvisible cirrus from nighttime Cloud-Aerosol Lidar with Orthogonal Polarization (CALIOP), related to atmospheric dynamics and water vapor". In: *Journal of Geophysical Research: Atmospheres* 116.D2. DOI: https://doi.org/10.1029/2010JD014519. eprint: https://agupubs.onlinelibrary.wiley.com/doi/pdf/10.1029/2010JD014519. URL: https://agupubs.onlinelibrary.wiley.com/doi/abs/10.1029/2010JD014519.

McFarquhar, Greg M. et al. (2000). "Thin and Subvisual Tropopause Tropical Cirrus: Observations and Radiative Impacts". In: *Journal of the Atmospheric Sciences* 57.12, pp. 1841 –1853. DOI: https://doi.org/10.1175/1520-0469(2000)057<1841:TASTTC>2.0.CO;2. URL: https://journals.ametsoc.org/view/journals/atsc/57/12/1520-0469_2000_057_1841_tasttc_2.0.co_2.xml.

Morris, Robert A. et al. (1995). "Effects of electron and ion reactions on atmospheric lifetimes of fully fluorinated compounds". In: *J. Geophys. Res.* 100.D1, pp. 1287–1294. DOI: https://doi.org/10.1029/94JD02399. eprint: https://agupubs.onlinelibrary.wiley.com/doi/pdf/10.1029/94JD02399. URL: https://agupubs.onlinelibrary.wiley.com/doi/abs/10.1029/94JD02399.

Müller, K. et al. (2023a). "Air Mass Transport to the Tropical West Pacific Troposphere inferred from Ozone and Relative Humidity Balloon Observations above Palau". In: *EGUsphere* 2023, pp. 1–37. DOI: 10.5194/egusphere-2023-1518. URL: https://egusphere.copernicus.org/preprints/2023/egusphere-2023-1518/.

Müller, K. et al. (2023b). "Measurement Report: The Palau Atmospheric Observatory and its Ozonesonde Record - Continuous Monitoring of Tropospheric Composition and Dynamics in the Tropical West Pacific". In: *EGUsphere* 2023, pp. 1–35. DOI: 10.5194/egusphere-2023-1023. URL: https://egusphere.copernicus.org/preprints/2023/egusphere-2023-1023/.

Müller, Katrin (2020). "Characterization of Ozone and the Oxidizing Capacity of the Tropical West Pacific Troposphere, Ph.D. thesis, Fachbereich Physik und Elektrotechnik der Universität Bremen, Germany". In.

Müller, Katrin et al. (2023c). "Measurement Report: The Palau Atmospheric Observatory and its Ozonesonde Record-Continuous Monitoring of Tropospheric Composition and Dynamics in the Tropical West Pacific". In: *EGUsphere* 2023, pp. 1–35.

Muntean, Marilena et al. (2018). "Evaluating EDGARv4.tox2 speciated mercury emissions ex-post scenarios and their impacts on modelled global and regional wet deposition patterns". In: *Atmospheric Environment* 184, pp. 56–68. ISSN: 1352-2310. DOI: https://doi.org/10.1016/j.atmosenv.2018.04.017. URL: https://www.sciencedirect.com/science/article/pii/S1352231018302425.

Nakoudi, Konstantina, Christoph Ritter, and Iwona S. Stachlewska (2021). "Properties of Cirrus Clouds over the European Arctic (Ny-Ålesund, Svalbard)". In: *Remote Sensing* 13.22. ISSN: 2072-4292. DOI: 10.3390/rs13224555. URL: https://www.mdpi.com/2072-4292/13/22/4555.

Nakoudi, Konstantina, Iwona S. Stachlewska, and Christoph Ritter (2021). "An extended lidar-based cirrus cloud retrieval scheme: first application over an Arctic site". In: *Opt. Express* 29.6, pp. 8553–8580. DOI: 10.1364/OE.414770. URL: https://opg.optica.org/oe/abstract.cfm?URI=oe-29-6-8553.

Newell, Reginald E. and Sharon Gould-Stewart (1981). "A Stratospheric Fountain?" In: *J. Atmos. Sci.* 38.12, pp. 2789 –2796. DOI: 10.1175/1520-0469(1981)038<2789:ASF>2.0.CO;2. URL: https://journals.ametsoc.org/view/journals/atsc/38/12/1520-0469_1981_038_2789_asf_2_0_co_2.xml.

Nicholson, Sharon E. (2018). "The ITCZ and the Seasonal Cycle over Equatorial Africa". In: *B. Am. Meteor. Soc.* 99.2, pp. 337 –348. DOI: 10.1175/BAMS-D-16-

0287.1. URL: https://journals.ametsoc.org/view/journals/bams/99/2/bams-d-16-0287.1.xml.

Pace, Giandomenico et al. (2003). "Lidar observations of equatorial cirrus clouds at Mahé Seychelles". In: *Journal of Geophysical Research: Atmospheres* 108.D8. DOI: https://doi.org/10.1029/2002JD002710. eprint: https://agupubs.onlinelibrary.wiley.com/doi/pdf/10.1029/2002JD002710. URL: https://agupubs.onlinelibrary.wiley.com/doi/abs/10.1029/2002JD002710.

Pan, Laura L et al. (2018). "Lapse rate or cold point: The tropical tropopause identified by in situ trace gas measurements". In: *Geophysical Research Letters* 45.19, pp. 10–756. DOI: https://doi.org/10.1029/2018GL079573.

Pan, LL and LA Munchak (2011). "Relationship of cloud top to the tropopause and jet structure from CALIPSO data". In: *Journal of Geophysical Research: Atmospheres* 116.D12.

Pandit, A. K. et al. (2015). "Long-term trend analysis and climatology of tropical cirrus clouds using 16 years of lidar data set over Southern India". In: *Atmospheric Chemistry and Physics* 15.24, pp. 13833–13848. DOI: 10.5194/acp-15-13833-2015. URL: https://acp.copernicus.org/articles/15/13833/2015/.

Pandit, Amit Kumar et al. (2014). "Characteristics of cirrus clouds and tropical tropopause layer: Seasonal variation and long-term trends". In: *Journal of Atmospheric and Solar-Terrestrial Physics* 121. The Indian Programme on CLIMATE AND WEATHER OF THE SUN EARTH SYSTEM Scientific Accomplishments from Phase II, pp. 248–256. ISSN: 1364-6826. DOI: https://doi.org/10.1016/j.jastp.2014.07.008. URL: https://www.sciencedirect.com/science/article/pii/S1364682614001734.

Park, S. et al. (2007). "The CO_2 tracer clock for the Tropical Tropopause Layer". In: *Atmospheric Chemistry and Physics* 7.14, pp. 3989–4000. DOI: 10.5194/acp-7-3989-2007. URL: https://acp.copernicus.org/articles/7/3989/2007/.

Patra, P. K. et al. (2011). "TransCom model simulations of CH_4 and related species: linking transport, surface flux and chemical loss with CH_4 variability in the troposphere and lower stratosphere". In: *Atmospheric Chemistry and Physics* 11.24, pp. 12813–12837. DOI: 10.5194/acp-11-12813-2011. URL: https://acp.copernicus.org/articles/11/12813/2011/.

Perlwitz, Judith, Thomas Knutson, and James Kossin (2017). "Large-scale circulation and climate variability". In: *: Climate Science Special Report: Fourth National Climate Assessment, Volume I [Wuebbles, D.J., D.W. Fahey, K.A. Hibbard, D.J. Dokken, B.C. Stewart, and T.K. Maycock (eds.)]*, pp. 161–184. DOI: https://doi.org/10.7930/J0RV0KVQ.

Petersen, A. K. et al. (2010). "First ground-based FTIR observations of methane in the inner tropics over several years". In: *Atmos. Chem. Phys.* 10.15, pp. 7231–7239. DOI: 10.5194/acp-10-7231-2010. URL: https://acp.copernicus.org/articles/10/7231/2010/.

Pfister, Leonhard et al. (2001). "Aircraft observations of thin cirrus clouds near the tropical tropopause". In: *Journal of Geophysical Research: Atmospheres* 106.D9, pp. 9765–9786. DOI: https://doi.org/10.1029/2000JD900648. eprint: https://agupubs.onlinelibrary.wiley.com/doi/pdf/10.1029/2000JD900648. URL: https://agupubs.onlinelibrary.wiley.com/doi/abs/10.1029/2000JD900648.

Pilch Kedzierski, R., K. Matthes, and K. Bumke (2016). "The tropical tropopause inversion layer: variability and modulation by equatorial waves". In: *Atmospheric Chemistry and Physics* 16.18, pp. 11617–11633. DOI: 10.5194/acp-16-11617-2016. URL: https://acp.copernicus.org/articles/16/11617/2016/.

Platt, C. M. R., S. C. Scott, and A. C. Dilley (1987). "Remote Sounding of High Clouds. Part VI: Optical Properties of Midlatitude and Tropical Cirrus". In: *Journal of Atmospheric Sciences* 44.4, pp. 729 –747. DOI: https://doi.org/10.1175/1520-

0469(1987)044<0729:RSOHCP>2.0.CO;2. URL: https://journals.ametsoc.org/view/journals/atsc/44/4/1520-0469_1987_044_0729_rsohcp_2_0_co_2.xml.

Platt, C. M. R. et al. (1998). "The Optical Properties of Equatorial Cirrus from Observations in the ARM Pilot Radiation Observation Experiment". In: *Journal of the Atmospheric Sciences* 55.11, pp. 1977 –1996. DOI: https://doi.org/10.1175/1520-0469(1998)055<1977:TOPOEC>2.0.CO;2. URL: https://journals.ametsoc.org/view/journals/atsc/55/11/1520-0469_1998_055_1977_topoec_2.0.co_2.xml.

Pommereau, Jean-Pierre (2010). "Troposphere-to-stratosphere transport in the tropics". In: *Comptes Rendus Geoscience* 342.4. Atmosphère vue de l'espace, pp. 331–338. ISSN: 1631-0713. DOI: https://doi.org/10.1016/j.crte.2009.10.015. URL: https://www.sciencedirect.com/science/article/pii/S1631071309002855.

Pope, Robin M and Edward S Fry (1997). "Absorption spectrum (380–700 nm) of pure water. II. Integrating cavity measurements". In: *Applied optics* 36.33, pp. 8710–8723. DOI: 10.1364/AO.36.008710.

Ramage, C. S. (1968). "ROLE OF A TROPICAL "MARITIME CONTINENT" IN THE ATMOSPHERIC CIRCULATION". In: *Mon. Weather. Rev.* 96.6, pp. 365 –370. DOI: 10.1175/1520-0493(1968)096<0365:ROATMC>2.0.CO;2. URL: https://journals.ametsoc.org/view/journals/mwre/96/6/1520-0493_1968_096_0365_roatmc_2_0_co_2.xml.

Randel, William J and Eric J Jensen (2013). "Physical processes in the tropical tropopause layer and their roles in a changing climate". In: *Nature Geoscience* 6.3, pp. 169–176. DOI: 10.1038/ngeo1733.

Randel, William J et al. (2016). "Dry layers in the tropical troposphere observed during CONTRAST and global behavior from GFS analyses". In: *Journal of Geophysical Research: Atmospheres* 121.23, pp. 14–142.

Ravishankara, A. R. et al. (1993). "Atmospheric Lifetimes of Long-Lived Halogenated Species". In: *Science* 259.5092, pp. 194–199. DOI: 10.1126/science.259.5092.194. eprint: https://www.science.org/doi/pdf/10.1126/science.259.5092.194. URL: https://www.science.org/doi/abs/10.1126/science.259.5092.194.

Ray, Eric A. et al. (2017). "Quantification of the SF6 lifetime based on mesospheric loss measured in the stratospheric polar vortex". In: *J. Geophys. Res.* 122.8, pp. 4626–4638. DOI: https://doi.org/10.1002/2016JD026198. eprint: https://agupubs.onlinelibrary.wiley.com/doi/pdf/10.1002/2016JD026198. URL: https://agupubs.onlinelibrary.wiley.com/doi/abs/10.1002/2016JD026198.

Reverdy, M. et al. (2012). "On the origin of subvisible cirrus clouds in the tropical upper troposphere". In: *Atmospheric Chemistry and Physics* 12.24, pp. 12081–12101. DOI: 10.5194/acp-12-12081-2012. URL: https://acp.copernicus.org/articles/12/12081/2012/.

Rex, M. et al. (2014). "A tropical West Pacific OH minimum and implications for stratospheric composition". In: *Atmos. Chem. Phys.* 14.9, pp. 4827–4841. DOI: 10.5194/acp-14-4827-2014. URL: https://acp.copernicus.org/articles/14/4827/2014/.

Rigby, M. et al. (2010). "History of atmospheric SF_6 from 1973 to 2008". In: *Atmos. Chem. Phys.* 10.21, pp. 10305–10320. DOI: 10.5194/acp-10-10305-2010. URL: https://acp.copernicus.org/articles/10/10305/2010/.

Ritter, C. et al. (2016). "2014 iAREA campaign on aerosol in Spitsbergen – Part 2: Optical properties from Raman-lidar and in-situ observations at Ny-Ålesund". In: *Atmospheric Environment* 141, pp. 1–19. ISSN: 1352-2310. DOI: https://doi.org/10.1016/j.atmosenv.2016.05.053. URL: https://www.sciencedirect.com/science/article/pii/S1352231016304010.

Rodgers, Clive D (2000). *Inverse methods for atmospheric sounding: theory and practice*. Vol. 2. World scientific.

Sassen, Kenneth and Sally Benson (2001). "A Midlatitude Cirrus Cloud Climatology from the Facility for Atmospheric Remote Sensing. Part II: Microphysical Properties Derived from Lidar Depolarization". In: *Journal of the Atmospheric Sciences* 58.15, pp. 2103 –2112. DOI: https://doi.org/10.1175/1520-0469(2001)058<2103:AMCCCF>2.0.CO;2. URL: https://journals.ametsoc.org/view/journals/atsc/58/15/1520-0469_2001_058_2103_amcccf_2.0.co_2.xml.

Sassen, Kenneth and Byung Sung Cho (1992). "Subvisual-Thin Cirrus Lidar Dataset for Satellite Verification and Climatological Research". In: *Journal of Applied Meteorology and Climatology* 31.11, pp. 1275 –1285. DOI: https://doi.org/10.1175/1520-0450(1992)031<1275:STCLDF>2.0.CO;2. URL: https://journals.ametsoc.org/view/journals/apme/31/11/1520-0450_1992_031_1275_stcldf_2_0_co_2.xml.

Sassen, Kenneth, Zhien Wang, and Dong Liu (2008). "Global distribution of cirrus clouds from CloudSat/Cloud-Aerosol lidar and infrared pathfinder satellite observations (CALIPSO) measurements". In: *Journal of Geophysical Research: Atmospheres* 113.D8. DOI: https://doi.org/10.1029/2008JD009972.

— (2009). "Cirrus clouds and deep convection in the tropics: Insights from CALIPSO and CloudSat". In: *Journal of Geophysical Research: Atmospheres* 114.D4. DOI: https://doi.org/10.1029/2009JD011916. eprint: https://agupubs.onlinelibrary.wiley.com/doi/pdf/10.1029/2009JD011916. URL: https://agupubs.onlinelibrary.wiley.com/doi/abs/10.1029/2009JD011916.

Schmidt, T. et al. (2010). "Observational characteristics of the tropopause inversion layer derived from CHAMP/GRACE radio occultations and MOZAIC aircraft data". In: *Journal of Geophysical Research: Atmospheres* 115.D24. DOI: https://doi.

org/10.1029/2010JD014284. eprint: https://agupubs.onlinelibrary.wiley.com/doi/pdf/10.1029/2010JD014284. URL: https://agupubs.onlinelibrary.wiley.com/doi/abs/10.1029/2010JD014284.

Schneider, Tapio, Tobias Bischoff, and Gerald H Haug (2014). "Migrations and dynamics of the intertropical convergence zone". In: *Nature* 513.7516, pp. 45–53. DOI: 10.1038/nature13636. URL: https://doi.org/10.1038/nature13636.

Schneising, O. et al. (2019). "A scientific algorithm to simultaneously retrieve carbon monoxide and methane from TROPOMI onboard Sentinel-5 Precursor". In: *Atmospheric Measurement Techniques* 12.12, pp. 6771–6802. DOI: 10.5194/amt-12-6771-2019. URL: https://amt.copernicus.org/articles/12/6771/2019/.

Schneising, Oliver et al. (Feb. 2023). "Advances in retrieving XCH_4 and XCO from Sentinel-5 Precursor: improvements in the scientific TROPOMI/WFMD algorithm". English. In: *Atmospheric Measurement Techniques* 16.3. Publisher: Copernicus GmbH, pp. 669–694. ISSN: 1867-1381. DOI: 10.5194/amt-16-669-2023. URL: https://amt.copernicus.org/articles/16/669/2023/ (visited on 03/03/2023).

Schoeberl, M. R. et al. (2019). "Water Vapor, Clouds, and Saturation in the Tropical Tropopause Layer". In: *Journal of Geophysical Research: Atmospheres* 124.7, pp. 3984–4003. DOI: https://doi.org/10.1029/2018JD029849. eprint: https://agupubs.onlinelibrary.wiley.com/doi/pdf/10.1029/2018JD029849. URL: https://agupubs.onlinelibrary.wiley.com/doi/abs/10.1029/2018JD029849.

Seifert, P. et al. (2007). "Cirrus optical properties observed with lidar, radiosonde, and satellite over the tropical Indian Ocean during the aerosol-polluted northeast and clean maritime southwest monsoon". In: *Journal of Geophysical Research: Atmospheres* 112.D17. DOI: https://doi.org/10.1029/2006JD008352. eprint: https://agupubs.onlinelibrary.wiley.com/doi/pdf/10.1029/2006JD008352.

URL: https://agupubs.onlinelibrary.wiley.com/doi/abs/10.1029/2006JD008352.

Sherwood, Steven C. (2000). "A stratospheric "drain" over the maritime continent". In: *Geophysical Research Letters* 27.5, pp. 677–680. DOI: https://doi.org/10.1029/1999GL010868. eprint: https://agupubs.onlinelibrary.wiley.com/doi/pdf/10.1029/1999GL010868. URL: https://agupubs.onlinelibrary.wiley.com/doi/abs/10.1029/1999GL010868.

Sherwood, Steven C and Andrew E Dessler (2001). "A model for transport across the tropical tropopause". In: *Journal of the Atmospheric Sciences* 58.7, pp. 765–779. DOI: 10.1175/1520-0469(2001)058<0765:AMFTAT>2.0.CO;2.

Shi, Hailiang et al. (2023). "High Resolution Fourier Transform Spectrometer for Ground-Based Verification of Greenhouse Gases Satellites". In: *Remote Sensing* 15.6. ISSN: 2072-4292. DOI: 10.3390/rs15061671. URL: https://www.mdpi.com/2072-4292/15/6/1671.

Sicard, Michaël et al. (2020). "Calculation of the Overlap Function and Associated Error of an Elastic Lidar or a Ceilometer: Cross-Comparison with a Cooperative Overlap-Corrected System". In: *Sensors* 20.21. ISSN: 1424-8220. DOI: 10.3390/s20216312. URL: https://www.mdpi.com/1424-8220/20/21/6312.

Smith, Ian N., Aurel F. Moise, and Robert A. Colman (2012). "Large-scale circulation features in the tropical western Pacific and their representation in climate models". In: *J. Geophys. Res.* 117.D4. DOI: https://doi.org/10.1029/2011JD016667. eprint: https://agupubs.onlinelibrary.wiley.com/doi/pdf/10.1029/2011JD016667. URL: https://agupubs.onlinelibrary.wiley.com/doi/abs/10.1029/2011JD016667.

Solomon, Susan et al. (2010). "Contributions of stratospheric water vapor to decadal changes in the rate of global warming". In: *Science* 327.5970, pp. 1219–1223.

Spichtinger, Peter (2014). "Shallow cirrus convection – a source for ice supersaturation". In: *Tellus A: Dynamic Meteorology and Oceanography* 66.1, p. 19937. DOI: 10.3402/tellusa.v66.19937.

Spichtinger, Peter et al. (2003). "Ice supersaturation in the tropopause region over Lindenberg, Germany". In: *Meteorologische Zeitschrift* 12.3, pp. 143–156. DOI: 10.1127/0941-2948/2003/0012-0143.

Stehr, J. W. et al. (2002). "Latitudinal gradients in O3 and CO during INDOEX 1999". In: *J. Geophys. Res.* 107.D19, INX2 15–1–INX2 15–8. DOI: https://doi.org/10.1029/2001JD000446. eprint: https://agupubs.onlinelibrary.wiley.com/doi/pdf/10.1029/2001JD000446. URL: https://agupubs.onlinelibrary.wiley.com/doi/abs/10.1029/2001JD000446.

Stein, A. F. et al. (2015). "NOAA's HYSPLIT Atmospheric Transport and Dispersion Modeling System". In: *Bulletin of the American Meteorological Society* 96.12, pp. 2059 –2077. DOI: https://doi.org/10.1175/BAMS-D-14-00110.1. URL: https://journals.ametsoc.org/view/journals/bams/96/12/bams-d-14-00110.1.xml.

Sun, Bomin et al. (2019). "On the accuracy of Vaisala RS41 versus RS92 upper-air temperature observations". In: *Journal of Atmospheric and Oceanic Technology* 36.4, pp. 635–653.

Sun, X. et al. (2023). "Determination of the chemical equator from GEOS-Chem model simulation: a focus on the tropical western Pacific region". In: *Atmospheric Chemistry and Physics* 23.12, pp. 7075–7090. DOI: 10.5194/acp-23-7075-2023. URL: https://acp.copernicus.org/articles/23/7075/2023/.

Sun, Y. et al. (2022). "Monitoring greenhouse gases (GHGs) in China: status and perspective". In: *Atmospheric Measurement Techniques* 15.16, pp. 4819–4834. DOI:

10.5194/amt-15-4819-2022. URL: https://amt.copernicus.org/articles/15/4819/2022/.

Sunilkumar, SV et al. (2017). "Boundaries of tropical tropopause layer (TTL): A new perspective based on thermal and stability profiles". In: *Journal of Geophysical Research: Atmospheres* 122.2, pp. 741–754.

Takahashi, Hanii, Zhengzhao Johnny Luo, and Graeme L. Stephens (2017). "Level of neutral buoyancy, deep convective outflow, and convective core: New perspectives based on 5 years of CloudSat data". In: *Journal of Geophysical Research: Atmospheres* 122.5, pp. 2958–2969. DOI: https://doi.org/10.1002/2016JD025969. eprint: https://agupubs.onlinelibrary.wiley.com/doi/pdf/10.1002/2016JD025969. URL: https://agupubs.onlinelibrary.wiley.com/doi/abs/10.1002/2016JD025969.

Uthe, EE and PB Russell (1977). "LIDAR OBSERVATIONS OF TROPICAL HIGH-ALTITUDE CIRRUS CLOUDS." In: pp. 242–244.

Veefkind, J. P. et al. (2012). "TROPOMI on the ESA Sentinel-5 Precursor: A GMES mission for global observations of the atmospheric composition for climate, air quality and ozone layer applications". In: *Remote Sensing of Environment* 120, pp. 70–83. ISSN: 0034-4257. DOI: 10.1016/j.rse.2011.09.027. URL: https://www.sciencedirect.com/science/article/pii/S0034425712000661.

Villamayor, Julián et al. (2023). "Very short-lived halogens amplify ozone depletion trends in the tropical lower stratosphere". In: *Nature Climate Change*, pp. 1–7. DOI: 10.1038/s41558-023-01671-y.

Virts, Katrina S. and John M. Wallace (2010). "Annual, Interannual, and Intraseasonal Variability of Tropical Tropopause Transition Layer Cirrus". In: *Journal of the Atmospheric Sciences* 67.10, pp. 3097 –3112. DOI: https://doi.org/10.1175/

2010JAS3413.1. URL: https://journals.ametsoc.org/view/journals/atsc/67/10/2010jas3413.1.xml.

— (2014). "Observations of Temperature, Wind, Cirrus, and Trace Gases in the Tropical Tropopause Transition Layer during the MJO". In: *Journal of the Atmospheric Sciences* 71.3, pp. 1143 –1157. DOI: https://doi.org/10.1175/JAS-D-13-0178.1. URL: https://journals.ametsoc.org/view/journals/atsc/71/3/jas-d-13-0178.1.xml.

Virts, Katrina S et al. (2010). "Tropical tropopause transition layer cirrus as represented by CALIPSO lidar observations". In: *Journal of the Atmospheric Sciences* 67.10, pp. 3113–3129. DOI: https://doi.org/10.1175/2010JAS3413.1.

Voudouri, K. A. et al. (2020). "Variability in cirrus cloud properties using a Polly^{XT} Raman lidar over high and tropical latitudes". In: *Atmospheric Chemistry and Physics* 20.7, pp. 4427–4444. DOI: 10.5194/acp-20-4427-2020. URL: https://acp.copernicus.org/articles/20/4427/2020/.

Waliser, Duane E. and Catherine Gautier (1993). "A Satellite-derived Climatology of the ITCZ". In: *J. Climate* 6.11, pp. 2162 –2174. DOI: 10.1175/1520-0442(1993)006<2162:ASDCOT>2.0.CO;2. URL: https://journals.ametsoc.org/view/journals/clim/6/11/1520-0442_1993_006_2162_asdcot_2_0_co_2.xml.

Wallace, John M and Peter V Hobbs (2006). *Atmospheric science: an introductory survey*. Vol. 92. Elsevier.

Wang, Bin et al. (2012). "Recent change of the global monsoon precipitation (1979–2008)". In: *Climate Dynamics* 39, pp. 1123–1135. DOI: 10.1007/s00382-011-1266-z.

Wang, Chiachi and Gudrun Magnusdottir (2006). "The ITCZ in the Central and Eastern Pacific on Synoptic Time Scales". In: *Mon. Weather. Rev.* 134.5, pp. 1405 –

1421. DOI: 10.1175/MWR3130.1. URL: https://journals.ametsoc.org/view/journals/mwre/134/5/mwr3130.1.xml.

Wang, Pi-Huan et al. (1996). "A 6-year climatology of cloud occurrence frequency from Stratospheric Aerosol and Gas Experiment II observations (1985–1990)". In: *Journal of Geophysical Research: Atmospheres* 101.D23, pp. 29407–29429. DOI: https://doi.org/10.1029/96JD01780. eprint: https://agupubs.onlinelibrary.wiley.com/doi/pdf/10.1029/96JD01780. URL: https://agupubs.onlinelibrary.wiley.com/doi/abs/10.1029/96JD01780.

Waugh, D. W. et al. (2013). "Tropospheric SF6: Age of air from the Northern Hemisphere midlatitude surface". In: *J. Geophys. Res.* 118.19, pp. 11,429–11,441. DOI: https://doi.org/10.1002/jgrd.50848. eprint: https://agupubs.onlinelibrary.wiley.com/doi/pdf/10.1002/jgrd.50848. URL: https://agupubs.onlinelibrary.wiley.com/doi/abs/10.1002/jgrd.50848.

Weitkamp, Claus (2006). *Lidar: range-resolved optical remote sensing of the atmosphere*. Vol. 102. Springer Science & Business.

Williams, J. et al. (2002). "Near equatorial CO and O3 profiles over the Indian Ocean during the winter monsoon: High O3 levels in the middle troposphere and interhemispheric exchange". In: *J. Geophys. Res.* 107.D19, INX2 6–1–INX2 6–13. DOI: https://doi.org/10.1029/2001JD001126. eprint: https://agupubs.onlinelibrary.wiley.com/doi/pdf/10.1029/2001JD001126. URL: https://agupubs.onlinelibrary.wiley.com/doi/abs/10.1029/2001JD001126.

Wu, Xueke, Qiang Fu, and Chihiro Kodama (2023). "Response of Tropical Overshooting Deep Convection to Global Warming Based on Global Cloud-Resolving Model Simulations". In: *Geophysical Research Letters* 50.14. e2023GL104210 2023GL104210, e2023GL104210. DOI: https://doi.org/10.1029/2023GL104210. eprint: https://agupubs.onlinelibrary.wiley.com/doi/pdf/10.1029/2023GL104210.

URL: https://agupubs.onlinelibrary.wiley.com/doi/abs/10.1029/2023GL104210.

Wunch, Debra et al. (2010). "Calibration of the Total Carbon Column Observing Network using aircraft profile data". In: *Atmospheric Measurement Techniques* 3.5, pp. 1351–1362.

Yang, Huang et al. (2019). "Evaluating Simulations of Interhemispheric Transport: Interhemispheric Exchange Time Versus SF6 Age". In: *Geophys. Res. Lett.* 46.2, pp. 1113–1120. DOI: https://doi.org/10.1029/2018GL080960. eprint: https://agupubs.onlinelibrary.wiley.com/doi/pdf/10.1029/2018GL080960. URL: https://agupubs.onlinelibrary.wiley.com/doi/abs/10.1029/2018GL080960.

Zhou, M. et al. (2018). "Atmospheric CO and CH_4 time series and seasonal variations on Reunion Island from ground-based in situ and FTIR (NDACC and TCCON) measurements". In: *Atmos. Chem. Phys.* 18.19, pp. 13881–13901. DOI: 10.5194/acp-18-13881-2018. URL: https://acp.copernicus.org/articles/18/13881/2018/.

Zou, L. et al. (2020). "Revisiting global satellite observations of stratospheric cirrus clouds". In: *Atmospheric Chemistry and Physics* 20.16, pp. 9939–9959. DOI: 10.5194/acp-20-9939-2020. URL: https://acp.copernicus.org/articles/20/9939/2020/.